Astrophysical Institute Potsdam
Solar Radio Physics

Electron Acceleration in a Flare Plasma via Coronal Circuits

Dissertation
for obtaining the academic degree
"doctor rerum naturalium"
(Dr. rer. nat.)

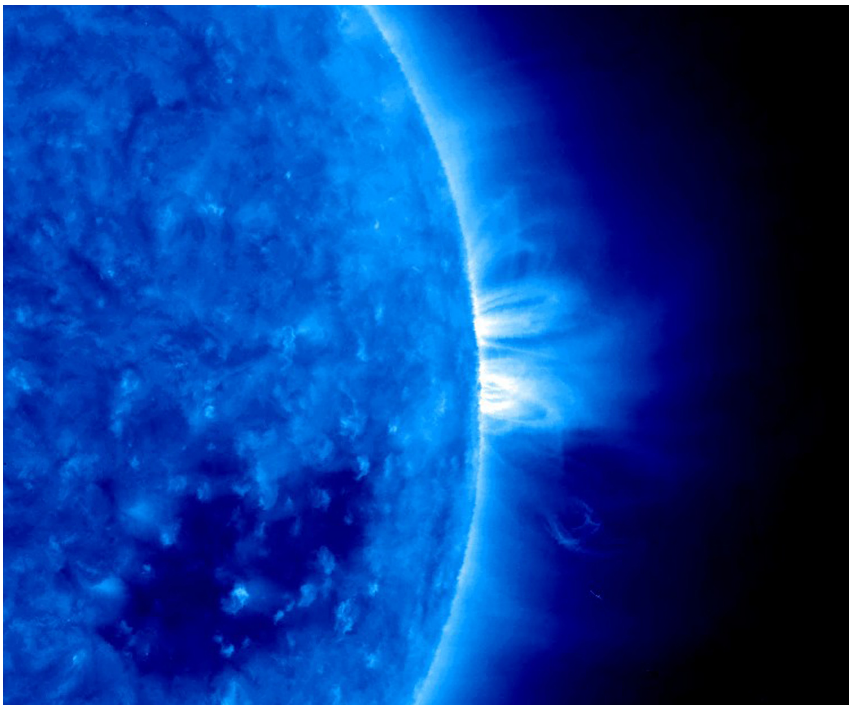

submitted at the
Faculty of Mathematics and Natural Sciences
at the Potsdam University

by

Hakan Önel

Potsdam, August 11, 2008

Published online at the
Institutional Repository of the University of Potsdam:
http://opus.kobv.de/ubp/volltexte/2009/2903/
urn:nbn:de:kobv:517-opus-29035
[http://nbn-resolving.de/urn:nbn:de:kobv:517-opus-29035]

This dissertation is a product of the collaboration between the Potsdam University and the Astrophysical Institute Potsdam (AIP).

Potsdam University

— Faculty of Mathematics and Natural Sciences, Institute for Physics —

Am Neuen Palais 10
14469 Potsdam, Brandenburg
Federal Republic of Germany

Astrophysical Institute Potsdam (AIP)

— Solar Radio Physics —

An der Sternwarte 16
14482 Potsdam, Brandenburg
Federal Republic of Germany

Thesis advisor: Prof. Dr. Gottfried J. Mann (AIP)

Referees:	1st	Prof. Dr.	Gottfried J. Mann	(AIP)
	2nd	Prof. Dr.	Erwin Sedlmayr	(Berlin University of Technology)
	3rd	Prof. Dr.	Jun-Ichi Sakai	(University of Toyama)

Date of oral defence: December 17, 2008

Cover photo: The spacecraft *STEREO Ahead* has pictured bright magnetic loops on May 26, 2007. The picture was taken at a wavelength of 171 Å (in extreme ultraviolet).

Abstract

The Sun is a star, which due to its vicinity has a tremendous influence on Earth. Since the very first days mankind tried to "understand the Sun", and especially in the 20^{th} century science has uncovered many of the Sun's secrets by using high resolution observations and describing the Sun by means of models. The knowledge obtained in these endeavours could be applied to stars far beyond the boundaries of our solar system, where observations are not as neat as in the case of the Sun (solar-stellar relations).

As an active star the Sun's activity expressed in its magnetic cycle, is closely related to the sunspot numbers. Flares play a special role, because they set free large energies on very short time scales. They are correlated with enhanced electromagnetic emissions all over the spectrum, i.e., from the radio up to the γ-ray range. Furthermore flares are sources for energetic particles. Hard X-ray observations (e.g., by NASA's *RHESSI* spacecraft) reveal that a large fraction of the energy released during a flare is transferred into the kinetic energy of electrons. However the mechanism that accelerates a large number of electrons to high energies (beyond 20 keV) in fractions of a second is not understood yet.

The thesis at hand presents a model for the generation of energetic electrons during flares that explains the electron acceleration using real parameters obtained by real ground and space based observations.

According to this model photospheric plasma flows build up electric potentials in the active regions in the photosphere. Usually these electric potentials are associated with electric currents closed within the photosphere. However as a result of magnetic reconnection, a magnetic connection between the regions of different magnetic polarity on the photosphere can establish through the corona. Due to the significantly higher electric conductivity in the corona, the photospheric electric power supply can be closed via the corona. Subsequently a high electric current is formed, which leads to the generation of hard X-ray radiation in the dense chromosphere. Simple estimations show that the coronal electric current's power is comparable to the power of large flares.

The previously described idea is modelled and investigated by means of electric circuits. For this the microscopic plasma parameters, the magnetic field geometry and hard X-ray observations are used to obtain parameters for modelling macroscopic electric components, such as electric resistors, which are connected with each other. By this it is demonstrated that such a coronal electric current is correlated with high large scale electric fields, which can accelerate the electrons quickly up to relativistic energies.

The results of these calculations are encouraging. The electron fluxes predicted by the model are in agreement with the electron fluxes deduced from the measured photon fluxes. Additionally the model developed, proposes a new way to understand the observed double footpoint hard X-ray sources. Hence the presented model can be regarded as a step toward a better understanding of the generation of flare electrons.

Thesis' structure

It is the aim of this thesis to develop a model, which is able to describe the acceleration of a sufficient number of electrons, within fractions of a second to high energies. The model needs to explain where the source of power for the flare is located, and how the double hard X-ray sources are established, and why the highly energetic electron currents are not associated with high magnetic fields in the corona.

The thesis is structured in five parts. The first three parts represent the scientific contents, i.e., in the first part a general but brief introduction for the thesis' topic is found. Therein the Sun and its structure are explained shortly, while the major focus is laid on the description of the explosive solar events.

The second part focuses on the model developed in the thesis and its application on electron acceleration. Hence electric circuits are introduced in order to estimate electric fields needed for the calculations of the electron acceleration.

In the thesis' third part the results of the model presented before are discussed, by applying the calculations to the Sun. Electron flux spectra are derived for several different cases and explained.

The forth part contains appendices, with several remarks and details that do not fit into the three parts before.

Finally the epilogue follows in the fifth part, containing acknowledgements, a bibliography and the index.

Contents

List of Figures

List of Tables

Part I

Introduction

If the Earth is the size of a pea in New York, then the Sun is a beach ball fifty metres away, Pluto is four kilometres away, and the next star is in Tokyo. Now shrink Pluto's orbit into a coffee cup; then our Milky Way Galaxy fills North America.

– Wayne Hayes

CHAPTER 1

The Sun

At the beginning of the 17^{th} century (1611) three Europeans, i.e., Johannes Fabricius, Christoph Schreiner, and Galileo Galilei observed the Sun independently from one another. What they found was revolutionary: They spotted “dark spots” on “god’s creation”. This incident can be understood as the beginning of solar astronomy, or even as the foundation of solar physics. Since then mankind has tried to understand all the processes running in and on the Sun. Even though the knowledge gained by human race has reached a tremendous amount today, many new questions have shown up. Questions which are still waiting to be answered.

In this thesis such an open question is addressed: It is an observed fact that solar energy releases, such as the later explained solar flares are accompanied by X-ray emissions. The sources for these emissions are energetic electrons, which travel through the dense chromosphere and produce X-ray radiation via Bremsstrahlung processes. The acceleration mechanism for these electrons still contains many riddles for modern science to solve. It is the aim of this thesis to explain a possible process, which may allow for the transfer of a large fraction of the total flare energy within fractions of a second into the kinetic energy of electrons. Since the Sun is an ordinary star, scientific discoveries made here, can be applied to stars far away. Hence the model presented in this thesis may be an important contribution for understanding the events in the solar corona and on other active stellar objects throughout the universe.

Though the Sun is found to be an average star, if compared with other stars in the universe, it is the most important one for the inhabitants of Earth. It is the centre of our solar system and the source for energy and life on Earth, which makes it very unique from mankind’s point of view. Due to the increasing use of modern technology in the 20^{th} century, the Sun’s influence on the civilised life on the Earth increased substantially. In order to obtain a better understanding of the Sun and its influence on Earth, the explosive events related with the Sun have become a focus for intensive study and the topic of interest in this thesis.

CHAPTER 2

The structure of the Sun

This chapter explores the Sun's structure. The information presented about the Sun and the processes which run on or in it, shall give the reader an overview only. Special attention is drawn toward those facts which carry high importance for the present work. A claim for completeness of the information presented here cannot be made, since it would be beyond the scope of this thesis.

2.1 Solar interior

The Sun is a G2 V spectral class main-sequence yellow dwarf star. It's mass composition is primarily made by hydrogen (about 73%) and helium (about 25%), with a small portion (about 2%) of heavier elements (Eddy & Ise, 1979).

In Fig. 2.1 some of the most prominent features of the Sun's structure are presented. On the first view it can be seen that the solar interior is constituted by three zones, i.e., the solar core, the radiative zone, and the convection zone. These zones are briefly introduced in the following.

The solar core is the inner most region of the Sun. As a result of the nuclear fusion, nuclear energy is transformed into thermal energy. Hence the energy released per second in the Sun's core is about $3.86 \times 10^{26}\,\mathrm{W}$.[1] The solar core extends from the centre to about $0.2\,R_\odot$, where $R_\odot$ represents the solar radius. The temperature in the core reaches up to about 15 MK, whereas the maximum density therein is about $148 \times 10^{3}\,\mathrm{kg/m^3}$.[2,3]

The radiative zone is the region next to the solar core. It extends from about $0.2\,R_\odot$ to about $0.7\,R_\odot$. The temperature in this zone decreases down to about 1 MK. This region is still highly ionised. There is no thermal convection, and the thermal energy from the core is transported outward by electromagnetic radiation only. Since the plasma is fully ionised, the radiation is repeatedly absorbed and re-emitted. Thus an average photon needs a long time (e.g., Mitalas & Sills (1992) estimate 1.7×10^{5} years) to traverse this region.

[1] The p-p chain reaction transforms a mass loss of 4.3×10^{9} kg per second into thermal energy (Williams, D. R., 2007), i.e., each second the Sun loses 2.2×10^{-21} of its total mass.
[2] For comparison: The density of solid Iron (at the temperature of 300 K) is $7\,874\,\mathrm{kg/m^3}$.
[3] Almost 30% of the solar mass is contained in nearly 3% of the Sun's volume.

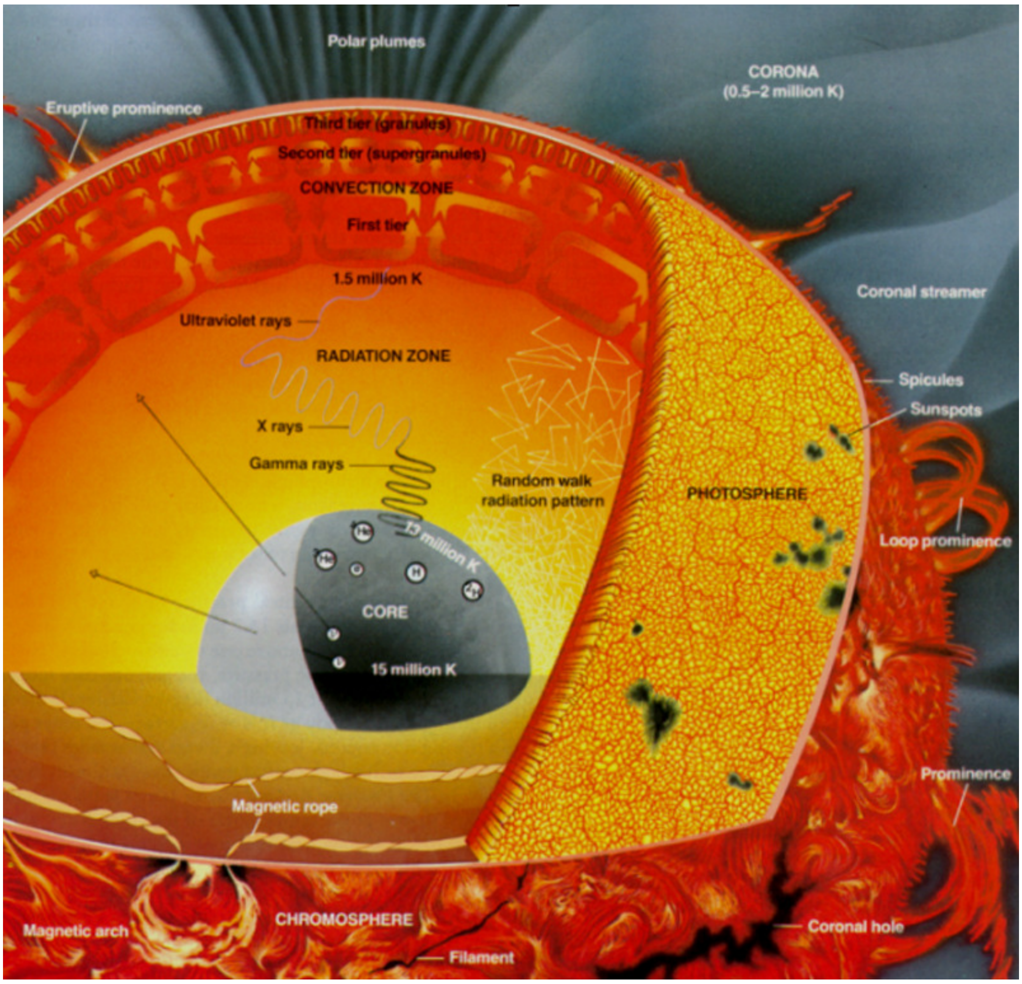

Figure 2.1: The Sun is a giant luminescent plasma ball. This figure shows its inner and outer structure; reference: Jansen *et al.* (2003).

The tachocline is the transition layer which separates two differently rotating regimes, namely the differentially rotating outer solar layers, and the uniformly rotating radiative interior one (see Fig. 2.2). Helioseismic methods[1] indicate that this transition is sharp and located near the base of the convection zone (Miesch, 2005).

The convection zone is the next solar layer. There the solar plasma is neither dense nor hot enough for the radiative energy transfer. Hence thermal convection occurs, which transports heat to the photosphere by material flow: At the top of the radiation zone the material is heated, why its density decreases, and it starts to ascent. When the hot material cools down on its way outside, its density increases. When its density becomes sufficiently high, it starts to descent again. The very effective energy transport[2] in the convection zone causes turbulence responsible for the continuously redistribution of angular momentum, leading to the phenomenon named differential rotation. The plasma close to the solar poles rotates slower (i.e., rotation period of 35 days), than the plasma close to the solar equator (i.e., rotation period of 25 days). Furthermore the origin for the Sun's magnetic activity is located in the convection zone. The Sun's magnetic field is generated

[1] The concepts of helioseismology are explained by Birch & Gizon (2005).
[2] Thermal convection can transport energy through the convection zone within a few days.

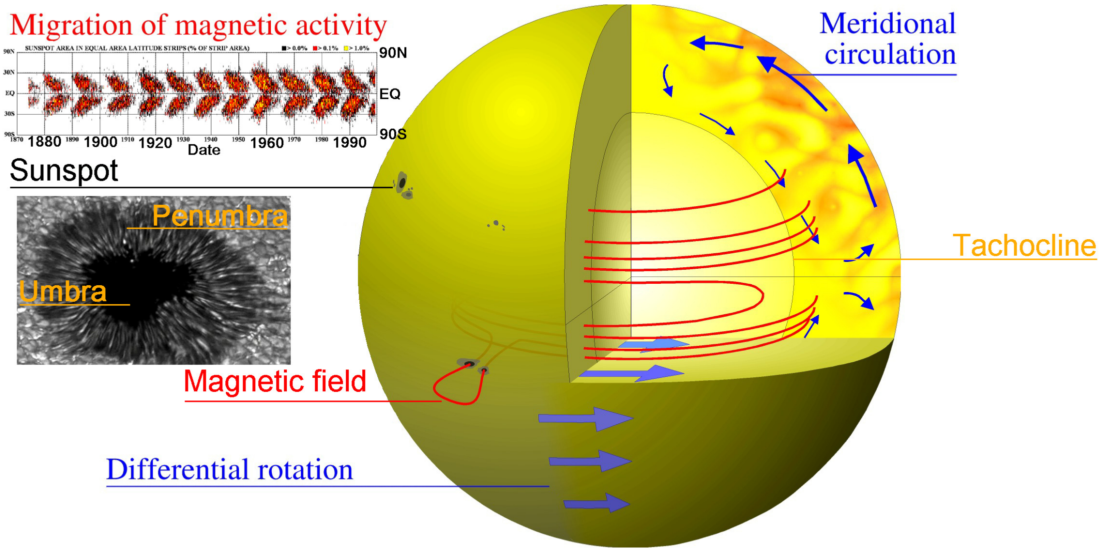

Figure 2.2: This image presents different aspects of the solar activity cycle: The magnetic field (red) builds up by convection and differential rotation (blue). The meridional circulation (blue), transports magnetic energy towards the equator. Wherever strong magnetic fields penetrate the photosphere sunspots are created. At the beginning of a solar cycle sunspots appear in high latitudes and then as the cycle progresses, they migrate toward the equatorial regions. Reference: Image significantly modified for this thesis. The original image (courtesy of R. Arlt) was published in, e.g., Kneer *et al.* (2003).

due to the solar dynamo driven by thermal convection, differential rotation, and meridional flows, i.e., these material flows are correlated with electric currents, which again cause magnetic fields.

The magnetic fields are the connectors of the solar interior with the solar exterior, e.g., sunspots, which are observable in the photosphere, are strongly related with the Sun's magnetic field: As seen in Fig. 2.2 the generated magnetic field is winded up by the differential rotation and if as a result of that, the magnetic flux tubes penetrate the photosphere, sunspots are generated. Further details about sunspots can be found in the next section.

2.2 Solar atmosphere

The layer next to the interior convection zone can be understood as the solar surface, i.e., the photosphere. The solar atmosphere above the photosphere is constituted by the chromosphere, the transition region, and the corona. All these regions have different properties and contain different features (Fig. 2.3).

The photosphere has a depth of about 400 km and a density of about $2 \times 10^{-4}\,\mathrm{kg/m^3}$. It fully absorbs all the visible light which comes from the solar interior, i.e., the is is the layer which the visible light cannot pass. In other words, the Sun becomes opaque at the photosphere for the electromagnetic radiation and therefore the photosphere is understood as the solar "surface". Hence the Sun represents a good approximation for a black body with a temperature of 5 778 K. The Frauenhofer absorption lines in the solar spectrum originate mainly from the photospheric matter.

The granules are convection cells which can be observed in the photosphere (see Fig. 2.4). They consist of hot ascending matter at the centre, and cooler matter falling in the narrow spaces between them. Granules have a diameter of approximately 1 000 km and their lifespan is about eleven minutes (Dialetis *et al.*, 1986).

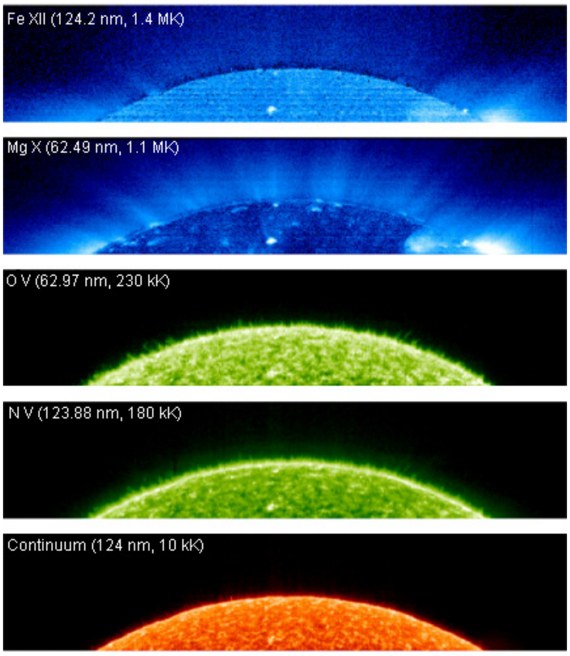

Figure 2.3: The outer layers of the Sun's atmosphere can for instance be observed with instruments aboard *SOHO* spacecraft. The line emissions from the highly ionised elements in the Sun's atmosphere is related to the local conditions, e.g., the local temperature. Reference: Jansen *et al.* (2003).

The supergranules are grouping of the granules. These structures are distributed uniformly on the solar disk and have diameters of about 30 000 km. Their lifespan lasts up to a few days (Beck & Duvall, 2001; Birch & Gizon, 2005; Gizon *et al.*, 2003a,b).

The sunspots, which is the real name of the "dark spots" already mentioned at the very beginning of this chapter, are also accommodated in the photosphere. They are regions of high magnetic flux penetrating the solar photosphere: Due to strong magnetic fields the thermal convection underneath the photosphere is disturbed, and the hot plasma is rerouted. Thus the heat flux coming from the solar interior is reduced. Hence the temperature in these regions is only about 4 000 K to 4 500 K and therefore lower than in the rest of the photosphere. Consequently these cool regions, the so-called sunspots appear dark compared with the hot photosphere.

The number of sunspots is a measure for the solar activity. It varies in the 11 years cycle, which is also called Schwabe cycle. A new cycle begins, when the first sunspots appear at high solar latitudes. During the cycle these spots wander towards the solar equator which they reach at the end of the solar cycle. This can be seen in Fig. 2.2, where the so called butterfly diagram is displayed for the years from 1870 to 2000 showing the number of sunspots as a function of time and solar latitude. A complete magnetic cycle, also called Hale cycle, consists of to two solar activity cycles, i.e., the magnetic polarities are reversed after each solar cycle, see e.g., Fan (2004); Schrijver & DeRosa (2003); Stix (2002).

Figure 2.2 also contains the illustration of a sunspot. Such a sunspot consists of two regions, i.e., the relatively cool ($\approx$ 4 000 K) and dark umbra in centre and the warmer ($\approx$ 5 000 K) and brighter penumbra surrounding the umbra. Evershed (1909) observed a radial flow of photospheric matter across the photospheric surface of the penumbra of sunspots: It is directed from the inner border of the umbra towards the outer edge.

Photospheric flows represent an other important aspect of the photosphere. Indeed these flow motions are a mixture of several different motions, e.g., the Evershed motion, i.e., a radial

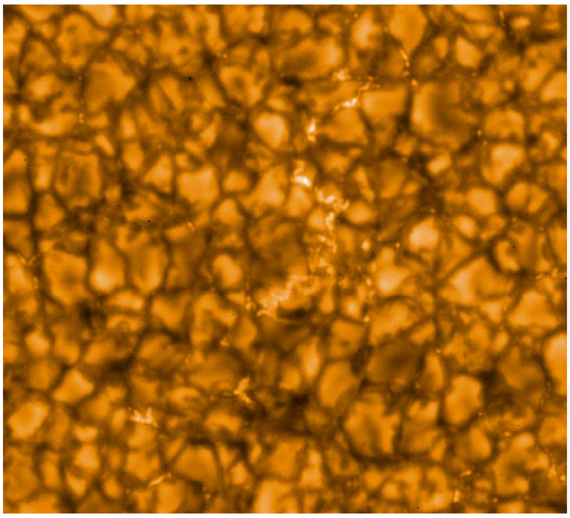

Figure 2.4: The granulation is pictured by the Solar Optical Telescope on *Hinode*. Energy from below the surface of the photosphere is transported by convection and results in the convection cells, or granulation, as seen in this image. The lighter areas reveal where gases are rising from below, while the darker "intergranular lanes" reveal where cooler gases are sinking back down. Reference: European Space Agency (2006).

outflow of matter along the sunspots (Chitre, 1968; Evershed, 1909). Often a cyclonic (also called vortex like) plasma motion is observed (see e.g., Hofmann *et al.*, 1992; Martres *et al.*, 1973), and high plasma shear velocities can be seen in the photosphere (Schleicher *et al.*, 2003; Xu *et al.*, 2004; Yang *et al.*, 2004). Figure 5.2 (pg. 33) illustrates among other things the photospheric motion in the case of the active region NOAA AR 10486. Typical flow velocities are in the order of about $1\,{}^{\mathrm{km}}/_{\mathrm{s}}$.

The chromosphere is the region right above the photosphere. By definition this layer begins there, where the temperature reaches the local minimum of about 4 500 K, see Fig. 2.5. It is a relatively thin layer with a depth of about 10 Mm. The chromosphere's visual spectrum is dominated by the Lyman-α spectral line of hydrogen.

Spicules are the most common features in the chromosphere. In the green coloured panels of Fig. 2.3 spicules can be seen at the solar limb, i.e., they look like long wires, and contain luminous gas. Spicules have a lifetime of about eight minutes.

The transition region is the region between the chromosphere and the corona. In Fig. 2.5 the height profile of the temperature, the electron and the neutral hydrogen density are plotted. As seen the transition region is a very thin layer, wherein the temperature rapidly rises from roughly 10 kK in the chromosphere to 1 MK in the corona. Due to the increased thermal energy the solar atmosphere becomes highly ionised in the sharp transition region and the corona. For illustration, Fig. 2.5 shows the density height profile of neutral hydrogen which rapidly decreases in the transition region.

The corona is the hottest outer layer of the solar atmosphere. It is best visible during a total solar eclipse, and its shape and structure highly varies during the solar activity cycle. The quite Sun's corona has a temperature of about 1 MK to 2 MK. The coronal temperature is sufficient to bear highly ionised particles, as e.g., H II or Fe XVI. Hence the coronal plasma is a good

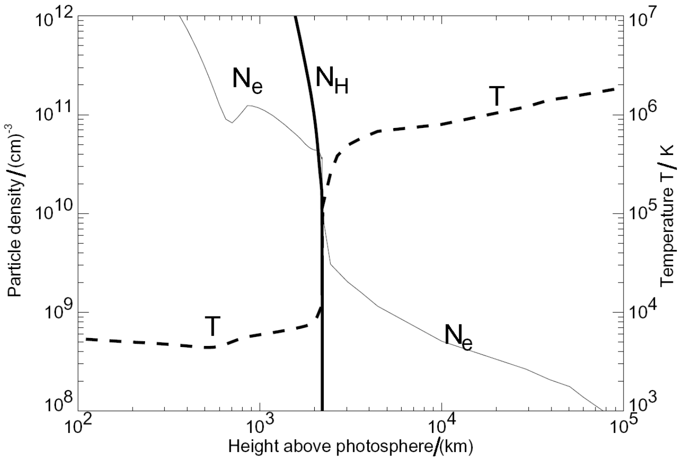

Figure 2.5: Electron temperature (dashed curve), electron density (thin solid curve), and neutral hydrogen density (thick solid curve) height profiles are plotted in dependence on the height above the photosphere; references: Aschwanden (2006); Vocks (2001).

approximation for an ideal plasma[1]. Due to the high coronal temperature the corona emits electromagnetic radiation mainly in EUV[2] and X-ray. Since the Earth's atmosphere absorbs radiation in these wavelength range, ground based observation does not suffice to observe the processes in the corona and space based observations are needed. The outer corona continues in the interplanetary space filled with the solar wind.

Coronal magnetic loops are closed magnetic field lines located in the corona. As shown in Figs. 2.6 and 2.7 the corona contains magnetic field lines which are mainly responsible for the non uniform coronal structure (Longcope, 2005): These fields confine the coronal plasma in them, and thus the magnetic loops are regions of dense plasma and appear as bright phenomena, when compared to the surrounding region.

Coronal holes are features located in the corona. Often they can be observed close to the solar polar regions. In comparison with the rest of the corona the coronal holes are cool regions of low particle density. Primarily they maintain open magnetic field configurations.[3] Along these open field lines the atmospheric plasma can leave the Sun and penetrate into the interplanetary space.

Prominences are an other coronal feature (Fig. 2.8). They are large structures of relatively cool but dense plasma in the thin corona (Gilbert *et al.*, 2001). From time to time, they can be ejected into the interplanetary space by eruptive events such as flares and coronal mass ejections, as described in Chapter 3.

The solar wind is a continuous outflow of charged particles, mainly of electrons and protons. It is established due to the hydrodynamic expansion of the corona, which means that the particles constituting the solar wind can overcome the solar gravitation due to their thermal energy (Marsch, 2006; Parker, 1958, 1963). The outflow velocity varies from 200 km/s to 800 km/s (Matthaeus *et al.*,

[1] An ideal plasma has an infinitely high electric conductivity.
[2] EUV stands for extreme ultraviolet.
[3] The Maxwell equation $\mathrm{div}[\vec{B}] = 0$, where $\vec{B}$ represents the magnetic flux density vector declares that all magnetic field lines are closed. In solar physics the terminology of an open solar magnetic field line means that the concerning magnetic field line is closed very far away, e.g., in the interplanetary space.

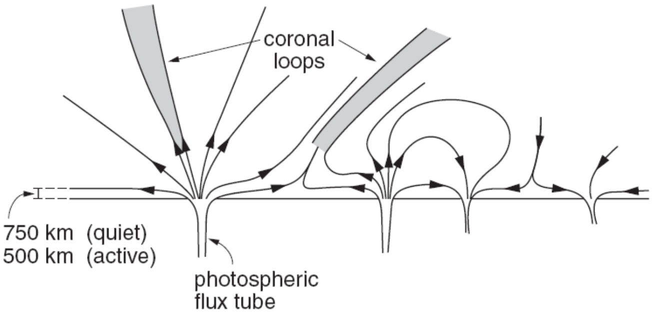

Figure 2.6: The structure of the solar magnetic field is illustrated in the figure. It can be seen that the magnetic field is responsible for the non-uniformity of the solar atmosphere; reference: Encyclopedia of Astronomy and Astrophysics (2006).

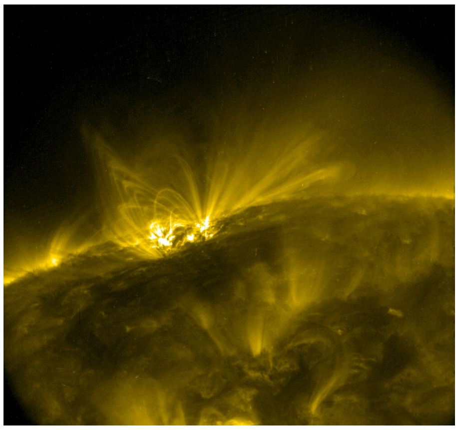

Figure 2.7: Magnetic arcs are pictured by *TRACE* on August 9, 2006 23:55:05 UT. The bright structure is the active region NOAA AR 10904.

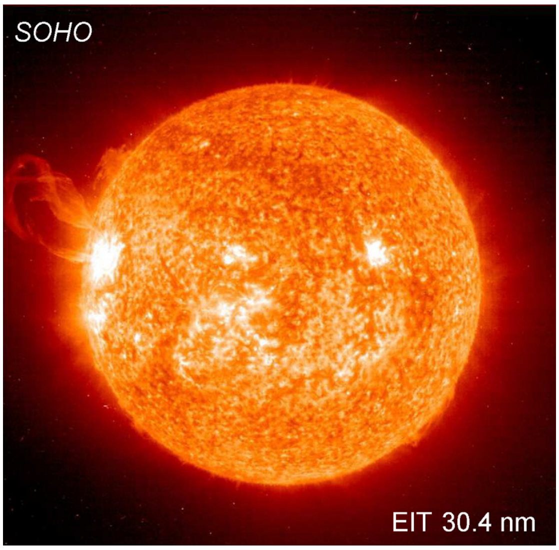

Figure 2.8: A huge eruptive prominence can be seen; reference: O'Neill (1998).

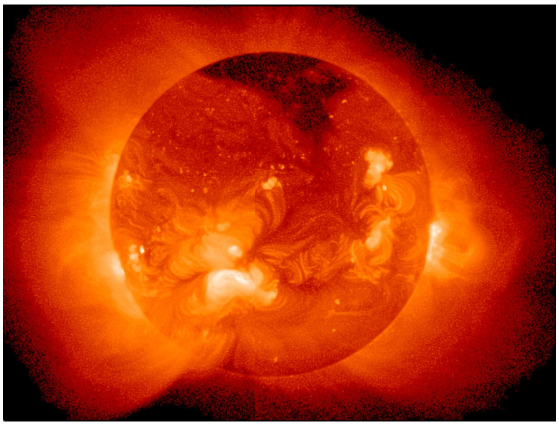

Figure 2.9: X-ray image made by *Yohkoh*. Bright regions correspond to dense matter.

2006; Vocks, 2007).[1] About one million tonnes of mass is carried away from the Sun per second. The wind's density and temperature at about 1 AU is in the order of about 5×10^6 particles per cubic metre and 10^5 K, respectively. Two kinds of the solar wind can be distinguished, i.e., the slow/fast streamers originating from the equatorial/polar region, respectively (see Fig. 2.10).

The heliosphere is the region in space, created by the solar wind, which is blown into the interstellar medium. Its boundary is defined by the location where the pressure of the solar and the interstellar wind become equal and the heliopause is formed. The heliosphere has an extension of about 100 AU.

[1] For comparison: The second escape velocity with respect to the Sun (at the solar equator) is 617.6 km/s.

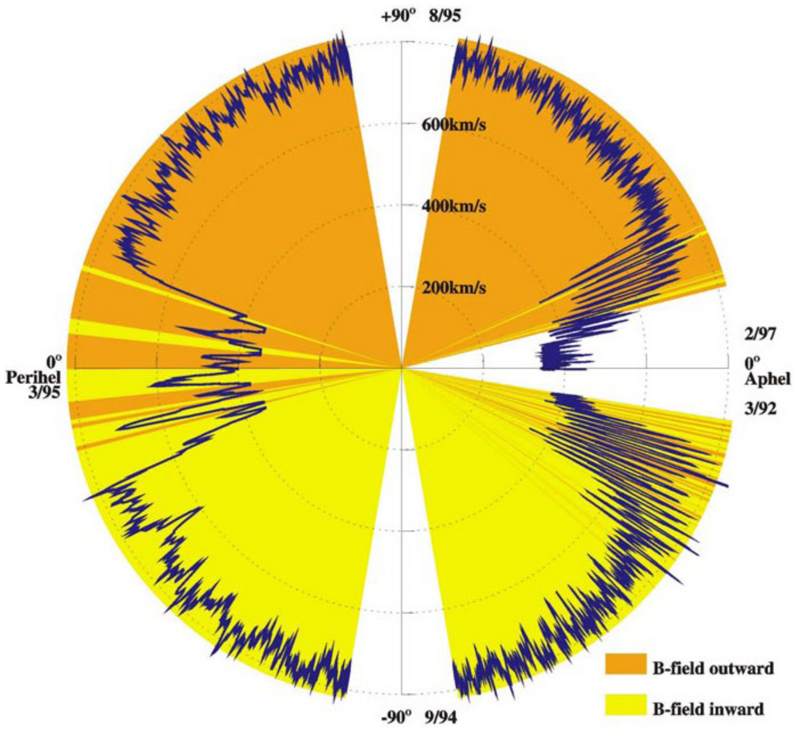

(a) Observations of polarity of the solar magnetic flux density and the solar wind velocity during the passage of *Ulysses* across both solar poles: reference Encyclopedia of Astronomy and Astrophysics (2006).

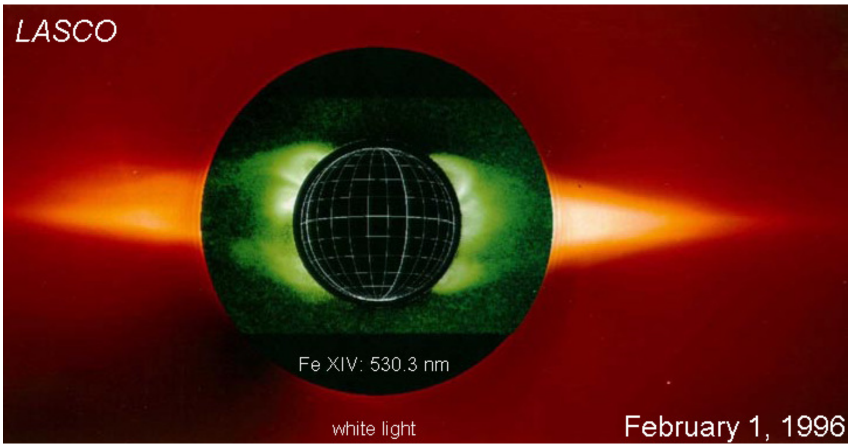

(b) A combined view of the quite corona with *SOHO*'s *LASCO* coronagraph at the extended solar minimum, composed by a green-line iron emission (*LASCO* C1) and a white-light (*LASCO* C2) image. It can be seen, how the solar corona continuously changes into the interplanetary medium; reference: Encyclopedia of Astronomy and Astrophysics (2006); Ivory (1998).

Figure 2.10: The figures present the solar wind, which is continuously streaming away from the Sun.

CHAPTER 3

The flare and other explosive solar events

For instance at the end of October 2003 and the beginning of November 2003 very huge solar eruptions were observed. In the following satellites for communication orbiting the Earth had to be shut down temporarily. Astronauts on the International Space Station were forced to stay in the strongly shielded service modules. Air planes avoided routes along high geographic latitudes and in Sweden even the electric power supply collapsed leaving about 50 000 people in temporary darkness. These events show the importance of the solar terrestrial relations for the modern human civilisation (Holman, 2006).

The reason for such regularly happening eruptions is the Sun's magnetic activity, which expresses itself on different time scales, e.g., the Schwabe and Hale cycles have been mentioned before. As stated in Chapter 2, the number of sunspots is a measure for the solar activity, and the activity in the solar atmosphere is closely related to the activity on the photosphere, since both regions are connected with each other by the magnetic field. Moreover the solar activity manifests itself in solar flares and flares are associated with restructuring of the coronal magnetic field topology.

Three different kinds of explosive solar events can be distinguished, namely solar flares, eruptive filaments or prominences, and coronal mass ejections (Schwenn, 2006; Warmuth, 2007). Due to the significance of solar flares for the thesis' topic, they are explained in detail employing the example of the solar flare from October 28, 2003. Eruptive filaments/prominences and coronal mass ejections are only briefly introduced at the end of this chapter.

3.1 Solar flare

3.1.1 Flare definition

A solar flare is defined as the sudden and quick increase in the emission of electromagnetic radiation, all over the spectrum (from the radio up to the γ-ray range). It is accompanied by local plasma heating, and mass motions (e.g., jets and coronal mass ejections). Within fractions of a second a huge amount of the flare energy is transferred into particle (primarily but not exclusively electron) acceleration. The total energy release during a large flare is estimated with about

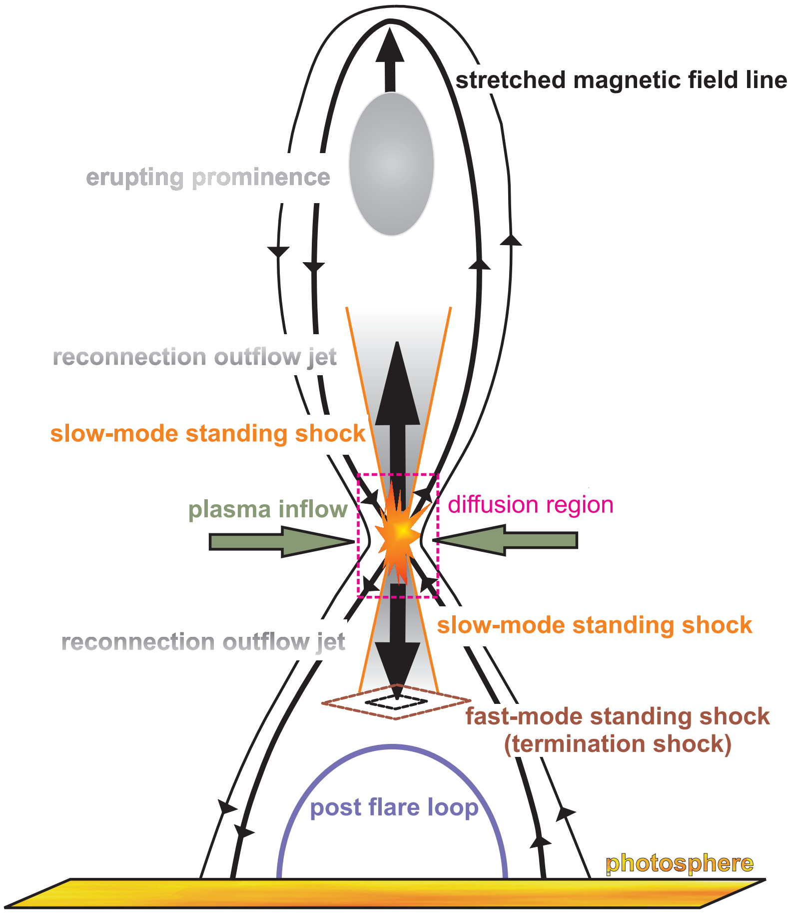

Figure 3.1: The reconnection process is illustrated schematically: A rising eruptive prominence stretches the underlying magnetic field. Magnetic reconnection occurs in the diffusion region and the slow inflowing plasma is catapulted away from the reconnection site in forms of hot jets.

10^{25} J.[1] Assuming a flare duration of ten minutes, the flare power can be estimated with about 1.7×10^{22} W. The total energy amount released during a flare in such a short time is about 200 000 times bigger, than the total worldwide energy consumption (5×10^{20} J) had been in the year 2005 (see e.g. U.S. Department of Energy, 2006).

3.1.2 Flare origin

A flare can be divided into three time phases, namely the precursor or pre-heating phase, which is followed by the impulsive phase and the gradual phase. The durations for each of these phases are different, i.e., the precursor phase lasts two minutes to five minutes but is not seen at every flare. The impulsive phase, where the sudden increase of emission takes place, lasts a few seconds up to a few minutes. Finally the gradual phase sets in, where the gradual decline lasts from several minutes up to a few hours.

In the frame of magnetic reconnection a flare can be understood in the following way (see e.g., Aschwanden, 2002a; Benz, 2008; Hudson, 2007; Karlický & Bárta, 2007; Nagashima & Yokoyama,

[1]This energy corresponds to the energy which is released by the simultaneous ignition of about 2.4×10^9 atomic bombs, if each bomb has the explosive TNT-equivalent[2] of 1 Mt. For comparison, the atomic bomb dropped by the USA on Japan (Nagasaki) on August 9, 1945 possessed a TNT-equivalent of 20 kt.

[2]Trinitrotoluol (TNT) is an explosive chemical compound which is obtained when three hydrogen atoms (H) are replaced by three nitro groups (NO_2) in the toluene molecule ($C_6H_5CH_3$).

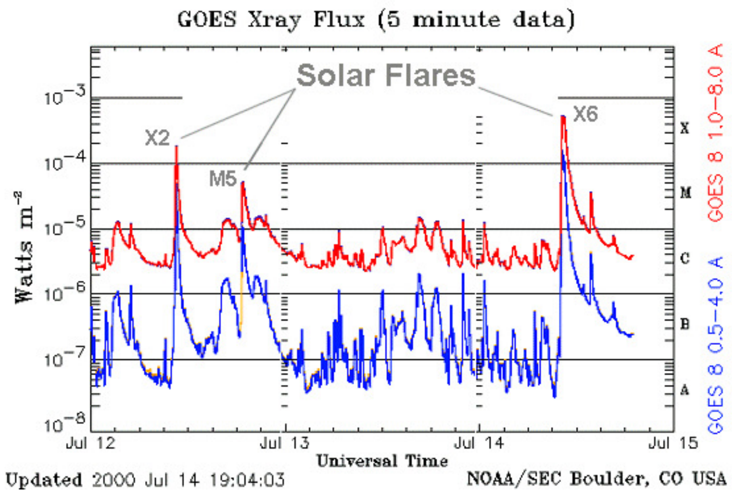

Figure 3.2: The diagram shows the *GOES* X-ray flux intensity in the time period from July 12, 2000 to July 15, 2000. In this time span a few solar flares of different strength were observed. (Courtesy of T. Phillips, reference: `http://www.spaceweather.com/glossary/images/xrays.gif`, April 2008.)

2006; Sakai & de Jager, 1996; Somov & Titov, 1985; van Hoven, 1976; Vršnak & Skender, 2005): If a prominence rises due to photospheric footpoint motion, it stretches the underlying magnetic field as seen in Fig. 3.1. Thus a current sheet establishes. If the current therein exceeds a critical value, the resistivity increases due to plasma-wave excitation originating from various instabilities (Baumjohann & Treumann, 1996; Treumann & Baumjohann, 1997). Then magnetic reconnection can occur in the region of enhanced resistivity, i.e., the diffusion region. The slowly into the diffusion region inflowing plasma shoots away from the reconnection site in forms of hot jets, due to the strong curvature of the magnetic field in the vicinity of the diffusion region.

If the velocity of these jets is above the local Alfvén velocity, a fast magnetosonic shock is established, when the jet penetrates into the surrounding coronal plasma. Forbes (1986); Shibata *et al.* (1995) predicted such a shock basing on numerical simulations. This so called termination shock is also presented in the Fig. 3.1. Tsuneta & Naito (1998) suggested the termination shock to be one generator for the highly energetic electrons produced during a flare. These particles are (gyrating and) travelling along the magnetic field lines. The electron transport in the coronal conditions considering Coulomb collisions is discussed by Önel *et al.* (2007) in more detail. If these electrons reach the dense chromosphere they can emit X-ray radiation via Bremsstrahlung processes (Brown, 1971; Kontar *et al.*, 2007).

3.1.3 Classification of flares

Flares are classified according to their X-ray brightness in the wavelength range 1 Å to 8 Å, e.g., by using the *GOES*[1] instruments (Fig. 3.2). Very small events are called A class[2] and B class flares. C class flares denote larger, but still small events. M class flares are moderate, and the X class[3] is used for extremely large flares. As presented (Fig. 3.2) these classes are logarithmically defined, hence one X class flare is 10 times stronger than one M class flare. Additionally each of these classes is divided into nine subclasses, i.e., (see the examples in Fig. 3.2) a X6 class flare (flux intensity: $6 \times 10^{-4}\,\mathrm{W/m^2}$) is 3 times stronger than a X2 class flare (flux intensity: $2 \times 10^{-4}\,\mathrm{W/m^2}$), which again is 4 times stronger than a M5 class flare (flux intensity: $5 \times 10^{-5}\,\mathrm{W/m^2}$).

[1] *GOES* stands for "Geostationary Operational Environmental Satellite", see `http://www.swpc.noaa.gov/`.
[2] Flux intensities of A class flares are between $[10^{-8}\,\mathrm{W/m^2}, 10^{-7}\,\mathrm{W/m^2})$.
[3] Flux intensities of X class flares are between $[10^{-4}\,\mathrm{W/m^2}, 10^{-3}\,\mathrm{W/m^2})$.

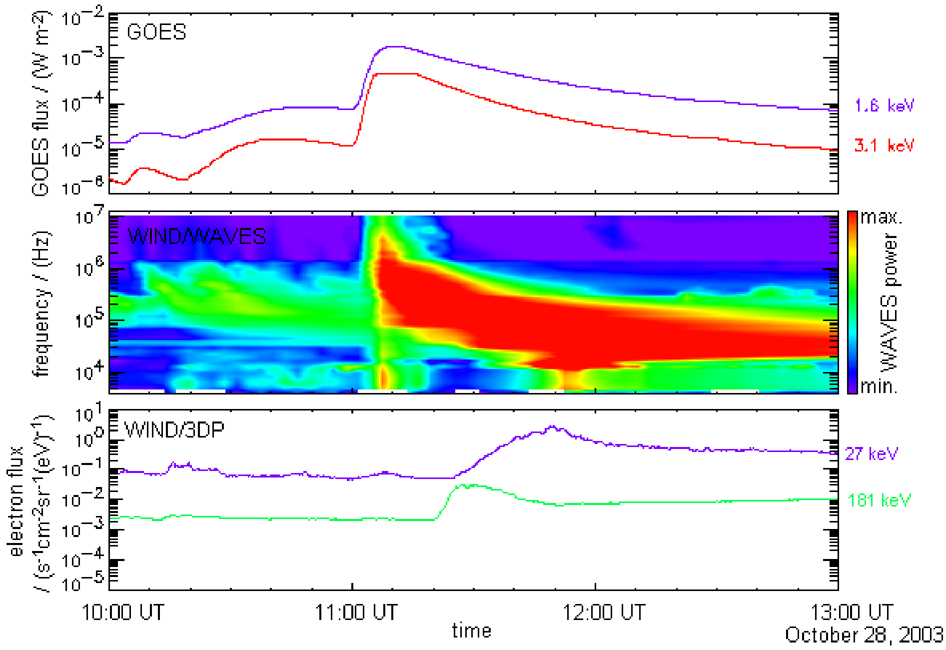

Figure 3.3: Three diagrams showing the emissions during the solar flare on October 28, 2003: The top panel presents the *GOES* X-ray fluxes around 1.6 keV (blue curve) and 3.1 keV (red curve). The panel in the middle shows a dynamic radio spectrum observed by *WIND*. The radio sources intensities are colour coded, and the frequency covers the range from around 20 kHz to 14 MHz. The lower panel shows fluxes of the energetic electrons observed by *WIND* at about 1 AU away from the Sun with energies around 27 keV (blue curve) and 181 keV (cyan curve). All three panels represent their data in dependence on the same time axis. (Courtesy of G. Mann and A. Warmuth.)

3.1.4 Flare example

On October 28, 2003 one of the largest (i.e., X17.2 class) flares observed until now occurred. Subsequently this flare and the related active region NOAA AR 10486 (*MDI* data related with this event is presented in Fig. 3.7(b) on pg. 21; a white-light continuum image of this active region is illustrated in Fig. 5.2(a) on pg. 33) has been analysed in many aspects (see e.g., Aurass *et al.*, 2007, and the references therein). The special event on October 28, 2003 is employed here, since it is a typical case of a large flare that has been closely investigated. Consequently, the presented results are not only valid for this special event, but for general solar flare physics.

As it can be seen in Fig. 3.3 (upper panel), the flare on October 28, 2003 is related with a strong enhancement of the solar X-ray flux at shortly after 11:00 UT. At the same time the dynamic radio spectrum shows enhanced radio emissions.

Important information about the parameters of the flare plasma can be derived from a dynamic radio spectrum. In a dynamic radio spectrum, such as the one presented in Fig. 3.3 (panel in the middle), the intensity of the radio source (colour-coded) is plotted as a function of the radio frequency (on the ordinate) and the time (on the abscissa). Sometimes also the polarity of the radio signals is recorded. The non-thermal radio radiation in the decimetre and metre wave range is generated by plasma emission. Therefore the radio frequency is directly related to the electron plasma frequency ($f_{\rm pl}$, see Eq. (A.2), pg. 79), which is directly proportional to the square root of the local electron number density $N_{\rm e}$, i.e., $f_{\rm pl} \sim \sqrt{N_{\rm e}[r]}$. If a gravitationally stratified density model for the solar atmosphere is taken into account (e.g., see Sect. 4.2, pg. 26) the electron plasma frequency in the dynamic radio spectrum can be expressed by the heliocentric radial distance r of the radio source. Hence it is possible to track the motion of disturbances in the solar and

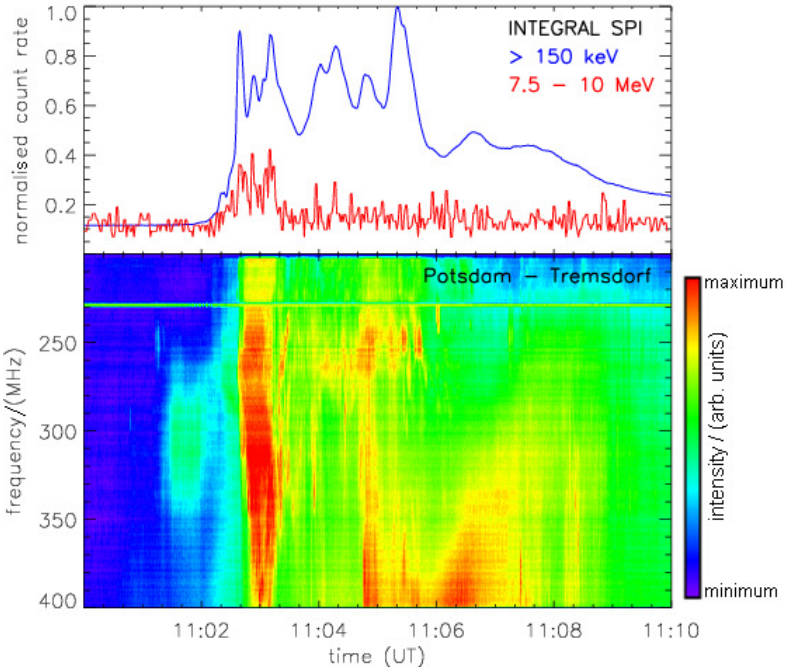

Figure 3.4: Two diagrams presenting data from the solar flare on October 28, 2003: The top panel illustrates the *INTEGRAL* γ-ray & X-ray fluxes. The red curve shows the count rates for those highly energetic photons (γ-rays) with energies in the range of 7.5 MeV to 10 MeV. The blue curve shows those energetic photons (X-rays) with energies above 150 keV. Both curves are normalised to the maximum value of the blue curve. In the lower panel a dynamic radio spectrum in the frequency range of 200 MHz to 400 MHz with colour coded intensity is presented. The radio data is recorded by the radiospectralpolarimeter located in the Tremsdorf observatory of the Astrophysical Institute Potsdam. Both panels represent their data in dependence on the same time axis. (Courtesy of G. Mann and A. Warmuth.)

interplanetary atmosphere by converting the dynamic radio spectrum into height-time diagrams. The radio spectrum in Fig. 3.3 therefore covers the range from 2.25 $R_\odot$ from the centre of the Sun (Mann *et al.*, 1999), up to approximately 1 AU where *WIND*[1] spacecraft is located. The type III radio bursts seen in the radio diagram in Fig. 3.3 indicate that fast electrons travel through the coronal and interplanetary plasma, which excite plasma oscillations leading to the generation of these radio signatures.

In the lower panel of Fig. 3.3 the electron fluxes measured by *WIND* at around 1 AU are illustrated. It can be seen that at about 11:30 UT the highly energetic electrons have traversed the interplanetary space, and have reached the *WIND* spacecraft were they were detected. Note the velocity dispersion, i.e., those electrons with higher energies (cyan curve) reach the *WIND* spacecraft earlier than those with less energies (blue curve).

In Fig. 3.4 γ-ray & X-ray data from *INTEGRAL*[2] spacecraft and ground based radio data from the radiospectralpolarimeter of the Astrophysical Institute Potsdam are plotted simultaneously. The time period covers the initial phase of the flare: The strong enhancement of the γ-ray & X-ray flux indicates the presence of highly energetic electrons (Kiener *et al.*, 2006). At the same time the dynamic radio spectrum shows the appearance of enhanced radio emissions.

This proves that the Sun acts as a gigantic particle accelerator in space (see e.g. Aschwanden, 2002a; Heber *et al.*, 2007; Mann, 2007).

[1] More information about the *WIND* spacecraft can be found at `http://pwg.gsfc.nasa.gov/istp/wind/`.

[2] *INTEGRAL* stands for "International Gamma-Ray Astrophysics Laboratory", see `http://www.esa.int/SPECIALS/Integral/`.

3.2 Production of energetic particles

As explained during explosive events charged particles are accelerated to relativistic energies within fractions of a second. The acceleration mechanisms are still not fully understood. Beside mechanical (e.g., collisions with electrically neutral particles) and Coulomb collisions, charged particles can gain energy only by electric field acceleration. In view of this fact, several different electric field acceleration mechanisms remain possible, differing only in the manner of creation and strength of the field. Nevertheless all different mechanisms have to satisfy the constraints obtained by observations of parameters such as, time-scales, energies, and total number of accelerated particles.

Several groups of mechanisms can be distinguished from one another and are discussed in the community, e.g.,

- ◇ acceleration at local DC electric fields in the diffusion region of the magnetic reconnection site (e.g., Benz, 1987; Holman, 1985; Litvinenko, 2000),
- ◇ acceleration at shock waves as a result of a blast wave and/or driven by a coronal mass ejection (e.g., Holman & Pesses, 1983; Mann & Classen, 1995; Mann *et al.*, 2001),
- ◇ stochastic acceleration via wave particle interaction (e.g., Melrose, 1994; Miller *et al.*, 1997; Miteva, 2007; Miteva & Mann, 2005, 2007; Miteva *et al.*, 2007),
- ◇ acceleration at the shock wave in the outflow region of the reconnection site (e.g., Aurass & Mann, 2004; Aurass *et al.*, 2002; Forbes, 1986; Mann *et al.*, 2006; Somov & Kosugi, 1997; Tsuneta & Naito, 1998).

3.2.1 Energetic electrons

Due to better observational instruments all models for particle acceleration are continuously improved. For instance, for a long time it was not clear, where the acceleration sites were located. This question could be attended to, when *Yohkoh* and *CGRO* [1] were launched in 1991 for the first time. Currently *RHESSI*[2] is and in future *SolO* [3] will become of major importance for the investigation of the particle acceleration mechanisms.

As already mentioned, during solar flares electrons and ions are accelerated up to relativistic energies (see e.g., Emslie *et al.*, 2004). These particles propagate along the magnetic field lines. If they reach the lower and thus denser solar atmosphere with sufficiently high energy, they can produce hard X- and γ-ray radiation (Brown, 1971, 1972). In order to investigate the acceleration process *RHESSI* was designed.

NASA's *RHESSI* satellite is the sixth mission in the line of NASA's small explorer missions (Lin *et al.*, 2002). *RHESSI*'s primary mission objective is to explore the basic physics of particle acceleration and explosive energy release in solar flares. It is equipped with an imaging system, capable to detect the highly energetic electromagnetic radiation emitted during solar flares, i.e., from soft X-rays ($\approx 3\,\mathrm{keV}$) up to γ-rays ($\approx 20\,\mathrm{MeV}$). Moreover it is able to perform highly resolved spatial and spectral spectroscopy.

The non-thermal X-ray radiation during flares is produced via Bremsstrahlung processes by the highly energetic electrons propagating through the dense chromosphere. Hence the X-ray photon spectrum (see Fig. 3.5) is related to the spectrum of the accelerated electrons.

What is known from radio observations?

Radio observations provide the only method to track fast electrons passing through the solar and interplanetary atmosphere in real time.

[1] *CGRO* stands for "Compton Gamma Ray Observatory", see `http://cossc.gsfc.nasa.gov/`.
[2] *RHESSI* stands for "Ramaty High Energy Solar Spectroscopic Imager", see `http://hessi.ssl.berkeley.edu/` or `http://hesperia.gsfc.nasa.gov/hessi/`.
[3] *SolO* stands for "Solar Orbiter". This spacecraft is scheduled to launch in the second decade of the 21st century.

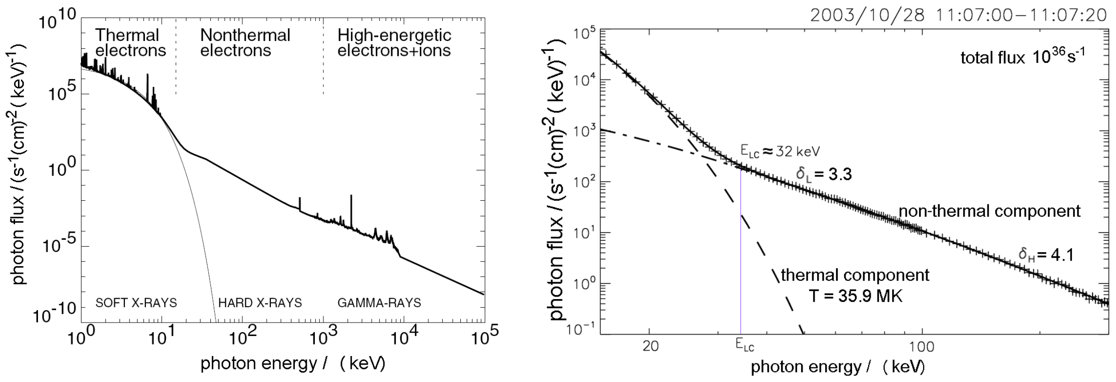

(a) A model of a photon spectrum of a large flare is presented. It extends from soft X-rays (1 keV to 10 keV), hard X-rays (10 keV to 1 MeV), to γ-rays (1 MeV to 10 GeV). It is composed by thermal, non-thermal (energetic), or high-energetic electrons. The γ-ray line emission and parts of the γ-ray continuum are generated by interactions of protons, neutrons, ions, and pion decay; reference: Encyclopedia of Astronomy and Astrophysics (2006)

(b) A real photon spectrum of the flare from October 28, 2003 is presented. The dashed curve shows the thermal and the dashed-dotted curve the non-thermal component. The observed photon flux is represented by the full curve. (Courtesy of A. Warmuth.)

Figure 3.5: A real and a theoretical photon spectrum during a flare is presented.

Radio emissions below 1 GHz are predominantly generated by collective plasma emission. Such emissions occur if the equilibrium in the plasma is disturbed, e.g., by an electron beam passing through the plasma. This excites Langmuir oscillations in the plasma and causes the emission of radio radiation.

An example is presented in the dynamic radio spectrum in Fig. 3.6: The data therein has been observed at the Astrophysical Institute Potsdam's radio observatory in Tremsdorf[1]. The frequencies are recorded on March 11, 1999 in the range from 110 MHz to 400 MHz and are plotted versus the time period of 8:18:50 UT to 8:19:05 UT. This spectrum contains one type III burst originating at 370 MHz and 8:19:51.5 UT. It also contains a second faint type III burst starting at the 320 MHz level at 8:19:55.5 UT, which is superimposed by a type U burst. While the type III

Table 3.1: Plasma parameters, obtained using a $\alpha = 4$-fold coronal density model for three different electron plasma frequencies. The quantities in the table are explained in Appendix A (pg. 79).

f_{pl} in MHz	r in $R_\odot$	N_{total} in m^{-3}	N_{e} in m^{-3}	B in T	β_{pl}
110	1.4639	2.89×10^{14}	1.5×10^{14}	1.58×10^{-4}	5.57×10^{-1}
300	1.1301	2.15×10^{15}	1.12×10^{15}	1.06×10^{-3}	9.15×10^{-2}
400	1.0608	3.82×10^{15}	1.98×10^{15}	3.33×10^{-3}	1.66×10^{-2}
f_{pl} in MHz	r in $R_\odot$	$v_{\mathrm{Alfvén}}$ in m s^{-1}	f_{cyc} in MHz	r_{Larmor} in m	λ_{Debye} in m
110	1.4639	2.62×10^{5}	2.38×10^{-6}	3.07×10^{5}	6.65×10^{-3}
300	1.1301	6.47×10^{5}	1.6×10^{-5}	4.56×10^{4}	2.44×10^{-3}
400	1.0608	1.52×10^{6}	5.02×10^{-5}	1.46×10^{4}	1.83×10^{-3}

[1] More information about the Tremsdorf Radio Observatory of Astrophysical Institute Potsdam can be found at `http://www.aip.de/groups/osra/`.

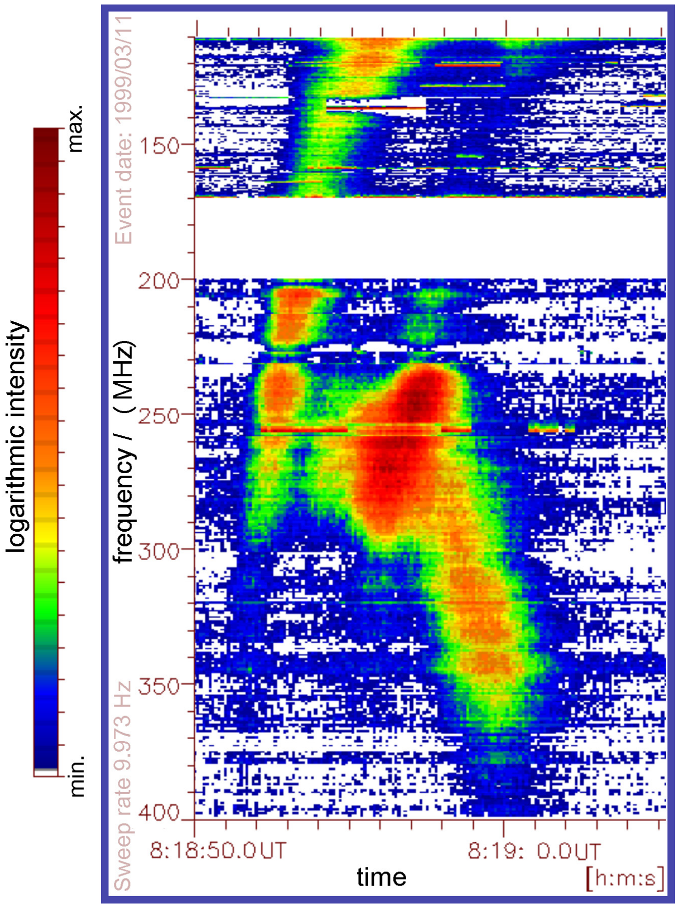

Figure 3.6: Dynamical radio spectrum of an event from March 11, 1999 obtained by the Radio Sweep Spectropolarimeter (Mann *et al.*, 1992) at the Astrophysical Institute Potsdam (AIP) in Tremsdorf. The frequency is shown on a reversed axis in dependence on time, whereas the radiation intensities are colour coded (Önel, 2004).

bursts are generated by fast electrons drifting outward along open field lines, the type U bursts are assumed to be created by fast drifting electrons in closed magnetic field structures (Yokoyama *et al.*, 2002). In such a case, the electrons also produce radio continuum radiation in terms of so-called type IV radio bursts (see e.g., Robinson, 1996, as a review).

Using an average model for the magnetic flux density and the electron number density in the corona (as the models introduced in Chapter 4) the local plasma conditions in the vicinity of the radio sources can be determined, see Table 3.1. The quantities in the table are explained in Appendix A where also tables for other conditions can be found.

Radio observations (such as in Fig. 3.6) indicate, that the site for the energy release during a flare is located at about the $f_{\rm pl} \approx 300\,\rm MHz$ level (Aschwanden *et al.*, 1995b).

What did *RHESSI* reveal?

In the course of solar flares a large amount of energy is suddenly released and transferred into local heating of the coronal plasma, mass motions (e.g., jets and coronal mass ejections), enhanced emission of both electromagnetic radiation (from the radio- up to the γ-ray range) and energetic particles (i.e., electrons, protons, and heavy ions). Energetic electrons play an important role, since they are responsible for the non-thermal radio and X-ray emission of the Sun, which can be seen by e.g., *RHESSI* observations. In addition, they carry a substantial part of the released flare

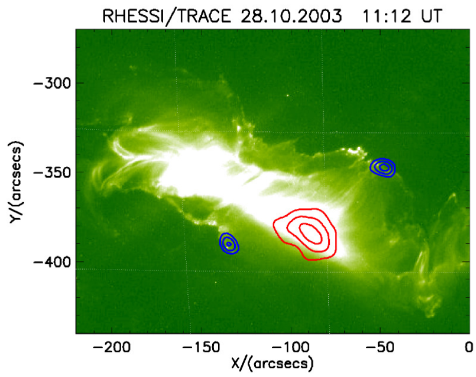

(a) The figure shows a flare ribbon as observed by *TRACE* spacecraft on October 28, 2003. The contour plots are obtained by *RHESSI*, i.e., the loop-top soft X-ray source is located in the middle (red contour lines) and the footpoint hard X-ray sources are located beside the loop-top source (blue contour lines). The related *MDI* data is presented in Fig. 3.7(b).

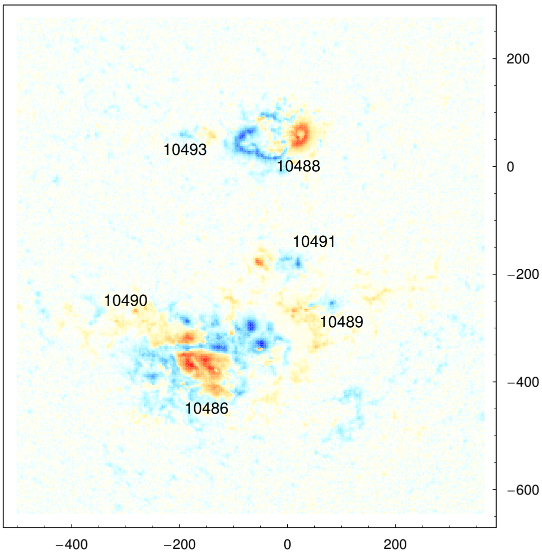

(b) *MDI* diagram from October 28, 2003 recorded at 11:11 UT. The horizontal axis represents the West-East direction, whereas the vertical axis represents the North-South direction. The solar disc's centre is located at $(0, 0)$ and the axes' units are arc seconds. The active regions visible are numbered and are colour coded according to their magnetic polarity: Blue corresponds to southern and red corresponds to northern polarity. Reference: Rausche (2008).

Figure 3.7: *MDI*, *TRACE* and *RHESSI* data from October 28, 2003 are presented.

energy (Emslie *et al.*, 2004; Lin, 1974; Lin & Hudson, 1971). *RHESSI* observations show that highly energetic ($\geq 20\,\mathrm{keV}$) electron fluxes F_e that are produced during a flare, are of the order of $F_\mathrm{e} \approx 10^{36}\,{}^{\mathrm{electrons}}/_{\mathrm{s}}$ and are related to a power P_e of about $P_\mathrm{e} \approx 10^{22}\,\mathrm{W} = 10^{29}\,{}^{\mathrm{erg}}/_{\mathrm{s}}$ (Heyvaerts, 1974; Lin *et al.*, 2002; Smith & Smith, 1963; Warmuth *et al.*, 2007).

How so many electrons are accelerated up to high energies within fractions of a second is still under discussion. Basing on average observations of *RHESSI* (as the numbers mentioned above) the following conclusions can be drawn. The average kinetic energy $\overline{W}$ of one energetic electron can be estimated with

$$\overline{W} \approx \frac{P_\mathrm{e}}{F_\mathrm{e}} = \frac{10^{22}\,\mathrm{W}}{10^{36}\,\mathrm{s}^{-1}} \approx 62.4\,\mathrm{keV}, \tag{3.1}$$

corresponding to an average velocity $\overline{V} = 0.454\,c \approx 136\,{}^{\mathrm{Mm}}/_{\mathrm{s}}$, where c represents the speed of light. Figure 3.7(a) shows an image taken by NASA's *TRACE* spacecraft[1] from the active region on October 28, 2003. X-ray contour plots observed by *RHESSI* are drawn into the image, i.e., the loop-top soft X-ray source is located in the middle of the picture, whereas the footpoint hard X-ray sources are located beside the loop-top source. Each one of these hard X-ray sources has a diameter of about $d_\mathrm{s} = 10\,\mathrm{Mm}$, i.e., hence each source area (if a circular shape is assumed) is $A_\mathrm{s} = 7.85 \times 10^{13}\,\mathrm{m}^2$. Both hard X-ray sources are separated from one another by about $L_\mathrm{s} = 70\,\mathrm{Mm}$. If it is assumed that both hard X-ray footpoints are located at the same height above the photosphere and belong to one circular magnetic field line, then this magnetic loop would have an arc length of $L_\mathrm{co} = {}^{(\pi L_\mathrm{s})}/_{2} \approx 110\,\mathrm{Mm}$. The electron density N_acc of the accelerated electrons

[1]Transition Region and Coronal Explorer

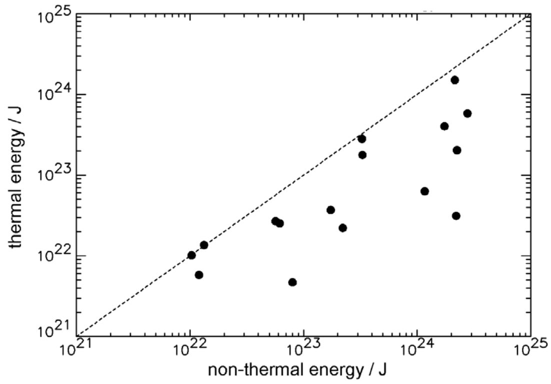

Figure 3.8: The dots in the diagram present the total energy output of 16 different flares measured by *RHESSI*, and the dashed line presents the identity function. The diagram leads to the conclusion that the fraction of the released flare energy, which is transferred into the non-thermal electrons is from the same order of magnitude as the energy transferred into thermal energy. (Courtesy of A. Warmuth.)

can also be retrieved from *RHESSI* observations, i.e.,

$$N_{\mathrm{acc}} \approx \frac{F_{\mathrm{e}}}{(2A_{\mathrm{s}})\,\overline{V}} = 1.17 \times 10^{13}\,\mathrm{m}^{-3}. \tag{3.2}$$

The 2 in the denominator of Eq. (3.2) originates from the fact that *RHESSI* usually observes two hard X-ray sources at the footpoints (as it can be seen in Fig. 3.7(a)). By assuming a typical electron density $N_{\mathrm{co}} = 10^{15}\,\mathrm{m}^{-3}$ in the flare region (see e.g., Aschwanden, 2002b), i.e., considering the density corresponding to the electron plasma frequency of about 284 MHz, it can be seen that only a fraction of the available electrons is finally accelerated, i.e.,

$$N_{\mathrm{acc}} \approx 1.2\%\, N_{\mathrm{co}}. \tag{3.3}$$

However the energy contained in the accelerated electrons in comparison to the thermal energy of the electrons in the flare region can be estimated by

$$\left.\frac{N_{\mathrm{acc}}\overline{W}}{\frac{3}{2}\,N_{\mathrm{co}}k_{\mathrm{B}}T}\right|_{T=40\,\mathrm{MK}} \approx 14.1\%. \tag{3.4}$$

The quantity k_{B} stands for Boltzmann's constant.[1] Here a typical flare temperature $T = 40\,\mathrm{MK}$ has been adopted, which is a value obtained from the photon fluxes observed by *RHESSI* (Warmuth *et al.*, 2007). Of course these values represent only rough estimates, but in summary, this example illustrates that at the flare peak only a small fraction (e.g., about 1%) of electrons are really accelerated up to high energies in the flare region, but these electrons carry a substantial part (e.g., about 14%) of the total electron energy (Benz *et al.*, 2007). Indeed if the whole flare duration is considered then *RHESSI* observations propose that the energy transferred into the non-thermal electrons is from the same order of magnitude as the released thermal energy (see Fig. 3.8). This is the reason why the electron acceleration process is of major interest for the understanding of solar flares (Emslie *et al.*, 2004; Lin & Hudson, 1971, 1976).

3.3 Filament eruption/Prominence eruption

Clouds of relatively cool and dense solar atmosphere seen above the solar disc are called filaments, while the same clouds located at the solar limb are named prominences. Hence a filament is

[1] All natural constants used within this Thesis are chosen according to the recommendations of Mohr *et al.* (2007).

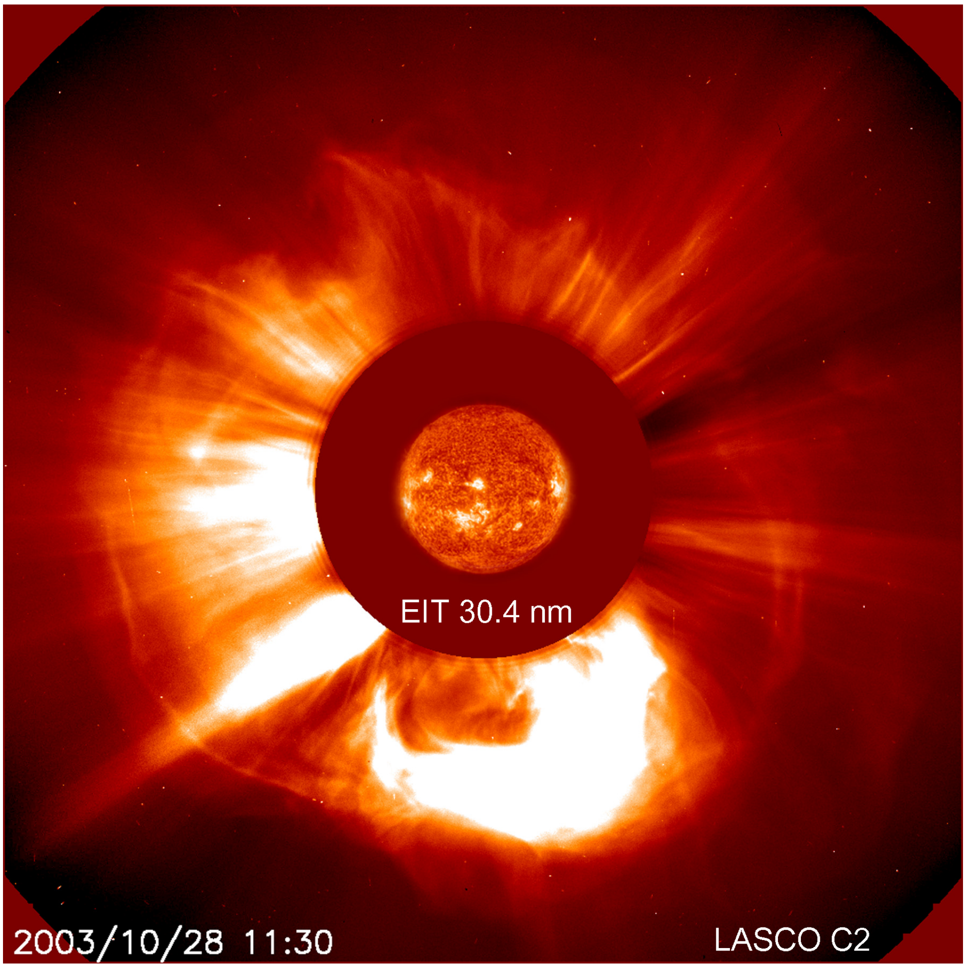

Figure 3.9: *LASCO C2* image from the October 28, 2008 event related with the active region NOAA AR 10486. In the centre an *EIT* (304 Å) picture is included. The picture shows a fast moving coronal mass ejection, which hit Earth early on October 29, 2008.; reference: *SOHO* webpage (2008).

a synonymous terminology for a prominence. As an example Fig. 2.8 (pg. 11) shows a huge prominence.

Filaments are suspended above magnetic flux tubes, indeed the magnetic fields thread them through and balance the force of gravity. These structures have lifespans up to months, and experience only little changes on the time-scale of days. Due to the magnetic fields the heat flow into the flux tubes from the surrounding corona is inhibited, this is why the tubes are cooler than the surrounding corona. Since filaments absorb most of the photons from the underlying chromosphere, and re-emit them in all directions, they appear darker against the chromosphere, but brighter against the dark sky.

Stationary filaments are located almost parallelly above magnetic neutral lines which they follow. As already explained, the magnetic neutral line is a line which separates regions of two different magnetic polarities on the photosphere from one another, e.g., the dashed orange line in Fig. 5.1(a) (pg. 32) represents such a neutral line.

Sometimes the filament becomes unstable and expands explosively. In such a circumstance the sudden expansion catapults the filament matter outwards with velocities from 10 $^{km}/_{s}$ to 100 $^{km}/_{s}$. Many filament eruptions are accompanied by solar flares.

3.4 Coronal mass ejection

A coronal mass ejection (hereafter CME) is comparable with the prominence or filament eruption, but much stronger. Figure 3.9 shows a typical CME.

During a CME a large amount of matter (about 10^{13} kg) is ejected into interplanetary space with velocities between 100 km/s to 2 500 km/s (Gallagher *et al.*, 2003; Yashiro *et al.*, 2004).[1] This process lasts from a few hours up to a few days. Even though many CMEs are accompanied by the flares (see Sect. 3.1), both events seem to be independent from one another, Yashiro *et al.* (2005) found that about 20% of the C class flares are accompanied by relatively slow (velocities of about 430 km$s$) CMEs, whereas all flares X class are associated with very fast (velocities of about 1 600 km$s$) CMEs. It is believed that the origin for CMEs lies in large-scale instabilities of the magnetic structures.

Considering the CME size, mass and the frozen-in magnetic field carried within them, such events can generate significant geomagnetic storms when they interact with the Earth's magnetosphere.

[1] The "*SOHO LASCO* CME catalog" can be found at `http://cdaw.gsfc.nasa.gov/CME_list`, April 2008.

CHAPTER 4

The magnetic flux and coronal density

Radio observations are one of the most important tools in solar physics. It is not easy to interpret these observations correctly, and therefore a successful observer needs to have much experience and additional knowledge about the local plasma conditions in the vicinity of the radio sources.

These plasma conditions (e.g., plasma composition, plasma density, and local magnetic field strength) are important input parameters, essentially needed for the correct interpretation of the solar radio signals. Exactly there lies the problem: As already explained the solar corona is the outer layer of the solar atmosphere. Figure 2.6 (pg. 11) sketches the magnetic field topology therein. The corona is highly structured in temporal and spatial ways and therefore the local plasma conditions are highly variable.

One way of dealing with this problem is to introduce average values for the magnetic flux density strength and plasma density: Empiric models for the coronal magnetic flux density and the coronal electron number density are presented in this chapter. With these models average values for the plasma parameters can be estimated (see Appendix A).

4.1 Model for the coronal magnetic field

The magnetic field is highly structured in the corona and therefore difficult to handle. Figure 2.6 (pg. 11) illustrates how the field topology may look like. This is a big problem, if highly accurate estimations for the magnetic field in the corona are needed. Nevertheless it proved to be useful, to estimate the strength of the magnetic flux density in the solar corona with average values.

Dulk & McLean (1978) proposed an empirical relation for the average value of the magnetic flux density B depending on the heliocentric radial distance r. Basing on several different observational methods they found

$$B = B_0 \left(\frac{r}{R_\odot} - 1 \right)^{-3/2} \quad \text{for} \;\; 1.02\, R_\odot \lesssim r \lesssim 10\, R_\odot, \tag{4.1}$$

with $B_0 = 5 \times 10^{-5}\,\mathrm{T} = 0.5\,\mathrm{G}$.

Equation (4.1) is presented in Fig. 4.1. As discussed by e.g., Önel (2004) this model can even be expanded into the interplanetary space if just a few modifications are made.

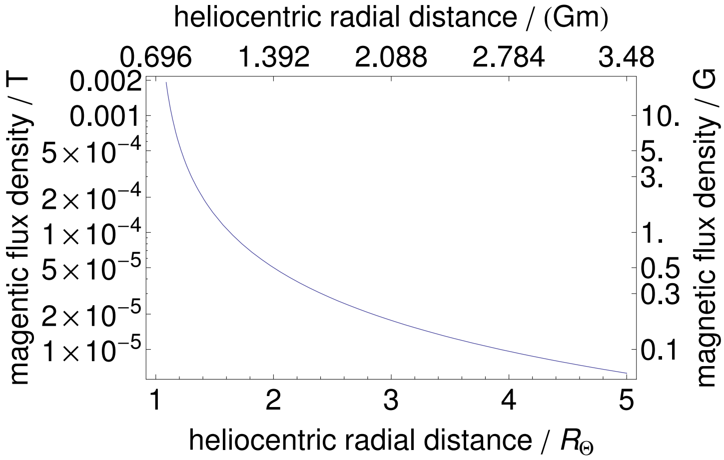

Figure 4.1: The empirically found magnetic flux density model of Dulk & McLean (1978) is plotted in dependence on the heliocentric distance.

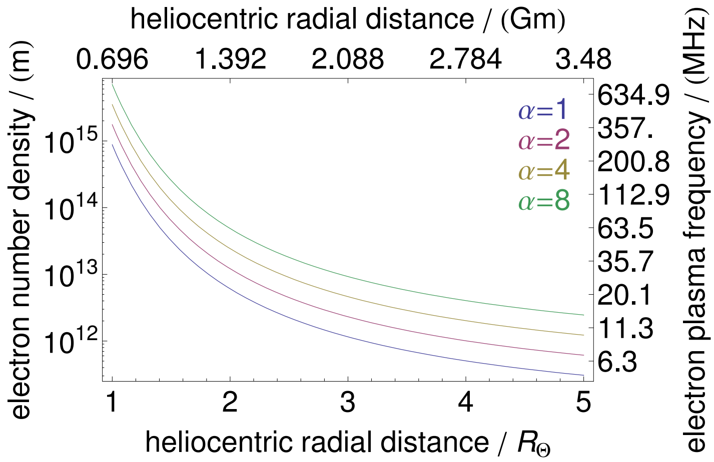

Figure 4.2: An average coronal electron number density model for several different Newkirk parameter α is plotted in dependence on the heliocentric distance. Additionally the electron plasma frequency dependence on the heliocentric height is visualised.

4.2 Model for the coronal density

As the magnetic field, the plasma density in the corona is strongly variable. Nevertheless the coronal density is an important plasma parameter which is needed for almost every kind of calculation. Hence an average barometric model is introduced in the following, which can be used to obtain average coronal densities.

Starting from the spherical symmetrical momentum equation

$$\begin{aligned}\rho_{\mathrm{co}}\frac{\mathrm{d}\vec{v}_{\mathrm{co}}}{\mathrm{d}t} &= \rho_{\mathrm{co}}\left(\frac{\partial\vec{v}_{\mathrm{co}}}{\partial t}+(\vec{v}_{\mathrm{co}}\cdot\nabla_r)\,\vec{v}_{\mathrm{co}}\right)\\ &= -\nabla_r p_{\mathrm{co}}-\rho_{\mathrm{co}}\frac{GM_\odot}{r^2}\,\vec{e}_{\mathrm{r}},\end{aligned} \tag{4.2}$$

where G, $M_\odot$ represent the Newtonian constant of gravitation and the solar mass, respectively. The time is symbolised by t, and $\vec{e}_{\mathrm{r}}$ is the unit vector pointing along the radial direction away from the solar centre, whereas the other quantities ρ_{co}, p_{co}, $\vec{v}_{\mathrm{co}}$, r correspondingly stand for the coronal gas density, the gas pressure, the radial plasma flow velocity vector, and the heliocentric radial distance. Assuming that the coronal plasma is composed of electrons and protons only, the plasma density can be expressed as

$$\rho_{\mathrm{co}} = \sum_{\varsigma} m_{\varsigma} N_{\varsigma} = m_{\mathrm{e}} N_{\mathrm{e}} + m_{\mathrm{p}} N_{\mathrm{p}}. \quad (4.3)$$

Here the quantities N_ς, m_ς represent the particle number density and the mass of the particle species $\varsigma \in \{$"e" for electron, "p" for proton$\}$, respectively. Considering the quasi electric neutrality $N_{\mathrm{e}} \approx N_{\mathrm{p}}$ of the plasma, the equation of state can be formulated

$$p_{\mathrm{co}} = k_{\mathrm{B}} T \left(N_{\mathrm{e}} + N_{\mathrm{p}}\right) = 2 k_{\mathrm{B}} T N_{\mathrm{e}}. \quad (4.4)$$

Here k_{B} and T denote the Boltzmann constant and the plasma temperature, respectively. By inserting the equation of state and Eq. (4.3) into Eq. (4.2), and taking an isothermal plasma ($\nabla_r T = \vec{0}$) as well as a static corona ($\mathrm{d}v_{\mathrm{co}}/\mathrm{d}t = 0$) into account,

$$0 = -2 k_{\mathrm{B}} T \frac{\mathrm{d}N_{\mathrm{e}}}{\mathrm{d}r} - \left(m_{\mathrm{e}} + m_{\mathrm{p}}\right) N_{\mathrm{e}} \frac{G M_\odot}{r^2} \quad (4.5)$$

is obtained. Introducing the abbreviation $\mathcal{K}_1 = (G M_\odot \, (m_{\mathrm{e}} + m_{\mathrm{p}}))/(2 k_{\mathrm{B}} T)$ during the integration of Eq. (4.5), the dependency of the electron particle number on the heliocentric distance is found to be

$$N_{\mathrm{e}} = N_0 \exp\left[\frac{\mathcal{K}_1}{R_\odot} \left(\frac{R_\odot}{r} - 1\right)\right], \quad (4.6)$$

where N_0 represents the density at the heliocentric distance $r = R_\odot$, i.e., at the base of the corona. Comparing Eq. (4.6) with the empirical α-fold Newkirk (1961) model

$$N_{\mathrm{e,Newkirk}} = \alpha \, 4.2 \times 10^{10 + 4.32 \frac{R_\odot}{r}} \,\mathrm{m}^{-3}, \quad (4.7)$$

$N_0 = \alpha \, 8.77504 \times 10^{14}\,\mathrm{m}^{-3}$ is obtained. The Newkirk scaling factor α for the density model allows to adjust the density model to the present conditions on the Sun (Koutchmy, 1994): It is chosen to be 1 in the case of a quiet Sun (very little magnetic activity at the equatorial regions). It is chosen to be 4 in the case of an active Sun, and 10 in the case of the presence of dense coronal loop structures. A moderate choice of $\alpha = 4$ for the scaling parameter has been made in most of the cases presented in this thesis. By further comparison it can be seen that the Newkirk model Eq. (4.7) agrees with Eq. (4.6), which describes an isothermal, static, and spherical symmetric corona, which has the temperature of $1.16 \times 10^6\,\mathrm{K}$.

If a more realistic coronal composition, i.e., a plasma composed by 52% electrons[1], 44% protons[2], and 4% α-particles[3], i.e., the composition corresponding to a mean molecular weight of about $m_{\mathrm{MMW}} = 0.6$ (see pg. 82, Priest, 2000), is considered (Önel, 2004), then $p_{\mathrm{co}} = (k_{\mathrm{B}} T N_{\mathrm{e}})/\mathcal{K}_2$, $\rho_{\mathrm{co}} = (m_{\mathrm{MMW}} m_{\mathrm{p}} N_{\mathrm{e}})/\mathcal{K}_2$, and $\mathcal{K}_1 = (m_{\mathrm{MMW}} m_{\mathrm{p}} G M_\odot)/(k_{\mathrm{B}} T)$ are obtained. Here the abbreviation $\mathcal{K}_2$ represents the ratio of the electron number density and the total particle number density. In such a case, the comparison with Eq. (4.7) delivers the coronal temperature of $1.39 \times 10^6\,\mathrm{K}$ (Mann *et al.*, 1999). Figure 4.2 presents the electron number density height profile for several different values of α.

The densities for the lower solar atmosphere predicted by this barometric density model are in good agreement with those proposed by Vernazza *et al.* (1981). However the Newkirk (1961) model does not accurately describe the electron number density in the higher solar atmosphere. In those heights the solar wind cannot be neglected and therefore density models, such as Mann *et al.* (1999) should be considered instead of the Newkirk (1961) model.

[1] The electron concentration for a given mean molecular weight of $m_{\mathrm{MMW}} = 0.6$ in an electron, proton, α-particle plasma is found to be $\mathcal{K}_2 = (m_\alpha + m_{\mathrm{p}} (m_{\mathrm{MMW}} - 2))/(m_{\mathrm{e}} + 2 m_\alpha - 3 m_{\mathrm{p}}) \approx 52\%$. Here m_α stands for the mass of the α-particle.

[2] The proton concentration for a given mean molecular weight of $m_{\mathrm{MMW}} = 0.6$ in an electron, proton, α-particle plasma is found to be $(2 m_{\mathrm{e}} + m_\alpha - 3 m_{\mathrm{p}} m_{\mathrm{MMW}})/(m_{\mathrm{e}} + 2 m_\alpha - 3 m_{\mathrm{p}}) \approx 44\%$. Here m_α stands for the mass of the α-particle.

[3] The α-particle concentration for a given mean molecular weight of $m_{\mathrm{MMW}} = 0.6$ in an electron, proton, α-particle plasma is found to be $(m_{\mathrm{p}} (2 m_{\mathrm{MMW}} - 1) - m_{\mathrm{e}})/(m_{\mathrm{e}} + 2 m_\alpha - 3 m_{\mathrm{p}}) \approx 4\%$. Here m_α stands for the mass of the α-particle.

Part II

Model

The important thing in science is not so much to obtain new facts as to discover new ways of thinking about them.

– Sir William Lawrence Bragg

CHAPTER 5

The Flare modelled by electric circuits

A major aspect for investigation of the electron acceleration in the corona is to understand the origin of the electric fields that lead to the electron acceleration.

As explained later, the thesis at hand proposes a large scale DC electric field that establishes along a coronal magnetic loop, and therefore accelerates charged particles, in particular the electrons therein. This electric field needs to be high enough in order to explain the observed photon fluxes, which are closely correlated electron fluxes.

In order to describe the origin of the electric field needed for the acceleration mechanism simple electric circuit models are introduced in the solar atmosphere. The circuits are made up by macroscopic components, e.g., resistors, which are estimated when the local physical conditions, such as, temperature and particle density as well as their geometry obtained by observations are considered. From such a circuit's perspective a flare is initiated when a current is established that flows through the highly conductive coronal plasma (see e.g., Somov, 2000). The power supply for the circuit is powered by photospheric motion. Such motions are reported by many observations (e.g., Martres *et al.*, 1973; Santos & Büchner, 2007; Yang *et al.*, 2004).

In this thesis it is proposed that the energy released in the corona can be understood by means of electric circuits (see e.g., Akasofu, 1979; Alfvén & Carlqvist, 1967; Kan *et al.*, 1983; Obayashi, 1975; Sen & White, 1972; Ugai, 2007; Zaitsev & Stepanov, 1992; Zaitsev *et al.*, 1998). The idea is that the magnetic reconnection establishes an electric connection between the regions of different magnetic polarity of the active region through the corona, and therefore triggers the flare.

In this chapter the electric circuits are discussed, with which the flare scenario is modelled. The chapter is mainly structured in two sections: In Sect. 5.1 the basic ideas for the model discussed in the thesis are explained in detail. These general explanations are then investigated and briefly discussed using electric circuits in Sect. 5.2.

5.1 Description of the model

Active regions are groups of sunspots. They contain spots of both kinds of magnetic polarity (e.g., Fig. 5.1 shows two different active regions). In Fig. 5.1(a) arc like magnetic structures can be seen, which connect regions of different magnetic polarities. These regions are separated by the magnetic neutral line, as indicated by the dashed orange line in Fig. 5.1(a). Figure 5.1(b) presents a magnetogram in which the regions of different magnetic polarities of an active region are shown. The dotted line therein represents the magnetic neutral line. An other example for the magnetic neutral line is presented in Figs. 5.2(c) to 5.2(f).

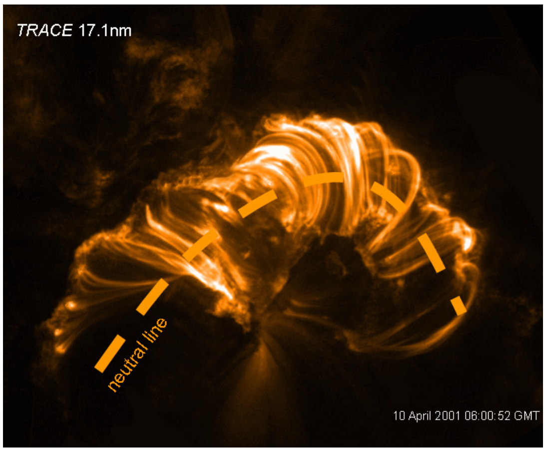

(a) Image obtained by *TRACE* spacecraft (at a wavelength of 17.1 nm on April 10, 2001 (6:00:52 GMT).

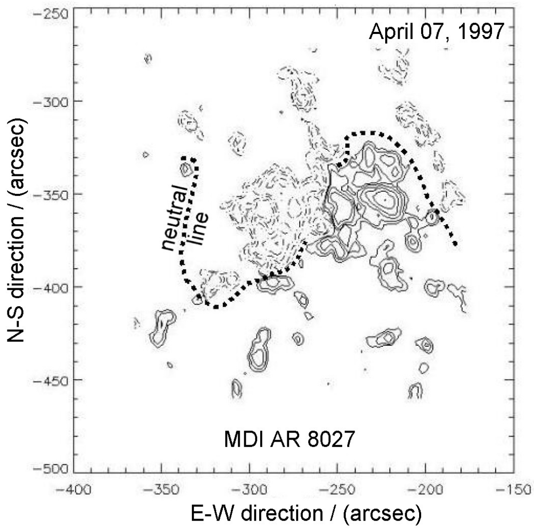

(b) The longitudinal field magnetogram of the active region NOAA AR 8027 measured by *SOHO-MDI* on April 7, 1997 (14:24 GMT). The dashed/solid contour lines represent northern/southern magnetic polarity, respectively. Reference: Aurass *et al.* (2005).

Figure 5.1: *TRACE* and *MDI* images of two different active regions. In both pictures a magnetic neutral line has been drawn.

The active regions are areas of high magnetic field concentration penetrating the photosphere: Yang *et al.* (2004) have reported magnetic flux densities in the case of NOAA AR 10486 (October 29, 2003) reaching up to $0.15\,\mathrm{T} = 1.5\,\mathrm{kG}$. They also mention photospheric flow motion with velocities up to $1.6\,{}^{\mathrm{km}}\!/\!{}_{\mathrm{s}}$ (see Fig. 5.2). Xu *et al.* (2004) report from near-infrared observations of the same event that the separation speed of the two flare ribbons is about $19\,{}^{\mathrm{km}}\!/\!{}_{\mathrm{s}}$ in regions with high magnetic fields, and increases to about $38\,{}^{\mathrm{km}}\!/\!{}_{\mathrm{s}}$ in regions, where weaker fields are found. These observations are not unusual as it can be seen, when they are compared with other events (see e.g., Kitahara & Kurokawa, 1990; Wang *et al.*, 2003, 2004).

A bipolar active region is schematically presented in Fig. 5.3. The yellow plane represents an area in the solar photosphere, where the regions of northern and southern magnetic polarity are located and which are separated from one another by the magnetic neutral line.

Since the temperature in the photosphere is roughly $6\,000\,\mathrm{K}$ the plasma is only partly ionised, whereas in the overlying corona, the temperature is sufficiently high ($> 1\,\mathrm{MK}$) to ionise most of the elements completely (see Fig. 2.5, pg. 10). Due to the present photospheric plasma motion in the partly ionised photospheric plasma, a force, i.e., the Lorentz force $q\,\vec{u}_{\mathrm{ind}} \times \vec{B}$ acts on the charges q of the plasma and leads to the generation of a current, as indicated by the magenta arrows in Fig. 5.3. The blue arrows illustrate the direction of the plasma velocity $\vec{u}_{\mathrm{ind}}$ which proposed by e.g., Heyvaerts (1974) is considered to be reversed at the blue dashed line (velocity separatrix) and the quantity $\vec{B}$ stands for the magnetic flux density. Hence the resulting Lorentz force points either toward the velocity separatrix or away from there, depending on the directions of the magnetic flux vector and the plasma velocity vector. This establishes an electric DC power supply within the active region.

Next electronics can be used to describe this quite complicated picture by a model: The electric power supplies are caused by the motion in regions of different magnetic polarities. The wires connecting them with each other correspond to the solar plasma, mainly confined by the magnetic field lines. Hence electric currents are established, which balance out the power supplies'

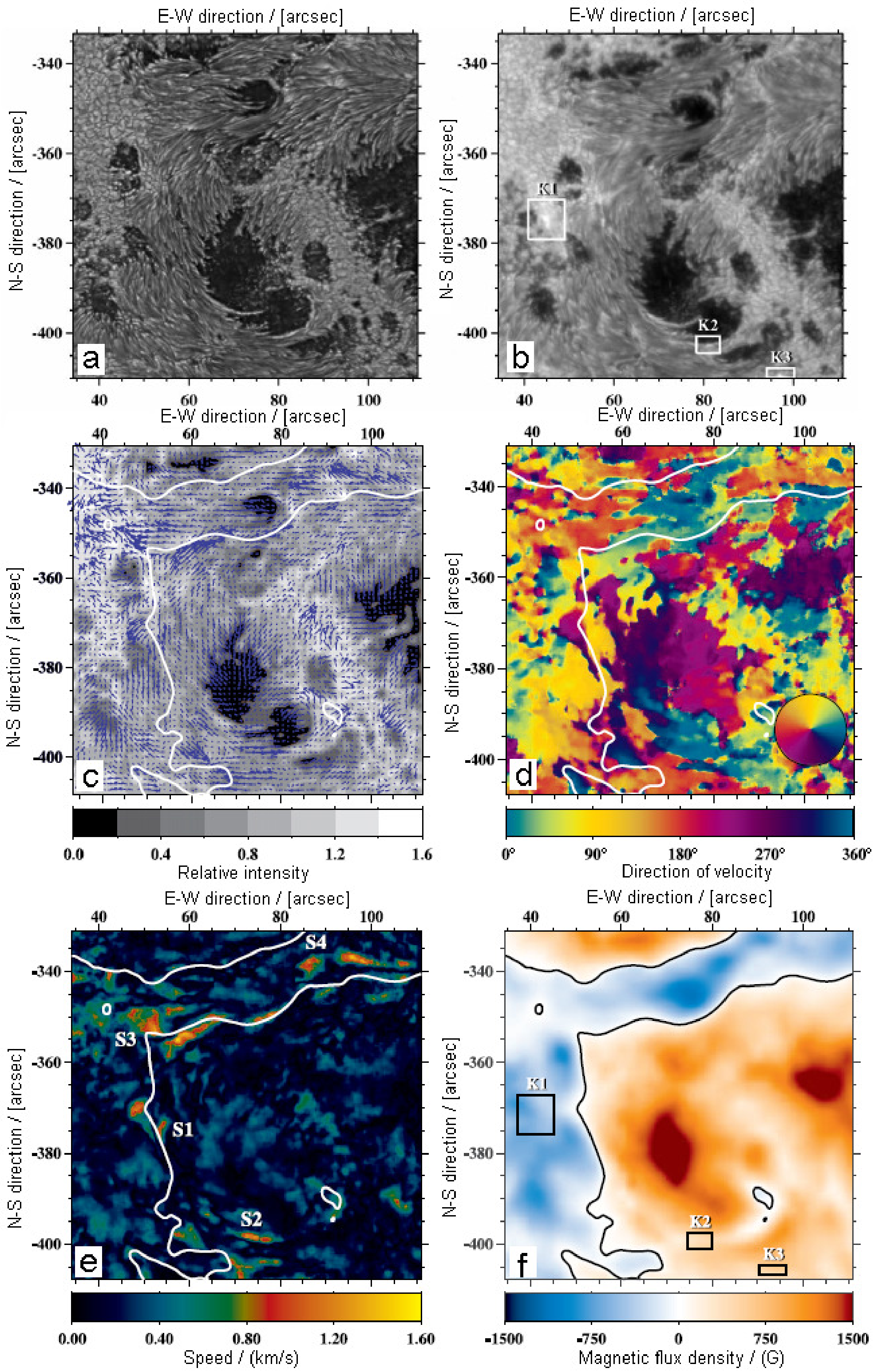

Figure 5.2: White-light continuum images (a-b), and photospheric flows and magnetic field configurations (c-f) of solar NOAA AR 10486 obtained on October 29, 2003: (a) A speckle-reconstructed image showing the preflare state at 16:59 UT and (b) a frame-selected image at 20:44 UT depicting the white-light flare kernels outlined by three white boxes, i.e., K1, K2, and K3. (c) flow vectors, (d) azimuth angle of the velocity vectors, (e) magnitude of the velocity vectors, and (f) MDI magnetogram with superposed magnetic neutral lines. Reference: Yang *et al.* (2004).

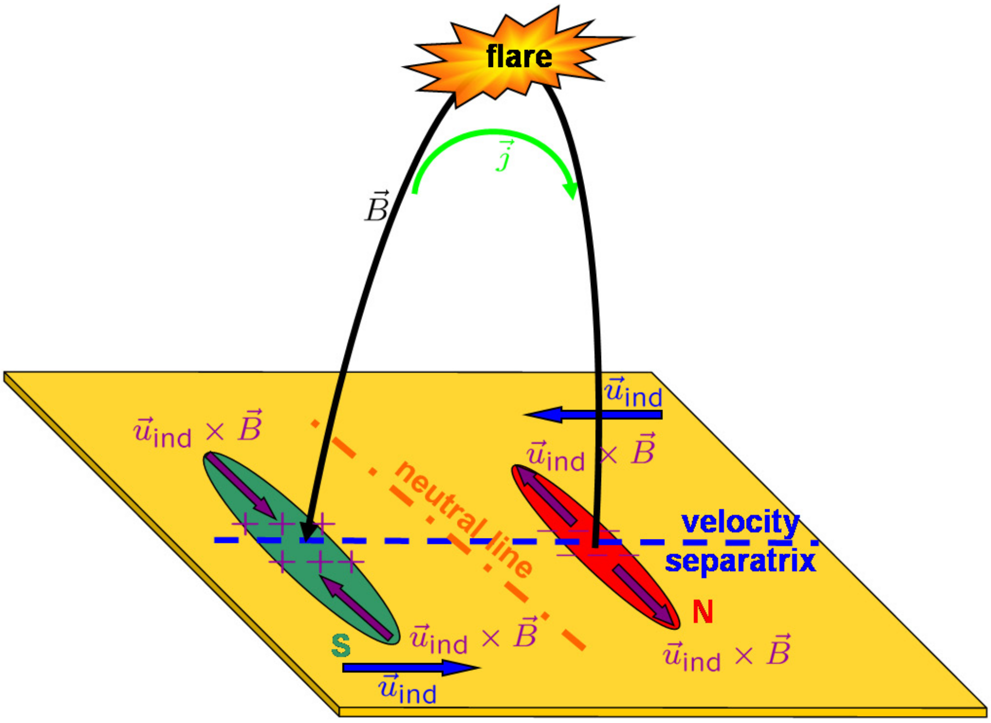

Figure 5.3: Simplified sketch of the geometrical configuration right even at the flare ignition in the solar corona. The current density $\vec{j}$ is established in the corona as a result of charge separation in the photosphere.

voltage.

It is a well known principle that electric currents always choose the path of the lowest resistance. Since the plasma resistivity is highly dependent on the temperature, the conductivity in the corona is about 1 090 times (see Appendix B) higher than in the photospheric plasma. In the plasma the charged particles propagate along the magnetic field lines, which correspond to electric wires. If there is a magnetic connection between two oppositely charged areas through the corona, possibly as a result of magnetic reconnection, an electric current (green arrow in Fig. 5.3) establishes (Alfvén & Carlqvist, 1967; Heyvaerts, 1974) through the corona. Then an electric field occurs along the coronal magnetic field line and acts on the electrons within the coronal loop and accelerates them along the field up to high energies.

5.2 Flare circuits

In order to discuss the flare energetics and to obtain the values for the electric field necessary for the electron acceleration, the model from Fig. 5.3 is translated into an electric circuit as drawn in Fig. 5.4(a). There are two electric DC power supplies u_1 and u_2 representing both different regions of magnetic polarity at the bipolar active region. Each of them has its own internal resistor, namely r_3 and r_4. The induced current can be closed via the photosphere of each region, i.e., via the resistors r_1 and r_2, and/or by an interconnection between these both regions, i.e., via the resistors $r_{\mathrm{i},1}$ and $r_{\mathrm{i},2}$. These interconnections can be established by both through the photosphere, i.e., via the resistors r_6 and r_8, and through the corona via the resistors r_5 and r_7. The latter can only happen, if there is a magnetic connection present between both different polarity regions of the active region through the corona. For simplicity the resistors r_5 and r_6, as well as r_7 and r_8 are combined to $r_{\mathrm{i},1} = {r_5 r_6}/{(r_5+r_6)}$ and $r_{\mathrm{i},2} = {r_7 r_8}/{(r_7+r_8)}$. As already mentioned, the resistors

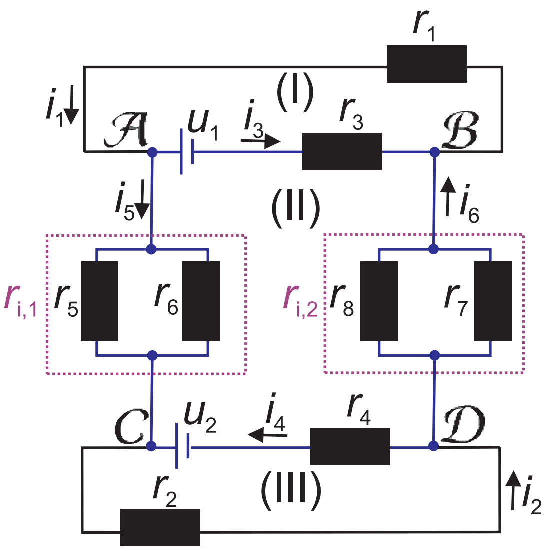

(a) Translation of Fig. 5.3 into a circuit diagram.

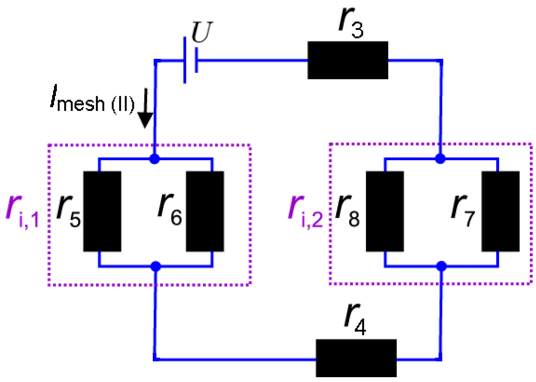

(b) The simplified electric circuit is extracted from the (II)nd bluely coloured mesh of the circuit in Fig. 5.4(a).

Figure 5.4: The simplified electric circuit for a flare is presented.

r_5 and r_7 are coronal resistors, whereas the other ones are located in the photosphere. Since the resistivity is much lower in the corona than in the photosphere (see Appendix B), the relationship $r_n \ll r_o$ for all $n \in \{5, 7\}$ and all $o \in \{1, 2, 3, 4, 6, 8\}$ is satisfied. Therefore $r_{i,1}$ and $r_{i,2}$ become either $r_{i,1} \approx r_5$ or $r_{i,1} \approx r_6$ and $r_{i,2} \approx r_7$ or $r_{i,2} \approx r_8$ depending on whether there is a magnetic connection through the corona present or not, respectively.

Applying Kirchhoff's law to the knots (i.e., $\mathcal{A}$, $\mathcal{B}$, $\mathcal{C}$, and $\mathcal{D}$) in Fig. 5.4(a)

$$i_1 = i_5 + i_3 \tag{5.1}$$
$$i_3 + i_6 = i_1 \tag{5.2}$$
$$i_4 + i_5 = i_2 \tag{5.3}$$
$$i_2 = i_4 + i_6 \tag{5.4}$$

are obtained. Accordingly for the meshes (i.e., (I), (II), and (III))

$$-u_1 = r_3 i_3 + r_1 i_1 \tag{5.5}$$
$$u_2 = r_2 i_2 + r_4 i_4 \tag{5.6}$$
$$u_1 - u_2 = r_{i,1} i_5 - r_4 i_4 + r_{i,2} i_6 - r_3 i_3 \tag{5.7}$$

can be written. The inspection of Eqs. (5.1) and (5.2) provides the important result

$$i_5 = i_6, \tag{5.8}$$

i.e., there are always two equal but counter-streaming currents connecting the circuits of both magnetic regions. Inserting Eqs. (5.1) and (5.4) into Eqs. (5.5) and (5.6) and taking Eq. (5.8) into account, the Eqs. (5.5) to (5.7) lead to an inhomogeneous system of algebraic equations, i.e.,

$$u_1 - u_2 = -r_3 i_3 - r_4 i_4 + (r_{i,1} + r_{i,2})\, i_5 \tag{5.9}$$
$$-u_1 = (r_1 + r_3)\, i_3 + r_1 i_5 \tag{5.10}$$
$$u_2 = (r_2 + r_4)\, i_4 + r_2 i_5. \tag{5.11}$$

Hence the electric current

$$i_5 = \frac{r_1(r_2 + r_4)u_1 - r_2(r_1 + r_3)u_2}{r_1 r_3\,(r_2 + r_4) + r_2 r_4\,(r_1 + r_3) + (r_{i,1} + r_{i,2})\,(r_1 + r_3)\,(r_2 + r_4)} \tag{5.12}$$

connecting both regions of the active region is obtained.

According to Eq. (5.12) a fully symmetrical circuit, i.e., $u_1 = u_2$, $r_1 = r_2$, and $r_3 = r_4$ would directly lead to $i_5 = i_6 = 0$. In such a case the electrical circuits would be closed completely through the photosphere, but no current would flow through the interconnecting resistors neither through the coronal part (r_5 and r_7) nor through the photospheric part (r_6 and r_8). However a minor asymmetry (e.g., caused by different plasma flow velocities in the photosphere $u_1 \neq u_2$ and/or different values of the resistors r_1, r_2, r_3, and r_4) would lead to the occurrence of such currents $i_5 = i_6 \neq 0$ interconnecting both parts of the bipolar active region, and the counter-streaming (see Fig. 5.4(a)) electric currents i_5 and i_6 would have the same value.

Note that the hard X-ray sources (e.g., see Fig. 3.7(a), pg. 21) accompanying a flare usually appear pairwise. As explained X-ray emissions are generated in these regions by highly energetic electrons which interact with the dense solar atmosphere. Therefore it seems reasonable to assume that electrons building up the two coronal currents i_5 and i_6 are the source for the hard X-ray footpoint double sources. Since each electric current is accompanied by a magnetic field, the counter-streaming currents could compensate the magnetic field in-between them. Therefore these currents need to be cospatial.

5.2.1 Simplified flare circuit

Since electric currents always choose the path of the lowest resistance, which is through the corona in the considered case, the complete electric circuit can be simplified to a single mesh as drawn in Fig. 5.4(b). In that circuit a DC power supply U is the resulting electric potential, if the two power supplies from Fig. 5.4(a) are merged, i.e., $U = u_1 - u_2$. It is serially connected with four macroscopic resistors, i.e., the power supplies' inner resistors (i.e., r_3 and r_4), and the interconnecting resistors $r_{\mathrm{i},1}$, and $r_{\mathrm{i},2}$. As before the interconnecting resistors are made up by a photospheric (i.e., r_6 and r_8) and by a coronal (i.e., r_5 and r_7) contribution, i.e., $r_{\mathrm{i},1} = {}^{r_5 r_6}/_{(r_5+r_6)}$ and $r_{\mathrm{i},2} = {}^{r_7 r_8}/_{(r_7+r_8)}$. The values for the resistors are chosen to be $r_3 = r_4 = R_{\mathrm{in}}$, $r_6 = r_8 = R_{\mathrm{ph}}$, and $r_5 = r_7 = R_{\mathrm{co}}$. How these resistors are determined is explained next.

A macroscopic resistor R is defined by

$$R = \frac{\eta L}{A}, \tag{5.13}$$

with its cross sectional area A, length L, and electric resistivity η. The first two parameters (i.e., A and L) are questions of geometry, whereas the electric resistivity is a plasma parameter depending strongly on the plasma temperature T and weakly on the electron density N_{e} (see Appendix B and/or Fig. B.1).

To choose realistic parameters for determining the resistors, the example shown in Fig. 3.7(a) is employed. Though these parameters derived from observations of the event from October 28, 2003, they are typical for many flare scenarios: The hard X-ray source's diameter $\oslash_{\mathrm{s}}$ is assumed to be about $\oslash_{\mathrm{s}} \approx 10\,\mathrm{Mm}$. The depth d_{s} of the photosphere is considered to be $d_{\mathrm{s}} \approx 500\,\mathrm{km}$ (see e.g., Priest, 2000). Thus the cross section $A_{\mathrm{ph}} = d_{\mathrm{s}} \oslash_{\mathrm{s}} = 5 \times 10^{12}\,\mathrm{m}^2$ is obtained. $L_{\mathrm{ph}} = 40\,\mathrm{Mm}$ is chosen as length of the inner photospheric resistor. The distance between the two hard X-ray sources is about $L_{\mathrm{s}} = 70\,\mathrm{Mm}$ (see Fig. 3.7(a)). Assuming that the overlying magnetic loop is a semicircle, its length L_{co} can be calculated by $L_{\mathrm{co}} = {}^{(\pi L_{\mathrm{s}})}/_2 \approx 110 \times 10^6\,\mathrm{m}$. The cross sectional area of the loop is estimated by A_{s} which according to Sect. 3.2.1 can be obtained by *RHESSI* observations, i.e., $A_{\mathrm{s}} \approx 80 \times 10^{12}\,\mathrm{m}^2 = A_{\mathrm{co}}$. These values and the geometrical configuration are sketched in Fig. 5.5.

In the Appendix B (see e.g., Fig B.1) the electric resistivity in the photosphere and corona for these given parameters are found to be $\eta_{\mathrm{ph}} = 9.12 \times 10^{-3}\,\Omega\mathrm{m}$ and $\eta_{\mathrm{co}} = 8.37 \times 10^{-6}\,\Omega\mathrm{m}$, respectively. With these values the resistors

$$R_{\mathrm{in}} = \frac{\eta_{\mathrm{ph}} L_{\mathrm{ph}}}{A_{\mathrm{ph}}} = 7.30 \times 10^{-8}\,\Omega \tag{5.14}$$

$$R_{\mathrm{ph}} = \frac{\eta_{\mathrm{ph}} L_{\mathrm{s}}}{A_{\mathrm{ph}}} = 1.28 \times 10^{-7}\,\Omega \tag{5.15}$$

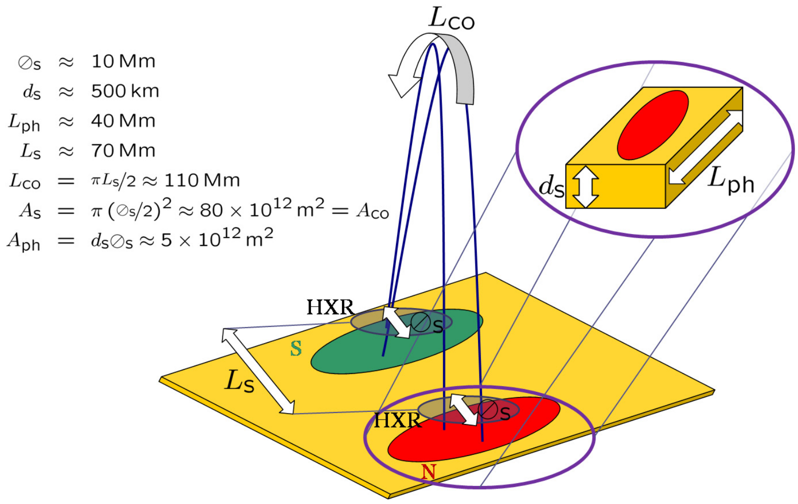

Figure 5.5: The sketch presents the important geometrical parameters for the electric components of the electric circuits.

$$R_{co} = \frac{\eta_{co} L_{co}}{A_{co}} = 1.14 \times 10^{-11}\,\Omega \tag{5.16}$$

are determined. The quantities R_{in}, R_{ph} and R_{co} represent the inner, the photospheric and the coronal resistor, respectively.

If these values for the resistors are considered, it can be seen that, the photospheric contributions of the interconnecting resistors $r_{i,1}$ and $r_{i,2}$ from Fig. 5.4(b) can be neglected, and the interconnecting resistors become $r_{i,1} = r_{i,2} = {}^{(R_{co}R_{ph})}/_{(R_{co}+R_{ph})} \approx R_{co}$. Kirchhoff's law provides

$$I_{\mathrm{mesh\,(II)}} = \frac{U}{2\,(R_{in} + R_{co})} \approx \frac{U}{2R_{in}} = u_{ind} B \frac{A_{ph}}{\eta_{ph}} \tag{5.17}$$

for the current (see Fig. 5.4(b)), which is determined by the power supply's voltage U. As explained in Sect. 5.1 the power of the power supply is generated according to Faraday's induction law, i.e.,

$$U = u_{ind} B L_s. \tag{5.18}$$

As introduced in Fig. 5.3, u_{ind} denotes the speed of the photospheric plasma flow. Note that the current from Eq. (5.17) is independent of the length of the photospheric resistor.

If it is assumed that the flare power released in the corona $P_e = 10^{22}\,\mathrm{W}$ (see Sect. 3.2.1) is equal to the electric power in the coronal resistors of the circuit in Fig. 5.4(b), then

$$I_{\mathrm{mesh\,(II)}} = \sqrt{\frac{P_e}{2R_{co}}} \approx 2.08 \times 10^{16}\,\mathrm{A} \tag{5.19}$$

can be obtained by using $U_{co} = R_{co} I_{\mathrm{mesh\,(II)}}$, where U_{co} represents the voltage drop in one of the coronal resistors. The circumstance that there are two resistors in the corona leads to the 2 in the denominator of the middle-term of Eq. (5.19) and in the following denominator of the electric current estimation. Note that the current is in good agreement with the electric current of about ${}^{(F_e e)}/_2 \approx 8 \times 10^{16}\,\mathrm{A}$, which is generated by the observed energetic ($\geq 20\,\mathrm{keV}$) electron flux of about $F_e \approx 10^{36}\,{}^{\mathrm{electrons}}/_{\mathrm{s}}$ (see Sect. 3.2.1). The quantity e stands for the elementary charge.

By using Eqs. (5.15), (5.17), (5.18), and (5.19) the constraint

$$u_{ind} B = \frac{I_{\mathrm{mesh\,(II)}}}{{}^{A_{ph}}/_{(2\eta_{ph})}} \approx 76.1\,{}^{\mathrm{V}}/_{\mathrm{m}} \tag{5.20}$$

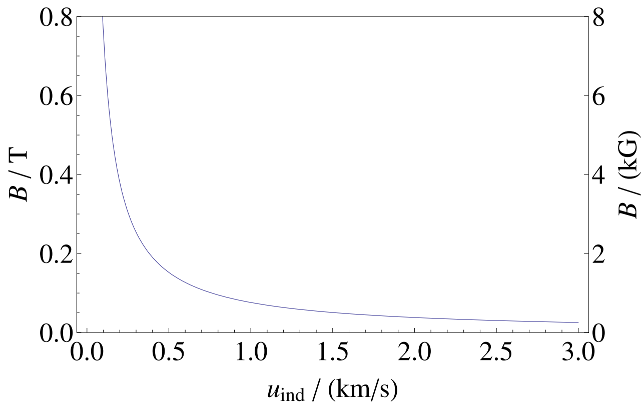

Figure 5.6: The diagram shows the curve which fulfils Eq. (5.20).

for the product $u_{\mathrm{ind}}B$ can be found. This requirement given by Eq. (5.20) can be fulfilled, e.g., for $u_{\mathrm{ind}} \approx 870\,{}^{\mathrm{m}}\!/\!{}_{\mathrm{s}}$ and $B \approx 0.087\,\mathrm{T} = 870\,\mathrm{G}$, which are reasonable conditions for the photosphere (see e.g. Yang *et al.*, 2004). Other possibilities are presented by the curve in Fig. 5.6.

The electric field along the coronal loop is estimated by the electrostatic voltage drop at the coronal resistor, i.e.,

$$E_0 = -\frac{U_{\mathrm{co}}}{L_{\mathrm{co}}} \approx -2.18 \times 10^{-3}\,{}^{\mathrm{V}}\!/\!{}_{\mathrm{m}}. \tag{5.21}$$

The negative sign is introduced due to the following convention: An electron located at x_a, where it only experiences the electric field E, shall be accelerated towards $x_b > x_a$.

The voltage drop at one of the coronal resistors is $U_{\mathrm{co}} = 240\,\mathrm{kV}$, and Eq. (5.18) gives for the power supplies voltage

$$U = 3\,\mathrm{GV}. \tag{5.22}$$

Note that this simplified circuit (Fig. 5.4(b)) allows to understand easily, how the coronal current is related to the power supply: Consider the circuit as it is shown in Fig. 5.4(b) being shorted, i.e., $R_{\mathrm{co}} \ll R_{\mathrm{ph}}$. In such a case, the shorted current is limited by the power supply's internal resistor R_{in}. The interconnecting resistors are constituted by a coronal (i.e., r_5, r_7) and a photospheric (i.e., r_6, r_8) contribution. Therefore the exact electric current in this mesh is given in accordance with Ohm's law by

$$I_{\mathrm{mesh\,(II)}} = \frac{U}{\frac{r_5 r_6}{r_5+r_6} + 2R_{\mathrm{in}} + \frac{r_7 r_8}{r_7+r_8}}. \tag{5.23}$$

or with $U = 3\,\mathrm{GV}$ and with the resistors as introduced above

$$\begin{aligned} I_{\mathrm{mesh\,(II)}} &= \frac{(R_{\mathrm{co}} + R_{\mathrm{ph}})\,U}{2\,(R_{\mathrm{in}}R_{\mathrm{ph}} + R_{\mathrm{co}}\,(R_{\mathrm{in}} + R_{\mathrm{ph}}))} \\ &\approx 2.08 \times 10^{16}\,\mathrm{A}. \end{aligned} \tag{5.24}$$

In order to analyse the dependence of the electric current on the coronal resistor, the following two cases are briefly discussed:

1. Case: If there is no magnetic connection through the corona, the coronal resistor can be considered as infinite, leading to a vanishing coronal current. In this case the total current $I_{\mathrm{mesh\,(II)}}$ is found to be,

$$\begin{aligned} I_{R_{\mathrm{co}}\to\infty} &= \lim_{R_{\mathrm{co}}\to\infty}\left[I_{\mathrm{mesh\,(II)}}\right] = \frac{U}{2\,(R_{\mathrm{in}} + R_{\mathrm{ph}})} \\ &\approx 0.76 \times 10^{16}\,\mathrm{A}. \end{aligned} \tag{5.25}$$

2. Case: In the opposite case, if e.g., by means of a magnetic reconnection a magnetic connection through the corona is established, the circuit is closed through the corona. Hence the coronal resistor can be considered to be very small, leading to

$$I_{R_{\mathrm{co}}\ll R_{\mathrm{in}}} \approx \lim_{R_{\mathrm{co}}\to 0}\left[I_{\mathrm{mesh\,(II)}}\right] = \frac{U}{2R_{\mathrm{in}}} \approx 2.08\times 10^{16}\,\mathrm{A}. \tag{5.26}$$

In result, the change from a perfectly isolating (first case) to a perfectly conducting (second case) corona, leads to a jump of the electric current by the factor of

$$\frac{I_{R_{\mathrm{co}}\ll R_{\mathrm{in}}}}{I_{R_{\mathrm{co}}\to\infty}} = \frac{(R_{\mathrm{in}}+R_{\mathrm{ph}})}{R_{\mathrm{in}}} \approx 2.75. \tag{5.27}$$

That evidently shows that a shorted current through the corona would be limited by the huge photospheric resistor R_{in}, and would be related only with a 2.75 times stronger current. This kind of jump happens suddenly when a magnetic connection through the corona is established along which the electric current can go. Indeed this is a discontinuous jump, which becomes continuous when a capacitive electric component is added to the circuit (see Sect. 5.2.2).

Comparing the voltages at the resistor $r_{\mathrm{i},1}$ (see Fig. 5.4(b)) in the case of the established magnetic connection through the corona with the case where no such a connection[1] is present

$$\frac{U_{\mathrm{i,co}}}{U_{\mathrm{ph}}} = \frac{R_{\mathrm{co}}}{R_{\mathrm{co}}+R_{\mathrm{ph}}} \approx 9\times 10^{-5} \tag{5.28}$$

is obtained and the two quantities $U_{\mathrm{i,co}} = \left({(R_{\mathrm{co}}R_{\mathrm{ph}})}/{(R_{\mathrm{co}}+R_{\mathrm{ph}})}\right) I_{\mathrm{mesh\,(II)}} \approx 240\,\mathrm{kV}$ and $U_{\mathrm{ph}} = R_{\mathrm{ph}} I_{\mathrm{mesh\,(II)}} \approx 2.66\,\mathrm{GV}$ are found. In result the voltage of the resistor $r_{\mathrm{i},1}$ and analogously for the resistor $r_{\mathrm{i},2}$ is dramatically diminished due to the shorted circuit through the corona. It shall be underlined that this diminished voltage, which is actually the voltage along the coronal loop, is nevertheless high enough (i.e., 240 kV) to accelerate electrons up to high energies, as it is discussed in detail in Sect. 6.1 later.

Furthermore, the continuous photospheric plasma motion along the way $\mathrm{d}X = u_{\mathrm{ind}}\mathrm{d}t$ in the time interval $\mathrm{d}t$ builds up an energy of

$$\mathrm{d}W_{\mathrm{s}} = (N_{\mathrm{e,ph}}A_{\mathrm{ph}}L_{\mathrm{ph}})\cdot(e u_{\mathrm{ind}}\,B)\cdot \mathrm{d}X, \tag{5.29}$$

due to the action of the Lorentz force $eu_{\mathrm{ind}}\,B$. Here $N_{\mathrm{e,ph}}$ stands for the total electron number density in the photosphere, whereas $N_{\mathrm{e,ph}}A_{\mathrm{ph}}L_{\mathrm{ph}}$ represents the total number of electrons in the volume $A_{\mathrm{ph}}L_{\mathrm{ph}}$. Therefore the power of the photospheric motion

$$\begin{aligned} P_{\mathrm{ph}} = \frac{\mathrm{d}W_{\mathrm{s}}}{\mathrm{d}t} &= (N_{\mathrm{e,ph}}A_{\mathrm{ph}}L_{\mathrm{ph}})\cdot(e u_{\mathrm{ind}}\,B)\cdot u_{\mathrm{ind}} \\ &= eN_{\mathrm{e,ph}}A_{\mathrm{ph}}L_{\mathrm{ph}}\,B\,u_{\mathrm{ind}}^2 \approx 8.4\times 10^{25}\,\mathrm{W} \end{aligned} \tag{5.30}$$

(when $L_{\mathrm{ph}} = 4\times 10^7\,\mathrm{m}$, $u_{\mathrm{ind}} = {\mathrm{d}X}/{\mathrm{d}t} = 870\,{\mathrm{m}}/{\mathrm{s}}$, and $B = 0.087\,\mathrm{T}$, and $N_{\mathrm{e,ph}} = 4\times 10^{19}\,\mathrm{m}^{-3}$ are used) is much higher than the required and in the corona released flare power ($10^{22}\,\mathrm{W}$). This means that the photospheric motion possesses more than enough power to permanently drive the electric circuit. It shall be emphasised that according to these estimations, the continuously generated power in the photosphere can be considered as the source for the energy of the flare. In other words, the energy release in the solar corona can be driven by photospheric motion.

5.2.2 Extended flare circuit

In real electric circuits besides the resistive components also inductive and capacitive components are found. By introducing these components into the flare circuit shown in Fig. 5.4(a), time-scales are established.

[1] Hence there is only a connection along the photospheric resistor R_{ph} present.

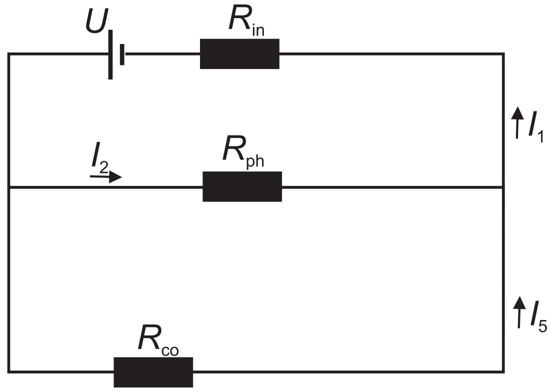

(a) The circuit from Fig. 5.4(a) is further simplified, i.e., just half of the circuit containing the power supply, the internal resistor, and one of the interconnecting resistors are considered.

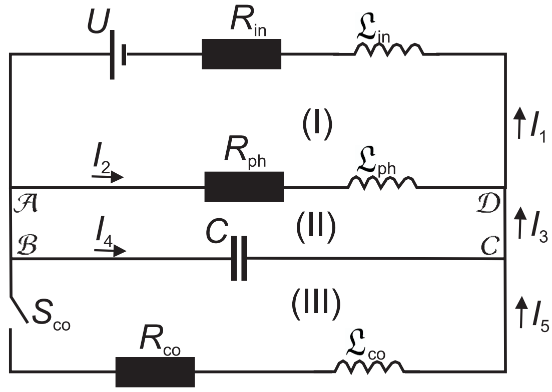

(b) The circuit from Fig. 5.7(a) is supplemented with a capacitor and three inductivities. This step introduces time-scales for the flare into the model.

Figure 5.7: Electric circuit model for a flare

This extended circuit is subsequently discussed for a simplified version. Hence the simplification in form of an approximation for the circuit presented in Fig. 5.4(a) is chosen, i.e., only half of the circuit system from Fig. 5.4(a) is taken into account, since it already contains all relevant parts. This approximation is justifiable, since the error related to such a simplification is in the order of a factor of two. In the calculations following, the power supply's voltage is reduced by the same factor of two in order to compensate the error related with this simplification. The simplified circuit diagram is presented in Fig. 5.7(a). As it can be seen therein, the power supply U is connected serially with the internal resistor R_{in}. Remember that this resistor represents the "wire" for the current closed in the photospheric part of the active region. Both of these components (U and R_{in}) are connected parallelly with the interconnecting resistor, which consists of two parallelly connected resistors, one for the photosphere R_{ph} and one for the corona R_{co}.

This circuit is discussed briefly next: Using the laws of Kirchhoff, i.e., $U = R_{\text{in}} I_1 + R_{\text{ph}} I_2$, $0 = R_{\text{co}} I_5 - R_{\text{ph}} I_2$, and $I_1 = I_2 + I_5$, the three currents

$$I_1 = \frac{(R_{\text{co}} + R_{\text{ph}})\, U}{R_{\text{in}} R_{\text{ph}} + R_{\text{co}}\,(R_{\text{in}} + R_{\text{ph}})} = 1.37 \times 10^{7}\,\mathrm{A/V}\, U \tag{5.31}$$

$$I_2 = \frac{R_{\text{co}} U}{R_{\text{in}} R_{\text{ph}} + R_{\text{co}}\,(R_{\text{in}} + R_{\text{ph}})} = 1.22 \times 10^{3}\,\mathrm{A/V}\, U \tag{5.32}$$

$$I_5 = \frac{R_{\text{ph}} U}{R_{\text{in}} R_{\text{ph}} + R_{\text{co}}\,(R_{\text{in}} + R_{\text{ph}})} = 1.37 \times 10^{7}\,\mathrm{A/V}\, U \tag{5.33}$$

are obtained, as a function of the power supply U. In order to correct the error caused by the previously explained simplification, namely by considering only half of the electric circuit, the power supply U from Eq. (5.22) (pg. 38) needs to be reduced by a factor of two, too: $U = 1.5 \times 10^{9}\,\mathrm{V}$ (i.e., $u_2 \to 0$). Hence the electric currents can be found to be $I_1 = 2.05 \times 10^{16}\,\mathrm{A}$, $I_2 = 1.83 \times 10^{12}\,\mathrm{A}$, and $I_5 = 2.05 \times 10^{16}\,\mathrm{A}$. When the coronal current I_5 is compared with $I_{\text{mesh (II)}}$ from Eq. (5.24), it can be seen that the chosen approximation agrees well.

Next the inductive components are introduced: Therefore each resistor is substituted by units of a serially connected resistor and the related inductivity. In order to model the voltages in the active region a capacitor is introduced parallelly to the unit of the serially connected coronal resistor and inductivity. The resulting circuit is presented in Fig. 5.7(b). The circuit is made up by three meshes (I, II, and III), i.e., mesh I represents the photospheric circuit. Hence it contains the electric power supply U, the inner R_{in} and photospheric R_{ph} resistor, as well as the inner $\mathfrak{L}_{\text{in}}$ and photospheric $\mathfrak{L}_{\text{ph}}$ inductivity. Accordingly mesh III corresponds to the coronal circuit, which contains the coronal resistor R_{co} and the coronal inductivity $\mathfrak{L}_{\mathrm{co}}$. The introduced capacitor has the capacity C. The voltage drop in the coronal branch of the circuit (i.e., between the knots $\mathcal{A}$-$\mathcal{D}$ or equivalently between $\mathcal{B}$-$\mathcal{C}$ in Fig. 5.7(b)) is represented by the voltage of the capacitor.

Meshes I and III are connected with one another through mesh II. The coronal switch S_{co} shall explain, what happens if magnetic connection between the regions of different magnetic polarity (Fig. 5.3) is established through the corona (switch is closed), or if no connection is present (switch is open).

In Sect. 5.2.1, when the resistors were introduced, all relevant quantities were explained. These are now used to determine the values for the capacitor and the inductivities according to the local plasma conditions and the geometrical considerations which need to be taken into account.

The capacity of the coronal loop is estimated with

$$C = \varepsilon_0 \frac{A_{\mathrm{co}}}{L_{\mathrm{co}}} = 6.32 \times 10^{-6}\,\mathrm{As/V}. \tag{5.34}$$

The quantity ε_0 represents the permittivity of free space.

The inductive components of the electric circuit are given by

$$\mathfrak{L} = \frac{\mu_0 L}{2\pi}\left(\ln\left|\frac{4L}{2\sqrt{A/\pi}}\right| - \frac{3}{4}\right), \tag{5.35}$$

where μ_0 stands for the permeability of free space (see e.g., Mende & Simon, 1971, pg. 232). As before L and A stand for the macroscopic length of the conductor and its cross section, respectively. Hence for the inner, the photospheric and the coronal circuit the inductivities

$$\mathfrak{L}_{\mathrm{in}} = \frac{\mu_0 L_{\mathrm{ph}}}{2\pi}\left(\ln\left|\frac{4L_{\mathrm{ph}}}{2\sqrt{A_{\mathrm{ph}}/\pi}}\right| - \frac{3}{4}\right) = 27.2\,\mathrm{Vs/A} \tag{5.36}$$

$$\mathfrak{L}_{\mathrm{ph}} = \frac{\mu_0 L_{\mathrm{s}}}{2\pi}\left(\ln\left|\frac{4L_{\mathrm{s}}}{2\sqrt{A_{\mathrm{ph}}/\pi}}\right| - \frac{3}{4}\right) = 55.4\,\mathrm{Vs/A} \tag{5.37}$$

$$\mathfrak{L}_{\mathrm{co}} = \frac{\mu_0 L_{\mathrm{co}}}{2\pi}\left(\ln\left|\frac{4L_{\mathrm{co}}}{2\sqrt{A_{\mathrm{co}}/\pi}}\right| - \frac{3}{4}\right) = 66.7\,\mathrm{Vs/A} \tag{5.38}$$

can be determined, respectively.

Kirchhoff's laws for this circuit

From the laws of Kirchhoff the following two linearly independent equations for the four knots ($\mathcal{A}$, $\mathcal{B}$, $\mathcal{C}$, and $\mathcal{D}$)

$$I_1 = I_2 + I_3 \tag{5.39}$$

$$I_3 = I_4 + I_5 \tag{5.40}$$

and the three equations for the meshes (I, II, and III)

$$U = R_{\mathrm{ph}} I_2 + \mathfrak{L}_{\mathrm{ph}} \frac{\mathrm{d}I_2}{\mathrm{d}t} + \mathfrak{L}_{\mathrm{in}} \frac{\mathrm{d}I_1}{\mathrm{d}t} + R_{\mathrm{in}} I_1 \tag{5.41}$$

$$0 = U_{\mathrm{cap}} - \mathfrak{L}_{\mathrm{ph}} \frac{\mathrm{d}I_2}{\mathrm{d}t} - R_{\mathrm{ph}} I_2 \tag{5.42}$$

$$0 = R_{\mathrm{co}} I_5 + \mathfrak{L}_{\mathrm{co}} \frac{\mathrm{d}I_5}{\mathrm{d}t} - U_{\mathrm{cap}} \tag{5.43}$$

are obtained. The Eqs. (5.39) and (5.40) can be used to eliminate I_3, i.e.,

$$I_1 = I_2 + I_4 + I_5. \tag{5.44}$$

The voltage at the capacitor is given by

$$U_{\mathrm{cap}} \;=\; \frac{1}{C}\int_0^t \mathrm{d}\hat{t}\,\left[I_4[\hat{t}]\right] + U_{\mathrm{cap},0}, \tag{5.45}$$

where $U_{\mathrm{cap}}[t=0] = U_{\mathrm{cap},0}$ represents the capacitor's voltage at the time $t = 0$.

The set of all these equations describe the whole electric circuit hence they determine the electric currents I_1, I_2, I_3, I_4, and I_5, if the switch S_{co} is closed. In such a case the three regular differential equations of first order from the meshes are coupled through the algebraic equations from the knots with each other.

In the following it is explained how the electric circuit can be solved step by step.

Step 1: Considering the photospheric circuit / Charging the capacitor

At the beginning there is no magnetic connection through the corona between the regions of different magnetic polarity. From the circuit's point of view this situation corresponds to an open coronal switch S_{co}, i.e., $I_5 = 0$, $I_1 = I_2 + I_4$, and thus Eq. (5.43) becomes obsolete. At the very beginning, i.e., at the time $t = 0$, the capacitor is considered to be completely discharged, i.e., $U_{\mathrm{cap},0} = 0$. Due to photospheric plasma motion the power supply U is established, which subsequently charges the capacitor. The process of charging is explained in the following.

The Eq. (5.41) and (5.42) for the meshes can be written as

$$U \;=\; (R_{\mathrm{ph}} + R_{\mathrm{in}})\, I_2 + (\mathfrak{L}_{\mathrm{ph}} + \mathfrak{L}_{\mathrm{in}})\,\frac{\mathrm{d}I_2}{\mathrm{d}t} + \mathfrak{L}_{\mathrm{in}}\frac{\mathrm{d}I_4}{\mathrm{d}t} + R_{\mathrm{in}} I_4 \tag{5.46}$$

$$0 \;=\; \frac{1}{C}\int_0^t \mathrm{d}\hat{t}\,\left[I_4[\hat{t}]\right] - \mathfrak{L}_{\mathrm{ph}}\frac{\mathrm{d}I_2}{\mathrm{d}t} - R_{\mathrm{ph}} I_2. \tag{5.47}$$

If

$$I_2 \;=\; i_{2,1}\exp\left[-\lambda t\right] + i_{2,2} \tag{5.48}$$

$$I_4 \;=\; i_{4,1}\exp\left[-\lambda t\right] + i_{4,2} \tag{5.49}$$

with the unknown constants $i_{2,1}$, $i_{2,2}$, $i_{4,1}$, and $i_{4,2}$ are introduced, the Eqs. (5.46) and (5.47) lead to the relations

$$0 \;=\; \left((R_{\mathrm{ph}} + R_{\mathrm{in}}) - \lambda\,(\mathfrak{L}_{\mathrm{ph}} + \mathfrak{L}_{\mathrm{in}})\right) i_{2,1} + (R_{\mathrm{in}} - \lambda\mathfrak{L}_{\mathrm{in}})\, i_{4,1} \tag{5.50}$$

$$U \;=\; (R_{\mathrm{ph}} + R_{\mathrm{in}})\, i_{2,2} + R_{\mathrm{in}} i_{4,2} \tag{5.51}$$

$$0 \;=\; -\frac{i_{4,1}}{\lambda C} + (\lambda\mathfrak{L}_{\mathrm{ph}} - R_{\mathrm{ph}})\, i_{2,1} \tag{5.52}$$

$$0 \;=\; i_{4,2} \tag{5.53}$$

$$0 \;=\; \frac{i_{4,1}}{\lambda C} - R_{\mathrm{ph}} i_{2,2}. \tag{5.54}$$

The constant λ is related with the time τ via $\lambda = {}^{1}\!/_{\tau}$. On the other hand the constant $i_{2,2}$ can be calculated from Eq. (5.51) and Eq. (5.53), $i_{4,1}$ follows from the Eq. (5.54) and Eq. (5.55), and $i_{2,1}$ is obtained from Eq. (5.56) and Eq. (5.52), i.e.,

$$i_{2,2} \;=\; \frac{U}{(R_{\mathrm{ph}} + R_{\mathrm{in}})} \tag{5.55}$$

$$i_{4,1} \;=\; U\frac{\lambda C R_{\mathrm{ph}}}{(R_{\mathrm{ph}} + R_{\mathrm{in}})} \tag{5.56}$$

$$i_{2,1} \;=\; U\frac{R_{\mathrm{ph}}}{(R_{\mathrm{ph}} + R_{\mathrm{in}})}\frac{1}{(\lambda\mathfrak{L}_{\mathrm{ph}} - R_{\mathrm{ph}})}. \tag{5.57}$$

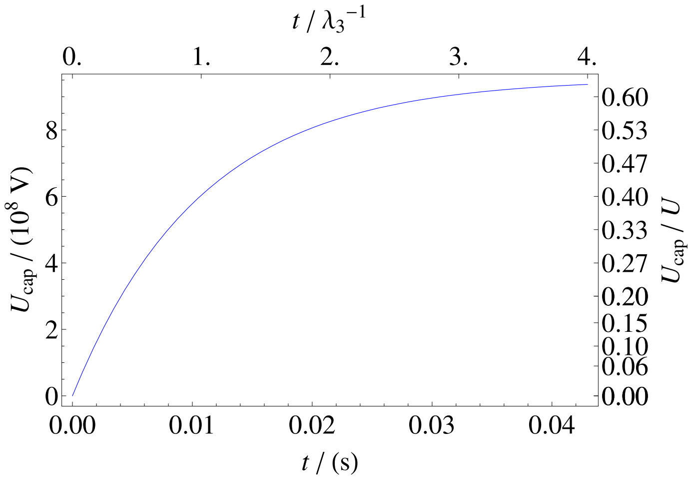

(a) Plot of U_{cap} versus the time.

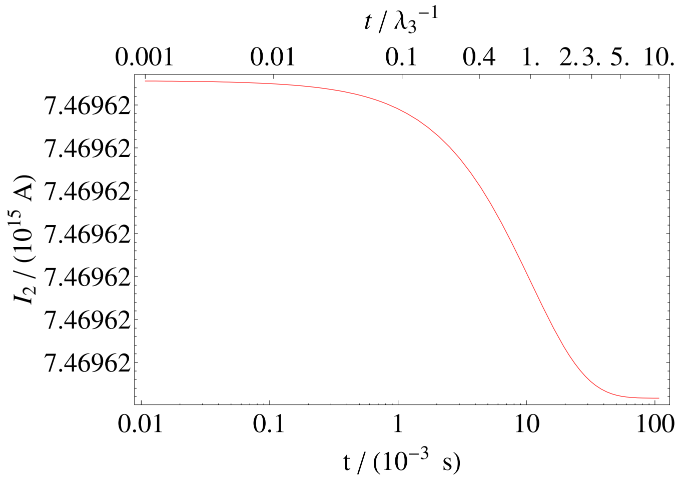

(b) Plot of I_2 versus the time. Note that the current I_2 does not decrease significantly, i.e., $I_2[t = 10^{-3}\lambda_3^{-1}] - I_2[t = 10\lambda_3^{-1}] = 1.85 \times 10^5$ A.

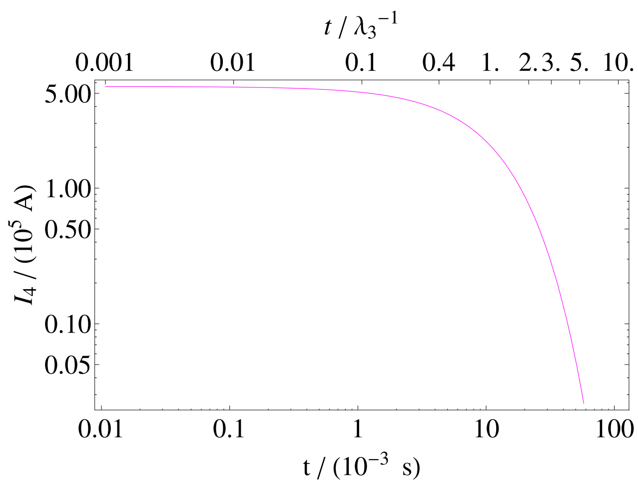

(c) Plot of I_4 versus the time.

Figure 5.8: These three diagrams present, how the initially completely discharged capacitor in Fig. 5.7(b) is charged, when the switch S_{co} is open. All diagrams consider $U = 1.5 \times 10^9$ V.

Finally by combining Eq. (5.50) with Eq. (5.52) the third order inhomogeneous polynomial characteristic equation

$$\begin{aligned} 0 &= \lambda^3 - \lambda^2 \left(\frac{R_{\mathrm{ph}}}{\mathfrak{L}_{\mathrm{ph}}} + \frac{R_{\mathrm{in}}}{\mathfrak{L}_{\mathrm{in}}} \right) + \lambda \left(\frac{1}{C\mathfrak{L}_{\mathrm{in}}} + \frac{1}{C\mathfrak{L}_{\mathrm{ph}}} + \frac{R_{\mathrm{in}}}{\mathfrak{L}_{\mathrm{in}}} \frac{R_{\mathrm{ph}}}{\mathfrak{L}_{\mathrm{ph}}} \right) \\ & -\frac{1}{C\mathfrak{L}_{\mathrm{in}}} \frac{R_{\mathrm{ph}}}{\mathfrak{L}_{\mathrm{ph}}} - \frac{1}{C\mathfrak{L}_{\mathrm{ph}}} \frac{R_{\mathrm{in}}}{\mathfrak{L}_{\mathrm{in}}} \end{aligned} \tag{5.58}$$

is found, i.e., the constant λ is obtained by solving Eq. (5.58).

Discussion:

As already mentioned the capacitive and inductive components of the electric circuit introduce different time-scales. These reciprocal time-scales manifest themselves in Eq. (5.58), i.e., using

$$\delta_{\mathrm{in}} = \frac{R_{\mathrm{in}}}{\mathfrak{L}_{\mathrm{in}}} = 2.68 \times 10^{-9}\, {}^{1}\!/\!{}_{\mathrm{s}}, \qquad \text{and} \qquad \delta_{\mathrm{ph}} = \frac{R_{\mathrm{ph}}}{\mathfrak{L}_{\mathrm{ph}}} = 2.31 \times 10^{-9}\, {}^{1}\!/\!{}_{\mathrm{s}}, \tag{5.59}$$

$$\lambda_{\mathrm{in}} = \frac{1}{\sqrt{C\mathfrak{L}_{\mathrm{in}}}} = 76.2\, {}^{1}\!/\!{}_{\mathrm{s}}, \qquad \text{and} \qquad \lambda_{\mathrm{ph}} = \frac{1}{\sqrt{C\mathfrak{L}_{\mathrm{ph}}}} = 53.4\, {}^{1}\!/\!{}_{\mathrm{s}}. \tag{5.60}$$

Hence the influence of the characteristic equation's coefficients (see Eq. (5.58)) can be summarised with $\delta_{\mathrm{ph}} \lesssim \delta_{\mathrm{in}} \ll \lambda_{\mathrm{ph}} < \lambda_{\mathrm{in}}$, i.e., the inductive and capacitive components of the electric circuit dominate the charging process of the capacitor. When these values are put into the characteristic equation (Eq. (5.58))

$$0 = \lambda^3 - \lambda^2 \times 4.99 \times 10^{-9}\, {}^{1}\!/\!{}_{\mathrm{s}} - \lambda \times 8.67 \times 10^{3}\, {}^{1}\!/\!{}_{\mathrm{s}^2} + 2.11 \times 10^{-5}\, {}^{1}\!/\!{}_{\mathrm{s}^3} \tag{5.61}$$

is obtained. Equation (5.61) has three real solutions, i.e.,

$$\lambda_1 = -9.31 \times 10^{1}\, {}^{1}\!/\!{}_{\mathrm{s}}, \qquad \lambda_2 = 2.43 \times 10^{-9}\, {}^{1}\!/\!{}_{\mathrm{s}}, \text{ and} \qquad \lambda_3 = 9.31 \times 10^{1}\, {}^{1}\!/\!{}_{\mathrm{s}}. \tag{5.62}$$

The time-scale obtained from λ_2 is far too long, i.e., $\tau = {}^{1}\!/\!{}_{\lambda_2} = 4.11 \times 10^{8}\,\mathrm{s} \approx 13\,\mathrm{yr}$. Hence that solution can be removed for the flare scenario. On the other hand, the negative time-scale following from λ_1 can not be justified and is also removed. Therefore λ_3 remains, which is a reasonable duration, i.e., $\tau_3 = {}^{1}\!/\!{}_{\lambda_3} = 1.07 \times 10^{-2}\,\mathrm{s}$.

Using λ_3 the currents I_2 (Eq. (5.48)) and I_4 (Eq. (5.49)) are found as a function of U, i.e.,

$$\begin{aligned} I_2 &= U \frac{R_{\mathrm{ph}}}{(R_{\mathrm{ph}} + R_{\mathrm{in}})} \frac{1}{(\lambda_3 \mathfrak{L}_{\mathrm{ph}} - R_{\mathrm{ph}})} \exp[-\lambda_3 t] + \frac{U}{(R_{\mathrm{ph}} + R_{\mathrm{in}})} \\ &\approx U \left(4.98 \times 10^{6}\, {}^{\mathrm{A}}\!/\!{}_{\mathrm{V}} + 1.23 \times 10^{-4}\, {}^{\mathrm{A}}\!/\!{}_{\mathrm{V}} \exp\left[-9.31 \times 10^{1}\, {}^{1}\!/\!{}_{\mathrm{s}}\, t \right] \right) \end{aligned} \tag{5.63}$$

$$\begin{aligned} I_4 &= U \frac{\lambda_3 C R_{\mathrm{ph}}}{(R_{\mathrm{ph}} + R_{\mathrm{in}})} \exp[-\lambda_3 t] \\ &\approx U\, 3.75 \times 10^{-4}\, {}^{\mathrm{A}}\!/\!{}_{\mathrm{V}} \exp\left[-9.31 \times 10^{1}\, {}^{1}\!/\!{}_{\mathrm{s}}\, t \right]. \end{aligned} \tag{5.64}$$

Due to $I_2 \gg I_3$ the currents $I_1 = I_2 + I_3 \approx I_2$ and due to $I_5 = 0$ the current $I_3 = I_4 + I_5 = I_4$ follow (according the Eqs. (5.39) and (5.40)) as a function of I_2 and I_4. From Eq. (5.45) the capacitor's voltage

$$U_{\mathrm{cap}} = U \frac{R_{\mathrm{ph}}}{R_{\mathrm{ph}} + R_{\mathrm{in}}} (1 - \exp[-\lambda_3 t]) \tag{5.65}$$

$$\approx U\, 6.36 \times 10^{-1} \left(1 - \exp\left[-9.31 \times 10^{1}\, {}^{1}\!/\!{}_{\mathrm{s}}\, t \right] \right) \tag{5.66}$$

is evaluated. The limits of I_2, I_4 and U_{cap} for $t \to 0$ are found to be

$$\begin{aligned} \lim_{t \to 0} [I_2] &= U \frac{R_{\mathrm{ph}}}{(R_{\mathrm{ph}} + R_{\mathrm{in}})} \frac{1}{(\lambda_3 \mathfrak{L}_{\mathrm{ph}} - R_{\mathrm{ph}})} + \frac{U}{(R_{\mathrm{ph}} + R_{\mathrm{in}})} = U\, 4.98 \times 10^{6}\, {}^{\mathrm{A}}\!/\!{}_{\mathrm{V}} \\ \lim_{t \to 0} [I_4] &= U \frac{\lambda_3 C R_{\mathrm{ph}}}{(R_{\mathrm{ph}} + R_{\mathrm{in}})} = U\, 3.75 \times 10^{-4}\, {}^{\mathrm{A}}\!/\!{}_{\mathrm{V}} \\ \lim_{t \to 0} [U_{\mathrm{cap}}] &= 0, \end{aligned}$$

whereas the limits for $t \to \infty$ are

$$\begin{aligned}
\lim_{t\to\infty}[I_2] &= \frac{U}{(R_{\mathrm{ph}}+R_{\mathrm{in}})} = U\,4.98\times10^{6}\,{}^{\mathrm{A}}\!/\!{}_{\mathrm{V}} \\
\lim_{t\to\infty}[I_4] &= 0 \\
\lim_{t\to\infty}[U_{\mathrm{cap}}] &= U\frac{R_{\mathrm{ph}}}{R_{\mathrm{ph}}+R_{\mathrm{in}}} = U\,6.36\times10^{-1}.
\end{aligned} \tag{5.67}$$

In the stationary case ($t \to \infty$) the influence of the inductive and capacitive components vanishes, and as expected the circuit becomes a pure Ohmian one. Note that the current I_2 changes only slightly during the whole charging process, i.e.,

$$\lim_{t\to0}[I_2] - \lim_{t\to\infty}[I_2] = U\frac{R_{\mathrm{ph}}}{(R_{\mathrm{ph}}+R_{\mathrm{in}})}\frac{1}{(\lambda_3\mathfrak{L}_{\mathrm{ph}}-R_{\mathrm{ph}})} = U\,1.23\times10^{-4}\,{}^{\mathrm{A}}\!/\!{}_{\mathrm{V}}. \tag{5.68}$$

In Fig. 5.8 the quantities U_{cap}, I_2, and I_4 are plotted in dependence on the time for the case that the power supply's voltage is chosen to be $U = 1.5\times10^{9}$ V. Figure 5.8(a) presents the voltage of the capacitor in the time interval of $[0, 4\tau_3]$. Initially the capacitor is fully discharged. As soon as the power supply's voltage is turned on the capacitor is charged within a few $\tau_3 \approx 1.07\times10^{-2}$ s to its full capacity, i.e., in less than 50 ms it becomes fully (i.e., 63.6% $U = 9.54\times10^{6}$ V) charged. Figure 5.8(b) and 5.8(c) present diagrams of I_2 and I_4 with double logarithmic axes for the time interval of $[10^{-3}\tau_3, 10\tau_3]$. Though I_2 does not change significantly both currents I_2 and I_4 decrease from their initial value. As discussed before I_4 is found to vanish completely, while I_2 does not.

Step 2: Switching the coronal circuit on

In this step the magnetic connection establishing through the corona between the two regions of different magnetic polarity is considered (see Fig. 5.3), i.e., the coronal switch S_{co} (see Fig. 5.7(b)) is closed. Hence in difference to step 1, mesh III becomes part of the electric circuit and thus all the Kirchhoff's laws presented before (see Eqs. (5.39) to (5.43)) need to be solved simultaneously. Subsequently the capacitor is assumed to be fully charged at $t = 0$, i.e., $U_{\mathrm{cap},0} = {}^{UR_{\mathrm{ph}}}\!/\!{}_{(R_{\mathrm{ph}}+R_{\mathrm{in}})}$ (see step 1, Eq. (5.67)).

Using Eq. (5.44) in Eq. (5.41), combining Eq. (5.42) with Eq. (5.45), and considering Eq. (5.45) in Eq. (5.43) the three equations

$$U = (R_{\mathrm{ph}}+R_{\mathrm{in}})\,I_2 + (\mathfrak{L}_{\mathrm{ph}}+\mathfrak{L}_{\mathrm{in}})\frac{\mathrm{d}I_2}{\mathrm{d}t} + \mathfrak{L}_{\mathrm{in}}\frac{\mathrm{d}I_4}{\mathrm{d}t} + R_iI_4 + \mathfrak{L}_{\mathrm{in}}\frac{\mathrm{d}I_5}{\mathrm{d}t} + R_{\mathrm{in}}I_5 \tag{5.69}$$

$$0 = \frac{1}{C}\int_0^t \mathrm{d}\hat{t}\,\left[I_4[\hat{t}]\right] + U_{\mathrm{cap},0} - \mathfrak{L}_{\mathrm{ph}}\frac{\mathrm{d}I_2}{\mathrm{d}t} - R_{\mathrm{ph}}I_2 \tag{5.70}$$

$$0 = R_{\mathrm{co}}I_5 + \mathfrak{L}_{\mathrm{co}}\frac{\mathrm{d}I_5}{\mathrm{d}t} - \frac{1}{C}\int_0^t \mathrm{d}\hat{t}\,\left[I_4[\hat{t}]\right] - U_{\mathrm{cap},0}, \tag{5.71}$$

are found, respectively. Analogously as presented for the photospheric circuit (see Eqs. (5.48) and (5.49)), the following approach for the electric currents is chosen

$$I_2 = I^*_{2,1}\exp[-\lambda t] + I^*_{2,2} \tag{5.72}$$

$$I_4 = I^*_{4,1}\exp[-\lambda t] + I^*_{4,2} \tag{5.73}$$

$$I_5 = I^*_{5,1}\exp[-\lambda t] + I^*_{5,2}. \tag{5.74}$$

By inserting these three equations into the Eqs. (5.69), (5.70), and (5.71), the relations

$$0 = ((R_{\mathrm{ph}}+R_{\mathrm{in}}) - \lambda(\mathfrak{L}_{\mathrm{ph}}+\mathfrak{L}_{\mathrm{in}}))\,I^*_{2,1} + (R_{\mathrm{in}}-\lambda\mathfrak{L}_{\mathrm{in}})\,I^*_{4,1} + (R_{\mathrm{in}}-\lambda\mathfrak{L}_{\mathrm{in}})\,I^*_{5,1} \tag{5.75}$$

$$U = (R_{\mathrm{ph}}+R_{\mathrm{in}})\,I^*_{2,2} + R_{\mathrm{in}}I^*_{4,2} + R_{\mathrm{in}}I^*_{5,2} \tag{5.76}$$

$$0 = -\frac{I^*_{4,1}}{\lambda C} + (\lambda\mathfrak{L}_{\mathrm{ph}} - R_{\mathrm{ph}})\,I^*_{2,1} \tag{5.77}$$

$$0 = I^*_{4,2} \tag{5.78}$$

$$0 = \frac{I^*_{4,1}}{\lambda C} - R_{\rm ph} I^*_{2,2} + U_{\rm cap,0} \tag{5.79}$$

$$0 = (R_{\rm co} - \lambda \mathfrak{L}_{\rm co})\, I^*_{5,1} + \frac{I^*_{4,1}}{\lambda C} \tag{5.80}$$

$$0 = R_{\rm co} I^*_{5,2} - \frac{I^*_{4,1}}{\lambda C} - U_{\rm cap,0} \tag{5.81}$$

are obtained. The still unknown constants $I^*_{2,1}$, $I^*_{2,2}$, $I^*_{4,1}$, $I^*_{5,1}$, and $I^*_{5,2}$ can be determined by combining the Eqs. (5.75) to (5.81) with each other, i.e., by using Eq. (5.77) and Eq. (5.80), and combining Eq. (5.79) with Eq. (5.81)

$$I^*_{5,1} = \frac{(R_{\rm ph} - \lambda \mathfrak{L}_{\rm ph})}{(R_{\rm co} - \lambda \mathfrak{L}_{\rm co})} I^*_{2,1} \tag{5.82}$$

$$I^*_{5,2} = \frac{R_{\rm ph}}{R_{\rm co}} I^*_{2,2} \tag{5.83}$$

are obtained, respectively. With Eqs. (5.78) and (5.83) the Eq. (5.76) can be rewritten as

$$I^*_{2,2} = \frac{U}{(R_{\rm ph} + R_{\rm in}\,(1 + {}^{R_{\rm ph}}/_{R_{\rm co}}))}. \tag{5.84}$$

Then Eq. (5.83) and (5.84), and Eq. (5.81) and Eq. (5.85) lead to

$$I^*_{5,2} = \frac{R_{\rm ph}}{R_{\rm co}} \frac{U}{(R_{\rm ph} + R_{\rm in}\,(1 + {}^{R_{\rm ph}}/_{R_{\rm co}}))} \tag{5.85}$$

$$I^*_{4,1} = \lambda C \left(\frac{R_{\rm ph} U}{(R_{\rm ph} + R_{\rm in}\,(1 + {}^{R_{\rm ph}}/_{R_{\rm co}}))} - U_{\rm cap,0} \right), \tag{5.86}$$

respectively. The constant $I^*_{2,1}$ follows when Eqs. (5.77) and (5.86) are considered, whereas $I^*_{5,1}$ follows from the Eqs. (5.80) and (5.86), i.e.,

$$I^*_{2,1} = \frac{1}{\lambda \mathfrak{L}_{\rm ph} - R_{\rm ph}} \left(\frac{R_{\rm ph} U}{(R_{\rm ph} + R_{\rm in}\,(1 + {}^{R_{\rm ph}}/_{R_{\rm co}}))} - U_{\rm cap,0} \right) \tag{5.87}$$

$$I^*_{5,1} = \frac{1}{\lambda \mathfrak{L}_{\rm co} - R_{\rm co}} \left(\frac{R_{\rm ph} U}{(R_{\rm ph} + R_{\rm in}\,(1 + {}^{R_{\rm ph}}/_{R_{\rm co}}))} - U_{\rm cap,0} \right). \tag{5.88}$$

The Eqs. (5.80) and (5.82) can be used in Eq. (5.76) in order to evaluate the inhomogeneous polynomial equation of forth order in λ

$$\begin{aligned} 0 = {} & \lambda^4 - \lambda^3 \left(\frac{R_{\rm in}}{\mathfrak{L}_{\rm in}} + \frac{R_{\rm ph}}{\mathfrak{L}_{\rm ph}} + \frac{R_{\rm co}}{\mathfrak{L}_{\rm co}} \right) \\ & + \lambda^2 \left(\frac{1}{C\mathfrak{L}_{\rm in}} + \frac{1}{C\mathfrak{L}_{\rm ph}} + \frac{1}{C\mathfrak{L}_{\rm co}} + \frac{R_{\rm in}}{\mathfrak{L}_{\rm in}}\frac{R_{\rm ph}}{\mathfrak{L}_{\rm ph}} + \frac{R_{\rm in}}{\mathfrak{L}_{\rm in}}\frac{R_{\rm co}}{\mathfrak{L}_{\rm co}} + \frac{R_{\rm ph}}{\mathfrak{L}_{\rm ph}}\frac{R_{\rm co}}{\mathfrak{L}_{\rm co}} \right) \\ & - \lambda \left(\frac{1}{C\mathfrak{L}_{\rm co}}\frac{R_{\rm ph}}{\mathfrak{L}_{\rm ph}} + \frac{1}{C\mathfrak{L}_{\rm ph}}\frac{R_{\rm co}}{\mathfrak{L}_{\rm co}} + \frac{1}{C\mathfrak{L}_{\rm co}}\frac{R_{\rm in}}{\mathfrak{L}_{\rm in}} + \frac{1}{C\mathfrak{L}_{\rm in}}\frac{R_{\rm co}}{\mathfrak{L}_{\rm co}} \right. \\ & \qquad \left. + \frac{1}{C\mathfrak{L}_{\rm ph}}\frac{R_{\rm in}}{\mathfrak{L}_{\rm in}} + \frac{1}{C\mathfrak{L}_{\rm in}}\frac{R_{\rm ph}}{\mathfrak{L}_{\rm ph}} + \frac{R_{\rm in}}{\mathfrak{L}_{\rm in}}\frac{R_{\rm ph}}{\mathfrak{L}_{\rm ph}}\frac{R_{\rm co}}{\mathfrak{L}_{\rm co}} \right) \\ & + \frac{1}{C\mathfrak{L}_{\rm in}}\frac{R_{\rm ph}}{\mathfrak{L}_{\rm ph}}\frac{R_{\rm co}}{\mathfrak{L}_{\rm co}} + \frac{1}{C\mathfrak{L}_{\rm ph}}\frac{R_{\rm in}}{\mathfrak{L}_{\rm in}}\frac{R_{\rm co}}{\mathfrak{L}_{\rm co}} + \frac{1}{C\mathfrak{L}_{\rm co}}\frac{R_{\rm in}}{\mathfrak{L}_{\rm in}}\frac{R_{\rm ph}}{\mathfrak{L}_{\rm ph}}. \end{aligned} \tag{5.89}$$

Hence all the constants ($I^*_{2,1}$, $I^*_{2,2}$, $I^*_{4,1}$, $I^*_{4,2}$, $I^*_{5,1}$, $I^*_{5,2}$, and λ) needed for the currents I_2, I_4, and I_5 (Eqs. (5.72), (5.73), and (5.74)) are determined as a function of U. The currents I_1 and I_3 follow from Eq. (5.39) and (5.40).

Here the characteristic Eq. (5.89) is of higher order in λ (forth order) than in the case of step 1 (third order, see Eq. (5.58)). Using the reciprocal time-scales from the Eqs. (5.59) and (5.60) together with

$$\delta_{\rm co} = \frac{R_{\rm co}}{\mathfrak{L}_{\rm co}} = 1.71 \times 10^{-13}\, {}^{1}/_{\rm s}, \qquad \text{and} \qquad \lambda_{\rm co} = \frac{1}{\sqrt{C\mathfrak{L}_{\rm co}}} = 48.7\, {}^{1}/_{\rm s}. \tag{5.90}$$

the characteristic equation (Eq. (5.89)) becomes

$$0 = \lambda^4 - \lambda^3 \times 4.99 \times 10^{-9}\,{}^1\!/\!_{\mathrm{s}} + \lambda^2 \times 1.10 \times 10^4\,{}^1\!/\!_{\mathrm{s}^2} - \lambda \times 3.29 \times 10^{-5}\,{}^1\!/\!_{\mathrm{s}^3} + 1.47 \times 10^{-14}\,{}^1\!/\!_{\mathrm{s}^4}. \quad (5.91)$$

The influence of the characteristic equation's coefficients (see Eq. (5.89)) can be summarised with $\delta_{\mathrm{co}} \ll \delta_{\mathrm{ph}} \lesssim \delta_{\mathrm{in}} \ll \lambda_{\mathrm{co}} < \lambda_{\mathrm{ph}} < \lambda_{\mathrm{in}}$. The inductive and capacitive components of the electric circuit dominate the discharging process of the capacitor.

According to the fundamental theorem of algebra (see e.g., Bronstein *et al.*, 1999) this equation possesses four solutions. Two of them are real and the other two are complex. They can be evaluated numerically, i.e.,

$$\lambda_1 = 5.46 \times 10^{-10}\,{}^1\!/\!_{\mathrm{s}} \quad (5.92)$$
$$\lambda_2 = \left(1.01 \times 10^{-9} - \imath\,1.05 \times 10^2\right)\,{}^1\!/\!_{\mathrm{s}} \quad (5.93)$$
$$\lambda_3 = \overline{\lambda_2} = \left(1.01 \times 10^{-9} + \imath\,1.05 \times 10^2\right)\,{}^1\!/\!_{\mathrm{s}} \quad (5.94)$$
$$\lambda_4 = 2.43 \times 10^{-9}\,{}^1\!/\!_{\mathrm{s}}. \quad (5.95)$$

Here $\imath$ represents the complex unit, i.e., $\imath^2 = -1$.

Since the eigenvalues are found (see Eq. (5.92) to (5.95)) the currents needed for the complete solution of the circuit can be determined next: The laws of Kirchhoff (from Eqs. (5.39) to (5.43)) describe the whole circuit as presented in Fig. 5.4(a). In order to solve these equations, I_3 can be eliminated by combining the Eqs. (5.39) and (5.40) with each other, i.e., $I_1 = I_2 + I_4 + I_5$. This new relation can be used in the equations for the three meshes, so that I_1 is also eliminated, i.e.,

$$U = (R_{\mathrm{ph}} + R_{\mathrm{in}})\,I_2 + (\mathfrak{L}_{\mathrm{ph}} + \mathfrak{L}_{\mathrm{in}})\,\frac{\mathrm{d}I_2}{\mathrm{d}t} + \mathfrak{L}_{\mathrm{in}}\frac{\mathrm{d}I_4}{\mathrm{d}t} + \mathfrak{L}_{\mathrm{in}}\frac{\mathrm{d}I_5}{\mathrm{d}t} + R_{\mathrm{in}}I_4 + R_{\mathrm{in}}I_5 \quad (5.96)$$
$$0 = U_{\mathrm{cap}} - \mathfrak{L}_{\mathrm{ph}}\frac{\mathrm{d}I_2}{\mathrm{d}t} - R_{\mathrm{ph}}I_2 \quad (5.97)$$
$$0 = R_{\mathrm{co}}I_5 + \mathfrak{L}_{\mathrm{co}}\frac{\mathrm{d}I_5}{\mathrm{d}t} - U_{\mathrm{cap}}. \quad (5.98)$$

The time derivative of Eq. (5.45) gives

$$\frac{\mathrm{d}U_{\mathrm{cap}}}{\mathrm{d}t} = \frac{1}{C}I_4. \quad (5.99)$$

If the solutions for the four quantities I_2, I_4, I_5, and U_{cap} are determined (from the four linear differential Eqs. (5.96) to (5.99) of first order) the circuit is solved. The fundamental solution of the differential equation system has four linear independent eigenvectors, for the four different eigenvalues λ_1, $\lambda_2 = \overline{\lambda_3}$, λ_4 (see Eqs. (5.92) to (5.95)). Hence I_2, I_4, I_5, and U_{cap} need to have the following structure

$$I_2[t] = I_{2,5} + \sum_{o=1}^{4}\left[I_{2,o}\exp[-\lambda_o t]\right] \quad (5.100)$$
$$I_4[t] = I_{4,5} + \sum_{o=1}^{4}\left[I_{4,o}\exp[-\lambda_o t]\right] \quad (5.101)$$
$$I_5[t] = I_{5,5} + \sum_{o=1}^{4}\left[I_{5,o}\exp[-\lambda_o t]\right] \quad (5.102)$$
$$U_{\mathrm{cap}}[t] = U_{\mathrm{cap},5} + \sum_{o=1}^{4}\left[U_{\mathrm{cap},o}\exp[-\lambda_o t]\right]. \quad (5.103)$$

In general a solution of such a problem is given by the sum of the general solution of the homogeneous equation system and a particular solution of the inhomogeneous system. A solution of the stationary problem is a special one. The stationary problem is described by the equations

$$
\begin{aligned}
U &= (R_{\text{ph}} + R_{\text{in}})\, I_2 + R_{\text{in}} I_5 && (5.104)\\
0 &= U_{\text{cap}} - R_{\text{ph}} I_2 && (5.105)\\
0 &= R_{\text{co}} I_5 - U_{\text{cap}}, && (5.106)
\end{aligned}
$$

which when combined lead to the results

$$
\begin{aligned}
I_2 &= \frac{R_{\text{co}} U}{R_{\text{ph}} R_{\text{co}} + R_{\text{in}} R_{\text{co}} + R_{\text{in}} R_{\text{ph}}} =: I_{2,5} && (5.107)\\
I_5 &= \frac{R_{\text{ph}} U}{R_{\text{ph}} R_{\text{co}} + R_{\text{in}} R_{\text{co}} + R_{\text{in}} R_{\text{ph}}} =: I_{5,5} && (5.108)\\
U_{\text{cap}} &= \frac{R_{\text{co}} R_{\text{ph}} U}{R_{\text{ph}} R_{\text{co}} + R_{\text{in}} R_{\text{co}} + R_{\text{in}} R_{\text{ph}}} =: U_{\text{cap},5}. && (5.109)
\end{aligned}
$$

Therefore the stationary equations determine three of the unknown constants and the other coefficients (i.e., $I_{2,o}$, $I_{5,o}$, and $U_{\text{cap},o}$ for $o \in \{1, 2, 3, 4\}$) are evaluated in the following. However the calculations for this part are quite lengthy but straightforward. Therefore it seems to be the best way to lay out a sketch about how the calculations are done, instead of presenting each step in detail. Indeed what comes next is comparable to what was done previously in this chapter: The Eqs. (5.100) to (5.103) are inserted into the Eqs. (5.96) to (5.99). By comparing the coefficients in the resulting equations, a new set of equations is obtained, which allow to determine the unknown coefficients. In the course of these calculations, the following three relations can be obtained

$$
\begin{aligned}
I_{4,o} &= \lambda_o C \left(R_{\text{ph}} - \lambda_o \mathfrak{L}_{\text{ph}}\right) I_{2,o} && (5.110)\\
I_{5,o} &= \frac{R_{\text{ph}} - \lambda_o \mathfrak{L}_{\text{ph}}}{R_{\text{co}} - \lambda_o \mathfrak{L}_{\text{co}}} I_{2,o} && (5.111)\\
U_{\text{cap},o} &= \left(R_{\text{ph}} - \lambda_o \mathfrak{L}_{\text{ph}}\right) I_{2,o}, && (5.112)
\end{aligned}
$$

and $I_{4,5} = 0$ is found. The initial conditions in the circuit, which need to be satisfied are the conditions at $t \to \infty$ from step 1:

$$
\begin{aligned}
I_4[t=0] &= 0 = I_{4,1} + I_{4,2} + I_{4,3} + I_{4,4} && (5.113)\\
I_5[t=0] &= 0 = I_{5,1} + I_{5,2} + I_{5,3} + I_{5,4} + I_{5,5} && (5.114)\\
U_{\text{cap}}[t=0] &= U_{\text{cap},0} = U_{\text{cap},1} + U_{\text{cap},2} + U_{\text{cap},3} + U_{\text{cap},4} + U_{\text{cap},5}\\
&= \frac{R_{\text{ph}}}{R_{\text{ph}} + R_{\text{in}}} U. && (5.115)
\end{aligned}
$$

Therefore all the components $I_{4,o}$, $I_{5,o}$ and $U_{\text{cap},o}$ can be found by using Eqs. (5.110) to (5.115), if the $I_{2,o}$ are determined for all $o \in \{1, 2, 3, 4\}$.

$$
\begin{aligned}
\left(\frac{R_{\text{ph}}}{R_{\text{ph}} + R_{\text{in}}} - \frac{R_{\text{co}}}{R_{\text{in}}}\right) \frac{U}{R_{\text{ph}}} &= \sum_{o=1}^{4} \left[\frac{{}^{R_{\text{ph}}}\!/\!{}_{\mathfrak{L}_{\text{ph}}} - \lambda_o}{{}^{R_{\text{ph}}}\!/\!{}_{\mathfrak{L}_{\text{ph}}}} I_{2,o}\right] && (5.116)\\
\left(\frac{1}{R_{\text{ph}} + R_{\text{in}}} - \frac{R_{\text{co}}}{R_{\text{ph}} R_{\text{in}}}\right) U &= \sum_{o=1}^{4} \left[I_{2,o}\right] && (5.117)\\
0 &= \sum_{o=1}^{4} \left[C \mathfrak{L}_{\text{ph}} \lambda_o \left({}^{R_{\text{ph}}}\!/\!{}_{\mathfrak{L}_{\text{ph}}} - \lambda_o\right) I_{2,o}\right] && (5.118)\\
-\frac{U}{R_{\text{in}}} &= \sum_{o=1}^{4} \left[\frac{\mathfrak{L}_{\text{ph}}}{\mathfrak{L}_{\text{co}}} \frac{{}^{R_{\text{ph}}}\!/\!{}_{\mathfrak{L}_{\text{ph}}} - \lambda_o}{{}^{R_{\text{co}}}\!/\!{}_{\mathfrak{L}_{\text{co}}} - \lambda_o} I_{2,o}\right]. && (5.119)
\end{aligned}
$$

Hence the mathematically formulated problem can is solved by

$$
{}^{I_{2,1}}\!/\!{}_{U} = 5.11 \times 10^{6}\,\text{A} + i\, 8.32 \times 10^{-22}\,\text{A} \qquad (5.120)
$$

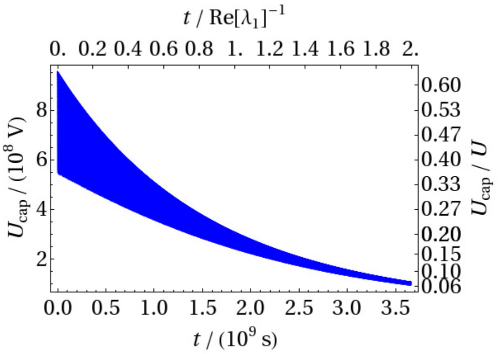

(a) Plot of U_{cap} against the time.

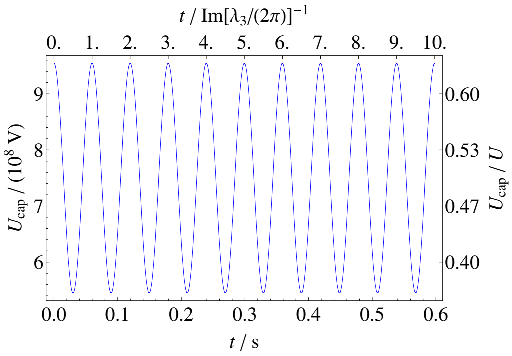

(b) Plot of U_{cap} against the time.

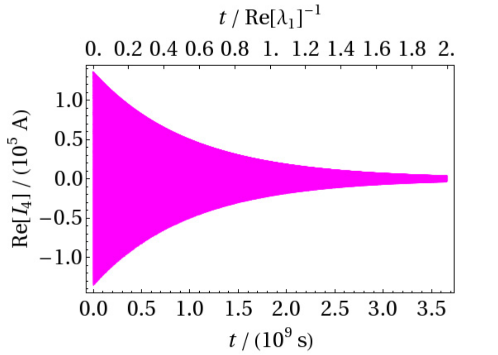

(c) Plot of I_4 against the time.

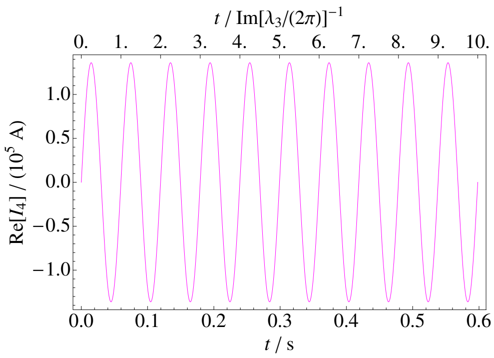

(d) Plot of I_4 against the time.

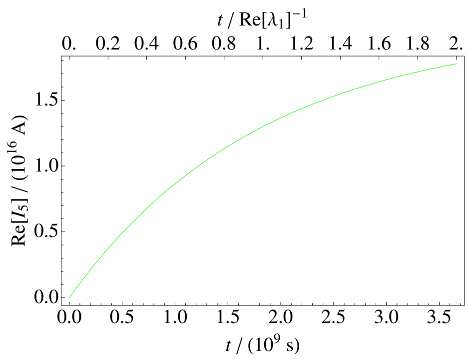

(e) Plot of I_5 against the time.

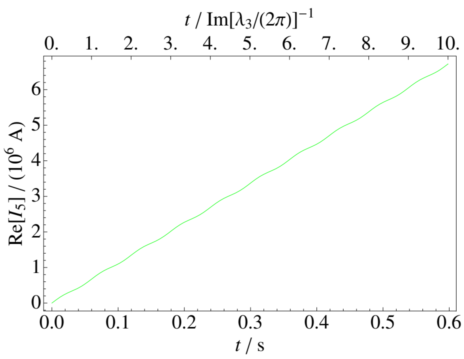

(f) Plot of I_5 against the time.

Figure 5.9: These six diagrams present, how the initially completely charged capacitor in Fig. 5.7(b) is discharged, when the switch S_{co} is closed. All diagrams consider $U = 1.5 \times 10^9\,\mathrm{V}$. The diagrams on the left hand side present the long term, whereas the ones on the right hand side the short term behaviour.

$$I_{2,2}/U = -1.92 \times 10^{-16}\,\mathrm{A} - i\,1.17 \times 10^{-5}\,\mathrm{A} \tag{5.121}$$

$$I_{2,3}/U = -1.92 \times 10^{-16}\,\mathrm{A} + i\,1.17 \times 10^{-5}\,\mathrm{A} \tag{5.122}$$

$$I_{2,4}/U = 1.36 \times 10^{5}\,\mathrm{A} + i\,3.15 \times 10^{-21}\,\mathrm{A}. \tag{5.123}$$

Discussion:

Initially the capacitor in the circuit diagram shown in Fig. 5.4(a) is considered to be fully charged (see Eq. (5.115)). Then the switch S_{co} is closed at $t = 0$ and in the following the capacitor

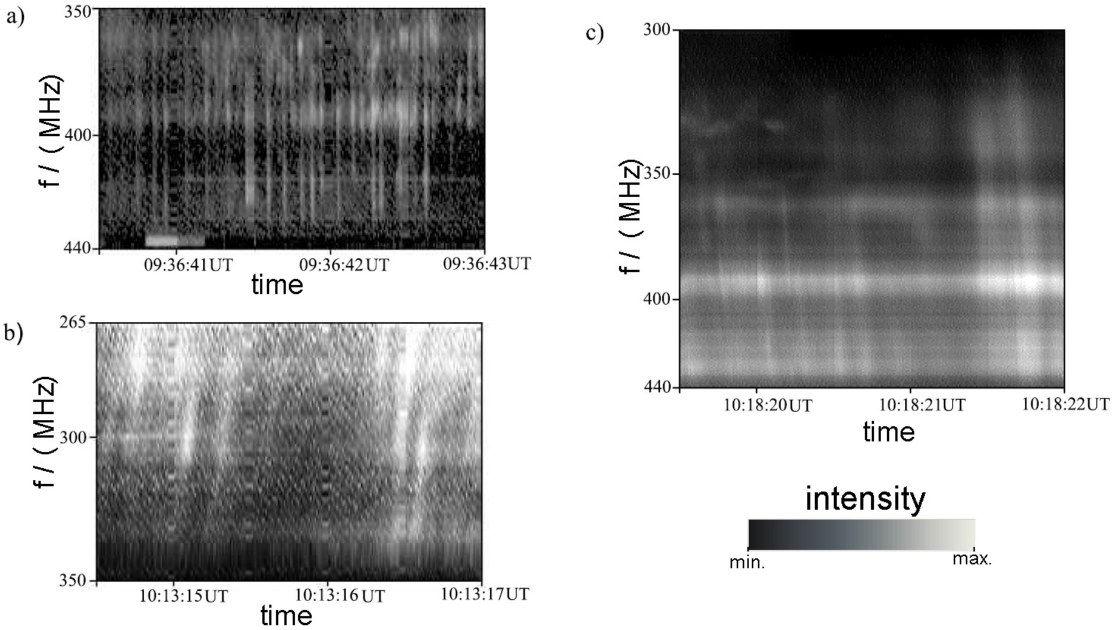

Figure 5.10: The radio diagrams presented here have been recorded by the digital solar radiospectrograph *Artemis-IV*, located at the Thermopylae station. It is operated by the University of Athens in Greece and covers the frequency range from 20 MHz to 650 MHz with a temporal resolution of 100 ms. However in the frequency range 270 MHz to 450 MHz a temporal resolution of 10 ms can be obtained (Caroubalos *et al.*, 2001). The three radio diagrams show simple broadband Super-short solar radio bursts (SSS bursts) recorded on April 15, 2000: a) SSS pulsations, b) SSSs with a negative drift velocity, and c) SSSs with a positive drift velocity can be seen. Reference: Magdalenić (2007).

discharges, i.e., U_{cap} diminishes exponentially.

The relevant time-scales for this process can be evaluated from Eqs. (5.92) to (5.95), i.e.,

$$\tau_1 = {}^1\!/\!_{\lambda_1} = 1.83 \times 10^9\,\text{s} \approx 58\,\text{yr} \tag{5.124}$$
$$\tau_2 = {}^1\!/\!_{\lambda_2} = \left(9.11 \times 10^{-14} + \imath\, 9.52 \times 10^{-3}\right)\,\text{s} \tag{5.125}$$
$$\tau_3 = {}^1\!/\!_{\lambda_3} = \overline{\tau_2} = \left(9.11 \times 10^{-14} - \imath\, 9.52 \times 10^{-3}\right)\,\text{s} \tag{5.126}$$
$$\tau_4 = {}^1\!/\!_{\lambda_4} = 4.11 \times 10^8\,\text{s} \approx 13\,\text{yr}. \tag{5.127}$$

The complex solutions τ_2 and τ_3 have small real parts, whereas their imaginary component causes an oscillation with the frequency of ${}^{|\text{Im}[\lambda_2]|}\!/\!_{(2\pi)} = {}^{|\text{Im}[\lambda_3]|}\!/\!_{(2\pi)} \approx 16.7\,\text{Hz}$. This oscillation frequency corresponds to a duration period of approximately 60 ms. Indeed the same oscillation frequency has been found recently: Figure 5.10 presents the so-called super-short solar radio bursts (SSS bursts) (Magdalenić, 2007). These burst signatures were observed accompanying explosive energy releases. Magdalenić *et al.* (2006) report that SSS bursts have durations at half-power ranging from 4 ms to 60 ms, which is in good agreement with the time-scale of oscillation calculated here. Moreover this time-scale of the oscillation agrees well with the time periods of observed hard X-ray pulses (Aschwanden *et al.*, 1995a).

However the time-scales τ_1 and τ_4 are far too high to be relevant during flare processes. Figure 5.9(a) presents the discharging process of the capacitor: The very high inductivities in the circuit are the reason for a quite long (i.e., 58 yr, see Eq. (5.124)) characteristic time-scale needed to discharge the capacitor. Nevertheless the capacitor's voltage shows oscillations with durations of about 60 ms as it can be seen in Fig. 5.9(b). The change of the capacitor's voltage is related with an increasing current through the corona (I_5) as it is seen in Fig. 5.9(e). Due to the same reason the capacitor current diminishes (I_4) as presented in Fig. 5.9(c). Again both of these currents oscillate with the same period (60 ms) as the capacitor's voltage.

Summarising:

It is found that the proposed mechanism considered to drive the solar flare can be the photospheric plasma motion. Indeed due to the photospheric motion more energy than needed for a flare can be generated. As a result of magnetic reconnection magnetic field lines can establish, which interconnect the photospheric power sources. Subsequently the energy is released in the corona by means of magnetic field aligned electric currents establishing themselves in the corona, due to the three orders of magnitude higher coronal electric conductivity. In order to discuss this briefly summarised mechanism, electric circuit models are used to model a solar flare. The circuits are modelled using values obtained from observations. It has been shown that the energy release in the corona is in accordance with the observed energy releases of solar flares.

One other important result found using these circuits is that currents which establish through the corona and connect photospheric regions of different magnetic polarities with each other, are accompanied by counter-streaming electric currents. This can be an explanation, why X-ray flare observations usually show two hard X-ray sources (e.g., see Fig. 3.7(a)). According to this explanation the electrons of each coronal conductor generate hard X-ray sources in the dense solar atmosphere, i.e., close to the footpoint region of the magnetic field connection.

High electric currents are accompanied with high magnetic flux densities. *RHESSI* observations indicate that an electric current of $I_{RHESSI} = |eF_{\mathrm{e}}| \approx 1.3 \times 10^{17}\,\mathrm{A}$ (see Sect. 3.2.1) is the source for the hard X-ray sources. Such an electric current would be accompanied by a magnetic flux density in the corona of about $B \approx {}^{\mu_0 I_{RHESSI}}/_{L_{\mathrm{s}}} = 2.28 \times 10^3\,\mathrm{T} = 2.28 \times 10^7\,\mathrm{G}$. Here μ_0 represents the vacuum permeability. However magnetic fields of this order of magnitude are not observed in the corona. The circuit model presented in this thesis provides a possible answer for this problem: Since the electric currents appear pairwise and are oppositely directed, the corresponding large magnetic field strengths generated by those currents can be annihilated.

Moreover by considering the inductive and capacitive components of the circuit, the model predicts electric current oscillations. The oscillation period is found to be 60 ms. As explained this time-scale agrees very well with reported the durations of SSS bursts (Magdalenić *et al.*, 2006).

CHAPTER 6

Electron acceleration

Electrons are charged and light particles. Due to their little mass the electron's inertia is very low. Therefore electron trajectories are mainly influenced by the electromagnetic force, whereas the weak gravitative interaction can be neglected in general.

The electromagnetic force has two contributions, i.e., the magnetic and the electric interaction. Since the magnetic force component (Lorentz force) acts perpendicular to the plane defined by the electron's velocity vector and the local magnetic flux density vector, the static magnetic force cannot accelerate the electron to higher energies. Indeed it is found that charged particles gyrate while they drift along magnetic field lines. The gyration frequency is a function of the strength of the magnetic flux density. Depending on the magnetic field configuration, e.g., charged particles can be rerouted or even as in the case of the magnetic bottle be "captured". Since the magnetic momentum is an adiabatic constant of motion (see e.g., Baumjohann & Treumann, 1996; Kegel, 1998) the magnetic field topology is responsible for transforming gyration energy into drift energy and vice versa. On the other hand electric fields lead to direct electron acceleration. In result the electron gains energy as long as it is accelerated against the direction of the electric field.

In the following the most direct way of electron acceleration caused by a static large-scale electric field is discussed and the Dreicer field is introduced. Finally the electron acceleration within a plasma tube inhomogeneously filled with an electron-proton plasma is investigated and the method for determining the electron flux spectra is explained.

6.1 Electric field acceleration & Coulomb collisions

Consider an electron within a coronal magnetic flux tube filled with an electron-proton plasma. Along the magnetic flux tube, i.e., parallel to the magnetic flux density, an electric field shall be present. In such a case the three dimensional equation of motion determining the electron's trajectory can be simplified using the Alfvén's gyro centre approximation. Hence the particle motion can be separated into two different motions, i.e., the one dimensional drift motion (which is parallel to the magnetic flux density vector) and the two dimensional gyro motion (which is perpendicular to the magnetic flux density vector). Expressing the drift motion by means of the electron's velocity parallel to the magnetic flux density vector, and using the electron's velocity perpendicular to the magnetic flux density vector in order to describe the gyro motion, the equations of motion can be formulated in a "two dimensional" manner, i.e., field parallel and perpendicular motion.

Since the acceleration along the magnetic flux density is investigated in this thesis, i.e., the electric field is considered to be aligned along the magnetic flux density in the corona, and therefore

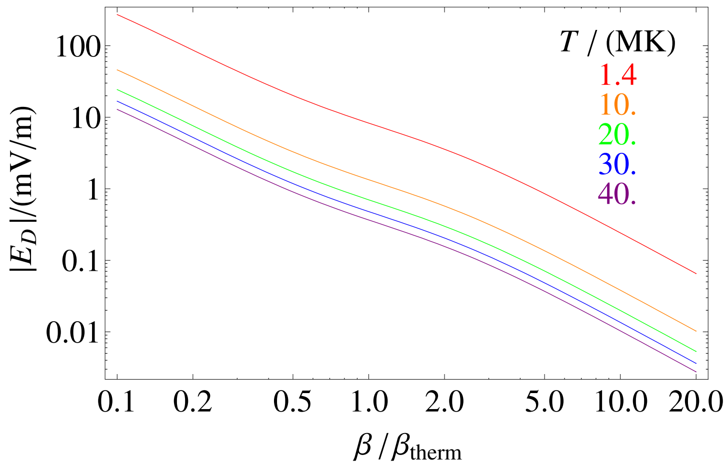

Figure 6.1: The absolute value of the Dreicer field $|E_\mathrm{D}|$ is shown in dependence on the normalised velocity $\beta/\beta_{\mathrm{th}}$ for several different temperatures and a constant particle density of $N_\mathrm{e} = 10^{15}\,\mathrm{m}^{-3}$.

the field perpendicular part of the electron motion can be neglected for these considerations.

Therefore the equation of motion for an electron[1] can be written in its one dimensional form

$$\frac{\mathrm{d}p}{\mathrm{d}t} = -eE - m_\mathrm{e}\,\mathrm{sign}[p]\,\left|D\right|. \tag{6.1}$$

Here t, c, and $p = m_\mathrm{e} c\,\beta\left(1-\beta^2\right)^{-1/2}$ denote the time, the speed of light, and the electron's momentum, respectively. The normalised electron velocity β is given by $\beta = V/c$ with $V = \mathrm{d}x/\mathrm{d}t$ as the electron's velocity, i.e.,

$$\frac{\mathrm{d}x}{\mathrm{d}t} = c\beta. \tag{6.2}$$

The x axis is assumed to be oriented parallelly to the magnetic flux density vector. Therefore x stands for the spatial position of the electron within the one dimensional magnetic flux tube.

The quantity D represents the electron's deceleration due to Coulomb collisions (Önel *et al.*, 2007). By inserting the expression for the electron's momentum into Eq. (6.1)

$$\frac{\mathrm{d}p}{\mathrm{d}t} = m_\mathrm{e} c\gamma^3\frac{\mathrm{d}\beta}{\mathrm{d}t} = -eE - m_\mathrm{e}\,\mathrm{sign}[\beta]\,\left|D\right| \tag{6.3}$$

is obtained, if the abbreviation $\gamma = \left(1-\beta^2\right)^{-1/2}$ for the Lorentz factor γ is used. The momentum change per arc length x along the x axis can be derived from Eq. (6.3)

$$\frac{\mathrm{d}p}{\mathrm{d}x} = m_\mathrm{e} c\,\gamma^3\frac{\mathrm{d}\beta}{\mathrm{d}x} = \frac{1}{\beta c}\frac{\mathrm{d}p}{\mathrm{d}t} = \frac{1}{\beta c}\left(-eE - m_\mathrm{e}\,\mathrm{sign}[\beta]\,\left|D\right|\right). \tag{6.4}$$

An electron traversing through an electron-proton plasma experiences Coulomb collisions, which means an energy loss for the electron. Thus the electron momentum changes by deceleration, as described in the very last sum of Eq. (6.3). The Coulomb deceleration D in an electron-proton plasma has two contributions, namely the electron-electron interaction D_e and the electron-proton interaction D_p, i.e., $D = D_\mathrm{e} + D_\mathrm{p}$. Each of these contributions is given by

$$\forall\varsigma \in \{\mathrm{e},\mathrm{p}\} : D_\varsigma = \frac{Z_\varsigma^2 e^4\, N_\varsigma \ln[\Lambda_\varsigma]}{4\pi\varepsilon_0^2\left(1/m_\mathrm{e} + 1/m_\varsigma\right)^{-2} c^2\beta_\varsigma^2} \qquad \text{for} \qquad \beta_\varsigma \neq 0. \tag{6.5}$$

[1] The electron carries the negative elementary charge $-e$ and possesses the rest mass m_e.

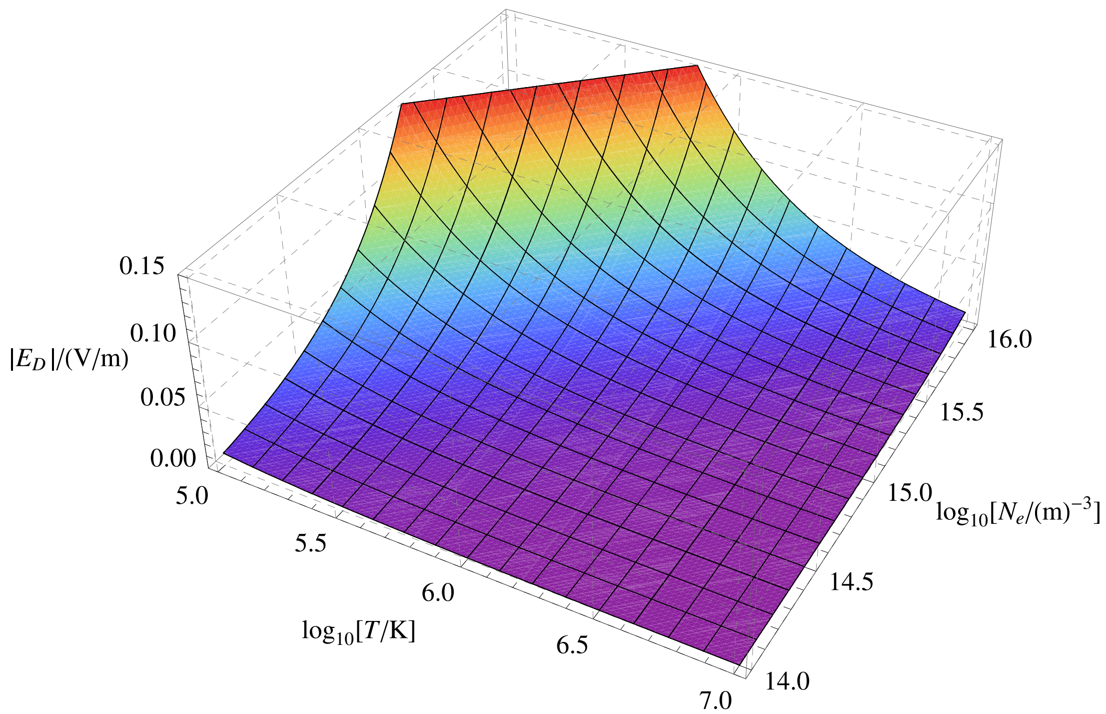

Figure 6.2: The absolute value of the Dreicer field $\left|E_\mathrm{D}\right|$ is shown in dependence on the logarithm of the plasma temperature T and the logarithm of electron density N_e for the case $\beta_\mathrm{D} = \beta_\mathrm{th}$.

Here Z_ς represents the charge number[1], m_ς the rest mass, and N_ς the number density of the particle species $\varsigma \in \{\mathrm{e}$ for "electron", p for "proton"$\}$. The quantity ε_0 stands for the permittivity of free space, whereas β_ς represents the relative velocity of the electron with respect to the one of the electrons and the protons of the plasma, in which the electron propagates. According to Appendix C (pg. 89) $\beta_\mathrm{e} = \sqrt{\beta^2 + 3\beta_\mathrm{th}^2}$ and $\beta_\mathrm{p} \approx \beta$ are the relative velocities of the electron in motion with respect to electrons and protons of the (background) plasma, respectively. The thermal velocity normalised to the speed of light is named $\beta_\mathrm{th} = \left({}^{k_\mathrm{B}T}/{}_{(m_\mathrm{e}c^2)}\right)^{1/2}$. Furthermore the Coulomb logarithm is given by

$$\ln\left[\Lambda_\varsigma\right] = \ln\left[\sqrt{\frac{\lambda_\mathrm{D}^2 + b_{0,\varsigma}^2}{2b_{0,\varsigma}^2}}\right], \tag{6.6}$$

with the Debye length

$$\lambda_\mathrm{D} = \sqrt{\frac{\varepsilon_0 k_\mathrm{B} T}{N_\mathrm{e} e^2}} \tag{6.7}$$

and the Coulomb collision impact parameter

$$b_{0,\varsigma} = \left|\frac{e^2}{4\pi\varepsilon_0 c^2} \cdot \frac{Z_\varsigma}{\left({}^1/{}_{m_\mathrm{e}} + {}^1/{}_{m_\varsigma}\right)^{-1} \beta_\varsigma^2}\right|. \tag{6.8}$$

As it can be seen from Eq. (6.3) a special electric field

$$E_\mathrm{D} = -\left(\frac{m_\mathrm{e}}{e}\,\mathrm{sign}[\beta]\left|D\right|\right)\Bigg|_{\beta=\beta_\mathrm{D}} \tag{6.9}$$

[1] In a fully ionized electron-proton plasma $Z_\mathrm{e} = 1$ and $Z_\mathrm{p} = 1$ is satisfied. A fully ionised Helium atom (i.e., α-particle) would have $Z_\alpha = 2$.

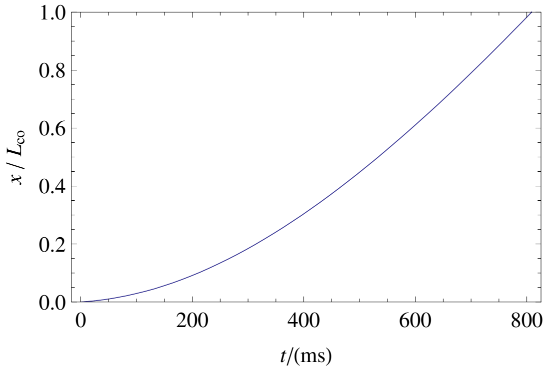

(a) The position of the electron in the coronal loop ${}^{x}/_{L_{\mathrm{co}}}$ is plotted in dependence on the time t.

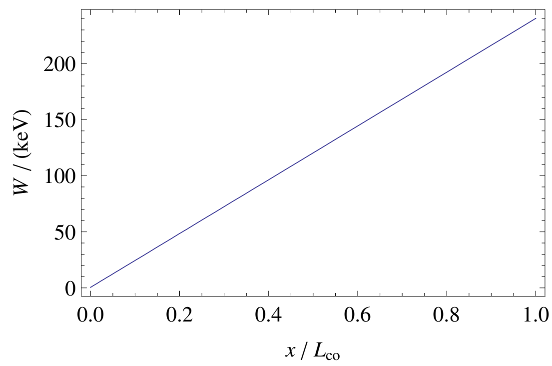

(b) The electron's relativistic kinetic energy W is plotted in dependence on the position of the electron in the coronal loop ${}^{x}/_{L_{\mathrm{co}}}$.

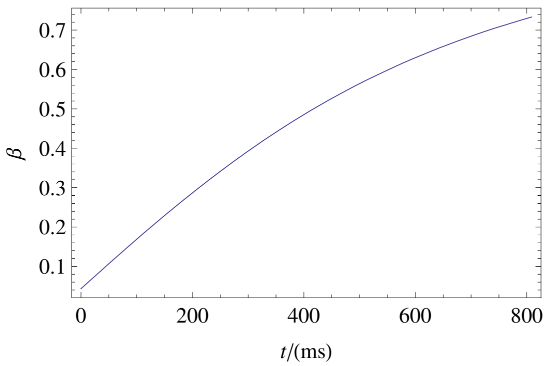

(c) The electron's normalised velocity β is plotted in dependence on the time t.

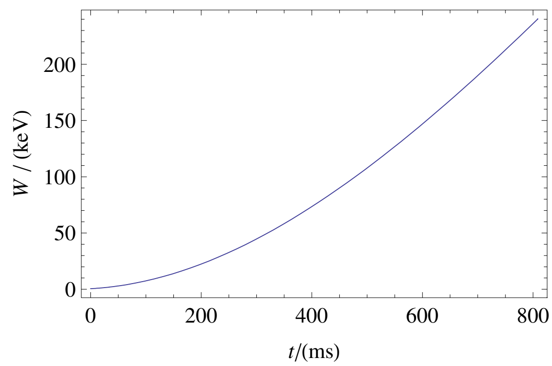

(d) The electron's relativistic kinetic energy W is plotted in dependence on the time t.

Figure 6.3: The solutions of the numerically solved relativistic electron acceleration problem, as explained in Sect. 6.1.1 are shown.

exists, which leads to a vanishing time derivation of the electron's momentum, i.e., ${}^{\mathrm{d}p}/_{\mathrm{d}t} = 0$. For each given critical electric field, also a critical velocity, the so-called Dreicer velocity β_{D} exists, which characterises the change of the electron's momentum. If $\beta_{\mathrm{D}} = \beta_{\mathrm{th}}$ is chosen, this special field E_{D} is called Dreicer (1959, 1960) field. The critical velocity acts as a sort of switch for the electron acceleration problem. Indeed electrons below this critical velocity experience many Coulomb collisions, whereas for faster electrons, the collisions can be neglected. This means that those electrons, which satisfy $|\beta| < |\beta_{\mathrm{D}}|$ are continuously decelerated and become thermalised plasma due to collisions. On the other hand those electrons, which fulfil $|\beta| > |\beta_{\mathrm{D}}|$, do not experience Coulomb collisions. They are called runaway electrons (e.g., Holman, 1995; Lifshitz & Pitaevskii, 1990), and their velocity increases without restrictions (within the limits of the theory of relativity).

The quantity of E_{D} (see Eq. (6.9)) is visualised in Fig. 6.1 for several different plasma temperatures in dependence on the normalised electron velocity. Moreover Fig. 6.2 shows the dependence of the absolute value of E_{D} on N_{e} and T for $\beta_D = \beta_{\mathrm{th}}$.

6.1.1 Simple example for the electron acceleration problem

Next an exemplary solution shall be presented for the problem of electron acceleration: The Eqs. (6.2) and (6.3) can be simultaneously solved in a numerical way. In order to keep the example easy the magnetic flux tube is considered to be filled homogeneously ($N_{\mathrm{e}} = N_{\mathrm{co}} = 10^{15}\,\mathrm{m}^{-3}$, e.g.,

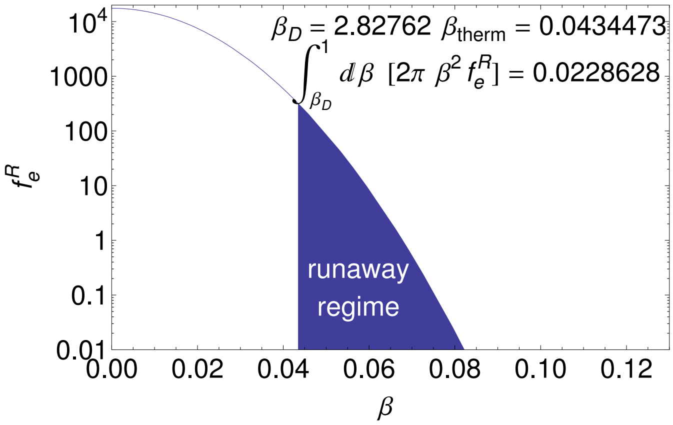

Figure 6.4: The to unity normalised relativistic Maxwellian velocity function f_e^R for electrons according to Eq. (6.34) is presented as a function of the normalised electron velocity β. The runaway region $\beta_\mathrm{D} < \beta$ is filled.

see Aschwanden (2002b)). Figure 6.3 shows the numerically obtained result of the explained endeavour for an electron traversing the whole loop with length $L_\mathrm{loop} = L_\mathrm{co} = {}^{(\pi L_\mathrm{s})}/_{2} \approx 110\,\mathrm{Mm}$. According to Eq. (5.21) the electric field is chosen to be $E_0 \approx -2.18 \times 10^{-3}\,{}^\mathrm{V}/_\mathrm{m}$, corresponding to the Dreicer velocity $\beta_\mathrm{D} = 2.83\,\beta_\mathrm{th}$.

Hence all the electrons initially possessing at least the Dreicer velocity $\beta_\mathrm{i} = \beta_\mathrm{D}$ are accelerated by that electric field. They reach the loop's ending in $t_\mathrm{acc} = 809\,\mathrm{ms}$ or less, depending on their initial velocity and their initial location. The electrons initially located at $x = 0$ and having the initial velocity of $\beta_\mathrm{i} = \beta_\mathrm{D} = 2.83\,\beta_\mathrm{th}$ are accelerated up to about $\beta_\mathrm{acc} = 0.733$, that corresponds to the kinetic energy of about 240 keV. Such values are typical time-scales for electron acceleration during solar flares (Aschwanden, 2002b).

Moreover using the relativistic Maxwellian velocity distribution $f_\mathrm{e}^\mathrm{R} = \mathcal{K}_\mathrm{Maxwell} \exp\left[-{}^{W}/_{k_\mathrm{B}T}\right]$ (as it is introduced later in Sect. 6.1.3 (Eq. (6.37), pg. 62) along with the normalisation[1] constant $\mathcal{K}_\mathrm{Maxwell}$), the question about how many electrons are accelerated, can be answered for this simple example. Here $W[\beta] = m_\mathrm{e}c^2\,(\gamma[\beta] - 1)$ stands for the electron's relativistic kinetic energy. For a temperature of $T = 1.4\,\mathrm{MK}$ the dimensionless normalisation constant becomes $\mathcal{K}_\mathrm{Maxwell} \approx 17\,526.1$. The relativistic Maxwell distribution function is presented in Fig. 6.4. If in accordance with the electric circuit model the circuit is closed through the corona and two electric currents are established (see Sect. 5.2), then

$$\frac{{}^{N_\mathrm{acc}}/_{2}}{N_\mathrm{co}} \quad = \quad \mathcal{K}_\mathrm{Maxwell} \int_{\beta_\mathrm{D}}^{1} \mathrm{d}\hat{\beta} \left[2\pi\,\hat{\beta}^2 \exp\left[\frac{1 - \gamma[\hat{\beta}]}{\beta_\mathrm{th}^2} \right] \right] \tag{6.10}$$

and thus ${}^{N_\mathrm{acc}}/_{N_\mathrm{co}} \approx 4.57\%$ electrons become accelerated, since these electrons are initially located in the runaway regime. This value is in very good accordance with the estimation presented in Eq. (3.3) (pg. 22). Next the total electron flux $F_\mathrm{e} = N_\mathrm{acc}\,A_\mathrm{s}\,\beta_\mathrm{acc}c \approx 7.89 \times 10^{35}\,{}^\mathrm{electrons}/_\mathrm{s}$ can be estimated using $N_\mathrm{co} = 10^{15}\,\mathrm{m}^{-3}$ $N_\mathrm{acc} = 4.57 \times 10^{13}\,\mathrm{m}^{-3}$, and $A_\mathrm{s} = 7.85 \times 10^{13}\,\mathrm{m}^2$ (see Sect. 3.2.1, pg. 20 and following). It (F_e) agrees well with the flux concluded from *RHESSI* observations (see Sect. 3.2.1).

6.1.2 Classical approach: Electron flux in a plasma

As already explained, collisions in the plasma have a large effect on the question of which electrons can be accelerated by the present electric field. It is shown in Sect. 6.1 that electrons which are

[1] Condition for normalisation: $\int_{-1}^{1} \mathrm{d}\hat{\beta}\,\left[f_\mathrm{e}^\mathrm{R}[\hat{\beta}]\right] = 1$.

faster than the Dreicer velocity $u > u_\mathrm{D}$, do not feel collisions, but the electrons slower $u \leq u_\mathrm{D}$ do. Henceforth the electron motion is considered in such a way that electrons faster than the Dreicer velocity are not influenced by collisions, whereas the collisions have to be considered for electrons slower than the Dreicer velocity:

In this classical approach the plasma tube is filled by a plasma which is subject to a classical, to unity normalised[1], one dimensional Maxwellian electron distribution

$$f_\mathrm{e}^\mathrm{C}[u] = \frac{1}{\sqrt{2\pi}} \exp\left[-\frac{u^2}{2}\right]. \tag{6.11}$$

Here $u = {}^{V}\!/\!{}_{v_\mathrm{th}}$ corresponds to the electron velocity V, which has been normalised to the thermal electron velocity $v_\mathrm{th} = \beta_\mathrm{th} c$. The Dreicer velocity normalised to the thermal electron velocity is represented by $u_\mathrm{D} = {}^{\beta_\mathrm{D}}\!/\!{}_{\beta_\mathrm{th}}$. Since the Dreicer velocity depends on the electron number density N_e and the plasma temperature T (see e.g., Fig. 6.2), and since the electron number density and the plasma temperature are connected with the location x of the electron in the plasma tube, the local Dreicer velocity depends on the spatial location in the tube $u_\mathrm{D} = u_\mathrm{D}[x, T]$. In the following the temperature inside the magnetic tube is considered to be constant.

The energy which a frictionless accelerated electron gains is

$$\Delta W = -eE\left(L_\mathrm{loop} - x_0\right) = -eEL_\mathrm{loop} x_\Delta. \tag{6.12}$$

The quantity $x_\Delta = (1 - {}^{x_0}\!/\!{}_{L_\mathrm{loop}})$ describes the electron's reversed but normalised spatial position. According to Eq. (6.12) the electron initially located at x_0, and possessing the initial velocity $u_0 > u_\mathrm{D}$ given in units of the thermal electron velocity, corresponding to the initial kinetic energy W_0 gains by frictionless acceleration the energy ΔW. After acceleration the final electron velocity given in units of the thermal electron velocity becomes u_f. Depending on the electron's initial velocity the following two cases have to be discussed.

Case $u_0 \leq u_\mathrm{D}$: In this case the electron is not accelerated, since the friction dominates its equation of motion (see Eq. (6.4)). Hence

$$u_0 = u_\mathrm{f} \qquad \text{for } u_0 \leq u_\mathrm{D} \tag{6.13}$$

is obtained.

Case $u_0 > u_\mathrm{D}$: As explained before the electron which is initially accelerated needs to be faster than u_D. The final electron velocity is obtained from the electron's final kinetic energy $W_\mathrm{f} = W_0 + \Delta W$. In the classical approach $W_0 = \left({}^{v_\mathrm{th}^2}\!/\!{}_2\right) m_\mathrm{e} u_0^2$ and $W_\mathrm{f} = \left({}^{v_\mathrm{th}^2}\!/\!{}_2\right) m_\mathrm{e} u_\mathrm{f}^2$ can be used together with Eq. (6.12), in order to obtain the relation $W_\mathrm{f} = \left({}^{v_\mathrm{th}^2}\!/\!{}_2\right) m_\mathrm{e} u_0^2 - eU\left(1 - {}^{x}\!/\!{}_{L_\mathrm{loop}}\right)$. By introducing $\epsilon_{a_\mathrm{acc}} = {}^{-(eU)}\!/\!{}_{(k_\mathrm{B}T)}$ the final electron velocity $u_\mathrm{f} = \sqrt{u_0^2 + 2\epsilon_{a_\mathrm{acc}}\left(1 - {}^{x_0}\!/\!{}_{L_\mathrm{loop}}\right)}$ can be evaluated. Thus

$$u_0 = \sqrt{u_\mathrm{f}^2 - 2\epsilon_{a_\mathrm{acc}}\left(1 - {}^{x_0}\!/\!{}_{L_\mathrm{loop}}\right)} \qquad \text{for } u_0 > u_\mathrm{D} \tag{6.14}$$

is found.

The electron distribution function

The initial distribution function from Eq. (6.11) can be written as

$$f_\mathrm{i,e}^\mathrm{C}[u_0] = \left(\mathcal{H}_0[u_\mathrm{D} - u_0] + \mathcal{H}_0[u_0 - u_\mathrm{D}]\right) \frac{1}{\sqrt{2\pi}} \exp\left[-\frac{u_0^2}{2}\right]. \tag{6.15}$$

Here $\mathcal{H}_{\mathcal{K}_3}$ stands for the Heaviside step function,

$$\mathcal{H}_{\mathcal{K}_3}[u] = \begin{cases} 0 & \text{for } u < 0 \\ \mathcal{K}_3 & \text{for } u = 0 \\ 1 & \text{for } u > 0 \end{cases} \tag{6.16}$$

[1]Condition for normalisation: $\int_{-\infty}^{\infty} \mathrm{d}\hat{u}\left[f_\mathrm{e}^\mathrm{C}[\hat{u}]\right] = 1$.

which can be defined as a piecewise constant function (see e.g., Abramowitz & Stegun, 1972, pg. 1020). The constant $\mathcal{K}_3$ is chosen to be $\mathcal{K}_3 = 0$ throughout this thesis.

Next the distribution function for the accelerated electrons is evaluated. Therefore the two cases discussed before are considered.

Case $u_0 \leq u_\mathrm{D}$: According to Eq. (6.13) the distribution function is not altered due to Coulomb collisions. Therefore the final distribution function

$$f^{\mathrm{C}}_{\mathrm{f,e}}[u_\mathrm{f}] = \mathcal{H}_0[u_\mathrm{D} - u_\mathrm{f}] \frac{1}{\sqrt{2\pi}} \exp\left[-\frac{u_\mathrm{f}^2}{2}\right] \tag{6.17}$$

is obtained.

Case $u_0 > u_\mathrm{D}$: The electrons are accelerated in this case, since the electric force $-eE$ dominates the equation of motion Eq. (6.13). As explained the faster the electron becomes, the less it feels Coulomb collisions. Indeed those electrons, which posses a higher velocity, than the local Dreicer velocity, can be considered to be accelerated frictionless, since the effect of the Coulomb collisions quickly become insignificantly small. Using Eq. (6.14) the final distribution function

$$f^{\mathrm{C}}_{\mathrm{f,e}}[u_\mathrm{f}] = \frac{\mathcal{H}_0\left[\sqrt{u_\mathrm{f}^2 - 2\epsilon_{a_\mathrm{acc}}\left(1 - \frac{x_0}{L_\mathrm{loop}}\right)} - u_\mathrm{D}\right]}{\sqrt{2\pi}} \exp\left[-\frac{u_\mathrm{f}^2 - 2\epsilon_{a_\mathrm{acc}}\left(1 - \frac{x_0}{L_\mathrm{loop}}\right)}{2}\right], \tag{6.18}$$

is found. By introducing $\epsilon = {}^{W}\!/_{(k_\mathrm{B}T)} = {}^{u^2}\!/_2$, i.e., $\epsilon_\mathrm{f} = {}^{u_\mathrm{f}^2}\!/_2$ and $\epsilon_\mathrm{D} = {}^{u_\mathrm{D}^2}\!/_2$, the Eq. (6.18) becomes

$$f^{\mathrm{C}}_{\mathrm{f,e}} = \frac{\mathcal{H}_0\left[\epsilon_\mathrm{f} - \epsilon_{a_\mathrm{acc}}\left(1 - \frac{x_0}{L_\mathrm{loop}}\right) - \epsilon_\mathrm{D}\right]}{\sqrt{2\pi}} \exp\left[-\left(\epsilon_\mathrm{f} - \epsilon_{a_\mathrm{acc}}\left(1 - \frac{x_0}{L_\mathrm{loop}}\right)\right)\right]. \tag{6.19}$$

Hence the Eqs. (6.17) and (6.19) represent the final form of the classical distribution function of the accelerated electrons in the velocity ranges $u_0 \leq u_\mathrm{D}$ and $u_0 > u_\mathrm{D}$, respectively.

Having the electron distribution function for the accelerated electrons determined, the electron flux in the homogeneously filled magnetic flux tube is evaluated next: Therefore it is assumed that N_e is constant. Then the total electron flux along the plasma tube is defined by

$$\Phi = N_\mathrm{e}\, v_\mathrm{th} \int_0^\infty \mathrm{d}u \left[u f^{\mathrm{C}}_{\mathrm{f,e}}[u]\right] = N_\mathrm{e}\, v_\mathrm{th} \int_0^\infty \mathrm{d}\epsilon \left[f^{\mathrm{C}}_{\mathrm{f,e}}[\epsilon]\right]. \tag{6.20}$$

The differential electron flux follows by derivation, i.e., $j^*[W] = {}^{\mathrm{d}\Phi}\!/_{\mathrm{d}W}$. If Eq. (6.20) is used, the differential flux

$$j^* = \frac{\mathrm{d}\Phi}{\mathrm{d}W} = \frac{\partial \Phi}{\partial \epsilon}\frac{\mathrm{d}\epsilon}{\mathrm{d}W} \tag{6.21}$$

$$= \frac{N_\mathrm{e} v_\mathrm{th}}{k_\mathrm{B}T} f^{\mathrm{C}}_{\mathrm{f,e}}[\epsilon] = \frac{N_\mathrm{e}}{\sqrt{m_\mathrm{e} k_\mathrm{B} T}} f^{\mathrm{C}}_{\mathrm{f,e}}[\epsilon] = j_{0,\mathrm{class}}\, f^{\mathrm{C}}_{\mathrm{f,e}}[\epsilon] \tag{6.22}$$

can be found. Here $j_{0,\mathrm{class}} = {}^{(N_{\mathrm{e},0} v_\mathrm{th})}\!/_{(k_\mathrm{B}T)}$ is used and the constant $N_{\mathrm{e},0} = N_\mathrm{e}$ is chosen.

In order to determine the electron flux for the accelerated electrons (case $u_0 > u_\mathrm{D}$) Eq. (6.19) is inserted in Eq. (6.22)

$$\frac{j^*_\mathrm{f}}{j_{0,\mathrm{class}}} = \frac{\mathcal{H}_0\left[\epsilon_\mathrm{f} - \epsilon_{a_\mathrm{acc}}\left(1 - \frac{x_0}{L_\mathrm{loop}}\right) - \epsilon_\mathrm{D}\right]}{\sqrt{2\pi}} \exp\left[-\left(\epsilon_\mathrm{f} - \epsilon_{a_\mathrm{acc}}\left(1 - \frac{x_0}{L_\mathrm{loop}}\right)\right)\right]. \tag{6.23}$$

Considering the plasma tube to have a constant cross section A_tube, and being filled with an electron-proton plasma, the differential electron flux along the whole plasma tube j_f can be determined, using the substitution $x_\Delta = 1 - s = 1 - {}^{x_0}\!/_{L_\mathrm{loop}}$, i.e.,

$$\frac{j_\mathrm{f}}{j_{0,\mathrm{class}}} = \frac{1}{L_\mathrm{loop}} \int_0^{L_\mathrm{loop}} \mathrm{d}x_0 \left[\frac{j^*_\mathrm{f}\, A_\mathrm{tube}}{j_{0,\mathrm{class}}}\right] = \int_0^1 \mathrm{d}x_\Delta \left[\frac{j^*_\mathrm{f}\, A_\mathrm{tube}}{j_{0,\mathrm{class}}}\right] \tag{6.24}$$

$$= \frac{1}{\sqrt{2\pi}} \int_0^1 \mathrm{d}x_\Delta \Big[A_\mathrm{tube}\, \mathcal{H}_0\left[\epsilon_\mathrm{f} - \epsilon_{a_\mathrm{acc}} x_\Delta - \epsilon_\mathrm{D}\right] \exp\left[-\left(\epsilon_\mathrm{f} - \epsilon_{a_\mathrm{acc}} x_\Delta\right)\right]\Big]. \tag{6.25}$$

Due to the Heaviside step function the integral in Eq. (6.25) gives a contribution only for $\epsilon_\mathrm{f} - \epsilon_{a_\mathrm{acc}} x_\Delta - \epsilon_\mathrm{D} > 0$, i.e., $(\epsilon_\mathrm{f}-\epsilon_\mathrm{D})/\epsilon_{a_\mathrm{acc}} > x_\Delta$. In the case of $(\epsilon_\mathrm{f}-\epsilon_\mathrm{D})/\epsilon_{a_\mathrm{acc}} < 1$ the integrand is non-zero within the boundaries from 0 to $(\epsilon_\mathrm{f}-\epsilon_\mathrm{D})/\epsilon_{a_\mathrm{acc}}$. Hence if A_tube is constant,

$$\begin{aligned}\frac{j_\mathrm{f}}{j_{0,\mathrm{class}} A_\mathrm{tube}} &= \frac{\exp[-\epsilon_\mathrm{f}]}{\sqrt{2\pi}} \int_0^{(\epsilon_\mathrm{f}-\epsilon_\mathrm{D})/\epsilon_{a_\mathrm{acc}}} \mathrm{d}x_\Delta \Big[\exp[\epsilon_{a_\mathrm{acc}} x_\Delta]\Big] \\ &= \frac{1}{\sqrt{2\pi}} \frac{1}{\epsilon_{a_\mathrm{acc}}} \Big(\exp[-\epsilon_\mathrm{D}] - \exp[-\epsilon_\mathrm{f}]\Big) \end{aligned} \tag{6.26}$$

is obtained. On the other hand, the case of $(\epsilon_\mathrm{f}-\epsilon_\mathrm{D})/\epsilon_{a_\mathrm{acc}} > 1$ leads to

$$\begin{aligned}\frac{j_\mathrm{f}}{j_{0,\mathrm{class}} A_\mathrm{tube}} &= \frac{\exp[-\epsilon_\mathrm{f}]}{\sqrt{2\pi}} \int_0^{1} \mathrm{d}x_\Delta \Big[\exp[\epsilon_{a_\mathrm{acc}} x_\Delta]\Big] \\ &= \frac{1}{\sqrt{2\pi}} \frac{\exp[-\epsilon_\mathrm{f}]}{\epsilon_{a_\mathrm{acc}}} \Big(\exp[\epsilon_{a_\mathrm{acc}}] - 1\Big), \end{aligned} \tag{6.27}$$

whereas the case $(\epsilon_\mathrm{f}-\epsilon_\mathrm{D})/\epsilon_{a_\mathrm{acc}} = 1$ gives no contribution at all.

Summarising these results the piecewise defined electron flux

$$\frac{j_\mathrm{f}}{j_{0,\mathrm{class}}} = \frac{A_\mathrm{tube}}{\sqrt{2\pi}} \begin{cases} \exp[-\epsilon_\mathrm{f}] & \text{for} \quad \epsilon_\mathrm{f} \le \epsilon_\mathrm{D} \\ \frac{1}{\epsilon_{a_\mathrm{acc}}}\Big(\exp[-\epsilon_\mathrm{D}] - \exp[-\epsilon_\mathrm{f}]\Big) & \text{for} \quad (\epsilon_\mathrm{f} > \epsilon_\mathrm{D}) \wedge ((\epsilon_\mathrm{f}-\epsilon_\mathrm{D})/\epsilon_{a_\mathrm{acc}} < 1) \\ 0 & \text{for} \quad (\epsilon_\mathrm{f} > \epsilon_\mathrm{D}) \wedge ((\epsilon_\mathrm{f}-\epsilon_\mathrm{D})/\epsilon_{a_\mathrm{acc}} = 1) \\ \frac{\exp[-\epsilon_\mathrm{f}]}{\epsilon_{a_\mathrm{acc}}}\Big(\exp[\epsilon_{a_\mathrm{acc}}] - 1\Big) & \text{for} \quad (\epsilon_\mathrm{f} > \epsilon_\mathrm{D}) \wedge ((\epsilon_\mathrm{f}-\epsilon_\mathrm{D})/\epsilon_{a_\mathrm{acc}} > 1) \end{cases} \tag{6.28}$$

is obtained. This equation describes the electron flux for the non-relativistic electrons accelerated by a constant electric field along a magnetic flux tube filled with an electron-proton plasma. However it covers only the classical electron acceleration neglecting relativistic effects. The relativistic electron flux is discussed in Sect. 6.1.3.

But before the relativistic flux is calculated, the obtained result is applied on an inhomogeneously filled plasma tube, i.e., due to the solar gravity N_e depends on x (see Sect. 4.2). Additionally the most general case is assumed, meaning that the tube is considered to vary in its cross sectional area, i.e., A_tube is dependent on x. In order to demonstrate the proceeding and to be able to treat the problem in an easy numerical way, N_e, ϵ_D, and A_tube are considered to be defined piecewise by simple functions of the following kind

$$N_\mathrm{e}[x_\Delta] = N_{\mathrm{e},0} \begin{cases} \mathcal{K}_{N_{\mathrm{e},1}} & \text{for} \quad s_{1,\mathrm{l}} = 0.0 \le x_\Delta < s_{1,\mathrm{u}} \\ \mathcal{K}_{N_{\mathrm{e},2}} & \text{for} \quad s_{2,\mathrm{l}} \le x_\Delta < s_{2,\mathrm{u}} \\ \mathcal{K}_{N_{\mathrm{e},i}} & \text{for} \quad s_{i,\mathrm{l}} \le x_\Delta < s_{i,\mathrm{u}} \\ \quad\vdots & \\ \mathcal{K}_{N_{\mathrm{e},n}} & \text{for} \quad s_{n,\mathrm{l}} \le x_\Delta \le 1.0 = s_{n,\mathrm{u}} \end{cases} \tag{6.29}$$

$$\epsilon_\mathrm{D}[x_\Delta] = \begin{cases} \epsilon_{\mathrm{D},1} & \text{for} \quad s_{1,\mathrm{l}} = 0.0 \le x_\Delta < s_{1,\mathrm{u}} \\ \epsilon_{\mathrm{D},2} & \text{for} \quad s_{2,\mathrm{l}} \le x_\Delta < s_{2,\mathrm{u}} \\ \epsilon_{\mathrm{D},i} & \text{for} \quad s_{i,\mathrm{l}} \le x_\Delta < s_{i,\mathrm{u}} \\ \vdots & \\ \epsilon_{\mathrm{D},n} & \text{for} \quad s_{n,\mathrm{l}} \le x_\Delta \le 1.0 = s_{n,\mathrm{u}} \end{cases} \tag{6.30}$$

$$A_\mathrm{tube}[x_\Delta] = \begin{cases} A_{\mathrm{tube},1} & \text{for} \quad s_{1,\mathrm{l}} = 0.0 \le x_\Delta < s_{1,\mathrm{u}} \\ A_{\mathrm{tube},2} & \text{for} \quad s_{2,\mathrm{l}} \le x_\Delta < s_{2,\mathrm{u}} \\ A_{\mathrm{tube},i} & \text{for} \quad s_{i,\mathrm{l}} \le x_\Delta < s_{i,\mathrm{u}} \\ \quad\vdots & \\ A_{\mathrm{tube},n} & \text{for} \quad s_{n,\mathrm{l}} \le x_\Delta \le 1.0 = s_{n,\mathrm{u}} \end{cases} , \tag{6.31}$$

respectively. From this paragraph on $N_{\mathrm{e},0}$ is chosen to be the absolute minimum of the density function along the plasma tube.

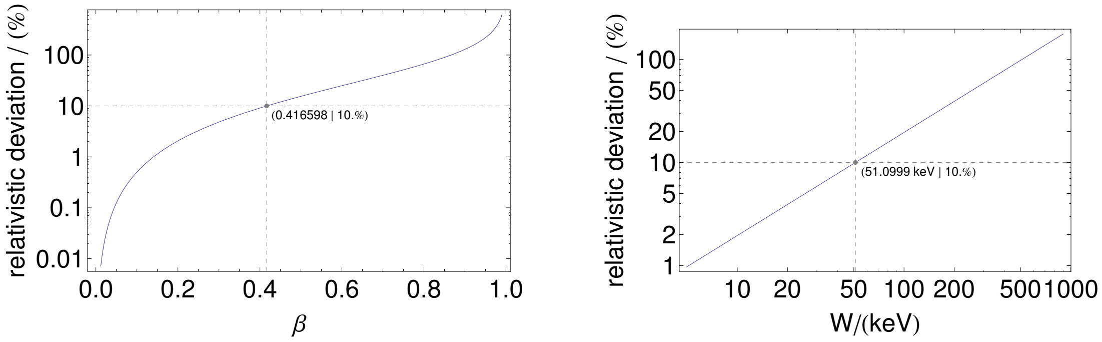

(a) The relativistic deviation is shown in dependence on the electron's velocity, which is normalised to the speed of light.

(b) The relativistic deviation is shown in dependence on the electron's kinetic energy.

Figure 6.5: The figures present the deviation of the classical equations of motion from the relativistic ones.

Hence the non-accelerated contribution of the electron flux is given by

$$j_{\mathrm{f}}^{\mathrm{nonacc}}[\epsilon] \quad = \quad \frac{j_{0,\mathrm{class}}}{\sqrt{2\pi}} \sum_{i=1}^{n} \left[\mathcal{K}_{N_{\mathrm{e}},i} A_{\mathrm{tube},i}\, \mathcal{H}_0[\epsilon_{\mathrm{D},i} - \epsilon]\; (s_{i,\mathrm{u}} - s_{i,\mathrm{l}})\right] \exp\left[-\epsilon\right], \tag{6.32}$$

whereas the accelerated part of the electron flux is obtained by means of Eq. (6.25), i.e.,

$$\begin{aligned} j_{\mathrm{f}}^{\mathrm{acc}}[\epsilon] \quad = \quad & \frac{j_{0,\mathrm{class}}}{\sqrt{2\pi}} \sum_{i=1}^{n} \Bigg[\mathcal{K}_{N_{\mathrm{e}},i} A_{\mathrm{tube},i} \\ & \cdot \int_{s_{1,\mathrm{l}}}^{s_{n,\mathrm{u}}} \mathrm{d}x_\Delta \Big[\mathcal{H}_0\left[\epsilon - \epsilon_{\mathrm{D},i} - \epsilon_{a_{\mathrm{acc}}} x_\Delta\right] \exp\left[-\left(\epsilon - \epsilon_{a_{\mathrm{acc}}} x_\Delta\right)\right]\Big]\Bigg]. \end{aligned} \tag{6.33}$$

These two (non-relativistic) equations allow to calculate both the non-accelerated and accelerated flux contribution. However these equations need to be modified in order to consider relativistic effects, which become the more important, the higher the kinetic energy of the electrons become. As seen in Fig. 6.5 the deviation due to relativistic effects from the classical Newtonian mechanics for an electron with a kinetic energy of about 51 keV is about 10% (Önel, 2004). Such a small deviation is still acceptable, but whenever electrons become faster, their motion needs to be treated in a relativistic way.

6.1.3 Relativistic approach: Electron flux in a plasma

Instead of the classical Maxwellian electron distribution function from Eq. (6.11), the previously mentioned and in the following introduced relativistic Maxwellian electron distribution function

$$f_{\mathrm{e}}^{\mathrm{R}} \quad = \quad \frac{1}{\mathcal{K}_{\mathrm{Maxwell}}} \exp\left[-\frac{W}{k_{\mathrm{B}} T}\right] \tag{6.34}$$

has to be used. The electron's kinetic energy can be expressed by

$$W \quad = \quad m_{\mathrm{e}} c^2 \left(\gamma - 1\right), \tag{6.35}$$

where

$$\gamma[\beta] \quad = \quad \frac{1}{\sqrt{1 - \beta^2}} \tag{6.36}$$

is the Lorentz factor, which is a function of the electron's velocity V that has been normalised $\beta = V/c$ to the speed of light c.

In the classical case as presented in Sect. 6.1.2 it made sense to normalise all energies to the thermal energy. Hence ϵ was defined by $\epsilon = W/(k_\mathrm{B}T)$. But in the relativistic case it is more convenient to introduce $\epsilon^* = W/(m_\mathrm{e}c^2) = \gamma - 1$, where the energies are normalised to the electron's rest energy. Using the normalised thermal energy $\epsilon^*_\mathrm{th} = (k_\mathrm{B}T)/(m_\mathrm{e}c^2)$ the distribution function from Eq. (6.34) can be rewritten as

$$f_\mathrm{e}^\mathrm{R} \quad = \quad \mathcal{K}_\mathrm{Maxwell} \exp\left[-\frac{\epsilon^*}{\beta_\mathrm{th}^2}\right] = \mathcal{K}_\mathrm{Maxwell} \exp\left[\frac{1-\gamma}{\beta_\mathrm{th}^2}\right]. \tag{6.37}$$

The constant $\mathcal{K}_\mathrm{Maxwell}$ is determined numerically by solving the integral

$$\mathcal{K}_\mathrm{Maxwell} \quad = \quad \left(\int_{-1}^{1} \mathrm{d}\hat{\beta} \left[\exp\left[\frac{1-\gamma[\hat{\beta}]}{\beta_\mathrm{th}^2}\right]\right]\right)^{-1} \tag{6.38}$$

for a given temperature. By choosing the constant like this, f_e^R is normalised to unity.[1]

As already discussed in the classical approach (see Eq. (6.20), pg. 59) the total electron flux along the plasma tube is

$$\Phi \quad = \quad \int_0^c \mathrm{d}V \Big[N_\mathrm{e} V f[V]\Big], \tag{6.39}$$

and the differential flux follows from

$$j^* \quad = \quad \frac{\mathrm{d}\Phi}{\mathrm{d}W} = \frac{\partial\Phi}{\partial\beta}\frac{\mathrm{d}\beta}{\mathrm{d}W} = \frac{\partial\Phi}{\partial V}\frac{\mathrm{d}V}{\mathrm{d}\beta}\frac{\mathrm{d}\beta}{\mathrm{d}W} \tag{6.40}$$

$$\quad = \quad (N_\mathrm{e} f V)\cdot(c)\cdot\left(m_\mathrm{e}c^2\gamma^3\beta\right)^{-1} = \frac{N_\mathrm{e} f}{m_\mathrm{e}\gamma^3} = \frac{N_\mathrm{e} f}{m_\mathrm{e}\left(\epsilon^*+1\right)^3}. \tag{6.41}$$

Introducing $j_{0,\mathrm{relat}} = (N_{\mathrm{e},0}\mathcal{K}_\mathrm{Maxwell})/m_\mathrm{e}$ the fluxes can be obtained analogously to the approach demonstrated in Sect. 6.1.2: The non-accelerated contribution of the electron flux is given by

$$j_\mathrm{f}^\mathrm{nonacc}[\epsilon^*] \quad = \quad \frac{j_{0,\mathrm{relat}}}{\mathcal{K}_\mathrm{Maxwell}} \sum_{i=1}^{n} \left[\mathcal{K}_{N_{\mathrm{e},i}} A_{\mathrm{tube},i}\, \mathcal{H}_0[\epsilon^*_{\mathrm{D},i} - \epsilon^*]\ (s_{i,\mathrm{u}} - s_{i,\mathrm{l}})\right] \frac{f_\mathrm{f,e}^\mathrm{R}[\epsilon^*]}{\left(\epsilon^*+1\right)^3}. \tag{6.42}$$

The contribution made by the accelerated electrons is found to be

$$j_\mathrm{f}^\mathrm{acc}[\epsilon] \quad = \quad \frac{j_{0,\mathrm{relat}}}{\mathcal{K}_\mathrm{Maxwell}} \sum_{i=1}^{n} \Bigg[\mathcal{K}_{N_{\mathrm{e},i}} A_{\mathrm{tube},i} \cdot \int_{s_{1,\mathrm{l}}}^{s_{n,\mathrm{u}}} \mathrm{d}x_\Delta \Big[\mathcal{H}_0\left[\epsilon^* - \epsilon^*_{\mathrm{D},i} - \Delta\epsilon^*\right] \frac{f_\mathrm{f,e}^\mathrm{R}[\epsilon^* - \Delta\epsilon^*]}{\left(\epsilon^*+1\right)^3}\Big]\Bigg], \tag{6.43}$$

where $\Delta\epsilon^*$ is given by the electron's normalised energy gain, i.e., $\Delta\epsilon^* = \Delta W/m_\mathrm{e}c^2 = \frac{(-eEL_\mathrm{loop}x_\Delta)}{(m_\mathrm{e}c^2)}$.

However the *RHESSI* spacecraft observes not $j_\mathrm{f}^\mathrm{acc}$, but the superposition of the accelerated electron flux and the thermal electron flux $j^{RHESSI} = j_\mathrm{f}^\mathrm{acc} + j^\mathrm{th}$. The latter one is obtained from Eq. (6.42) by removing the Heaviside step function, i.e.,

$$j_\mathrm{f}^\mathrm{th}[\epsilon] \quad = \quad \frac{j_{0,\mathrm{relat}}}{\mathcal{K}_\mathrm{Maxwell}} \sum_{i=1}^{n} \left[\mathcal{K}_{N_{\mathrm{e},i}} A_{\mathrm{tube},i}\ (s_{i,\mathrm{u}} - s_{i,\mathrm{l}})\right] \frac{f_\mathrm{f,e}^\mathrm{R}[\epsilon^*]}{\left(\epsilon^*+1\right)^3}. \tag{6.44}$$

An exemplary solution for a typical set of parameters for the Eqs. (6.43) and (6.44) is presented by Fig. 7.4 (pg. 68) and explained in Sect. 7.1. Moreover the electron fluxes obtained from these spectra are discussed for different conditions in Sect. 7.2 (pg. 68 and following).

[1] Condition for normalisation: $\int_{-1}^{1} \mathrm{d}\hat{\beta}\left[f_\mathrm{e}^\mathrm{R}[\hat{\beta}]\right] = 1$.

Part III

Results and discussion

I don't pretend we have all the answers. But the questions are certainly worth thinking about.

– Sir Arthur C. Clarke

CHAPTER 7

Electron fluxes

In Chapter 5 it is explained how the electric field needed for the electron acceleration is modelled by simple electric circuits. Then in Chapter 6 the electron acceleration along a magnetic loop is discussed and the needed expressions of the flux of accelerated electrons are derived. In the current chapter, the influence of the plasma parameters and their influence on the electron acceleration are demonstrated.

7.1 Influence of the plasma parameters

As explained in Sect. 2.2 the temperature in the quite corona is of the order of 1 MK to 2 MK. For instance Mann *et al.* (1999) deduce a coronal temperature of 1.39 MK by comparing a barometric density model with the empirically obtained Newkirk (1961) model. These values are confirmed by observations of spectral lines from the corona. However during a flare the plasma is heated quickly. Holman (1995) proposes a plasma temperature in the order of 8 MK in the early flare phases. *RHESSI* observations indicate plasma temperatures in the order of about 40 MK (Warmuth *et al.*, 2007). Indeed the temperature is a very important parameter for the conditions in the solar corona and during a flare it rises by an order of magnitude. Hence the electron fluxes need to be calculated for different temperatures in the range from about 1 MK to about 40 MK.

In order to determine the electron flux spectra, the total number of present electrons in the coronal loop needs to be known. In a first approximation the number of electrons that are accelerated is directly related to the volume of the coronal loop. As explained in Sect. 4.2 the solar atmosphere is highly structured. Hence an average gravitationally layered, here barometric density model is used, in order to determine the electron number density as a function of the loop height. Additionally the loop cross section needs to be considered. For instance Aschwanden *et al.* (1999); Bourouaine *et al.* (2008) or Chapter 3 in Aschwanden (2006) point out that the loop cross section is not always constant (see the sketch in Fig. 7.2(a)). On the other hand Klimchuk (2000) found by statistical analysis of 43 soft X-ray loops observed by *Yohkoh* that the loop cross section only slightly varies. Therefore in the present thesis both possibilities are discussed. First and in accordance with observations, the magnetic loop's arc length is considered to be $L_{\rm loop} = 110\,\mathrm{Mm}$ and the loop's cross section in the footpoints is chosen to be $A_{\rm s} = 7.85 \times 10^{13}\,\mathrm{m}^2$ and constant (see Sect. 5.2.1). In the second case the loop's cross section at the loop top is deduced from observation. Using the soft X-ray source's diameter from Fig. 3.7(a) (pg. 21), the loop diameter in the corona can be estimated with 23.9 Mm. If s quantifies the loop's to unity normalised arc length, and if the loop is assumed to be symmetric, then the two cross sections at the footpoints $A[s = 0] = A[s = 1] = A_{\rm s}$, and the cross section in the loop top

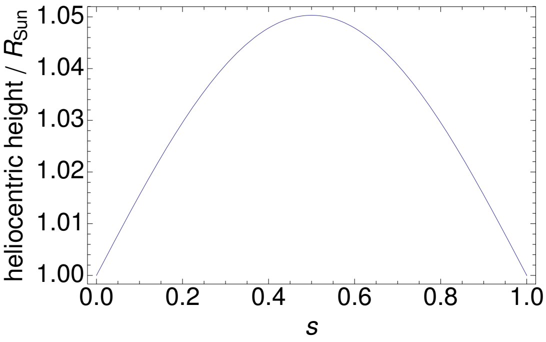

(a) A symmetric coronal loop is seen, i.e. its heliocentric height is plotted in dependence on the loop's normalised arc length. Its total arc length is 110 Mm.

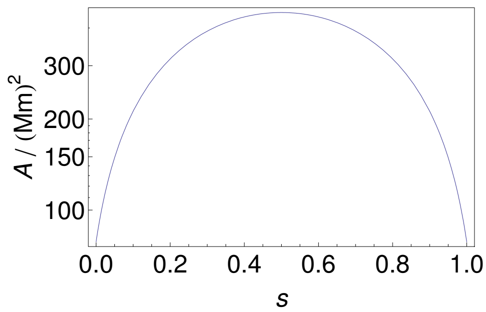

(b) The dependence of the coronal loop's cross section on the loop's normalised arc length, as explained in Eq. 7.1 is illustrated.

Figure 7.1: The diagrams show the cross-section and height in dependence on the normalised arc length of the coronal loop used for the calculations.

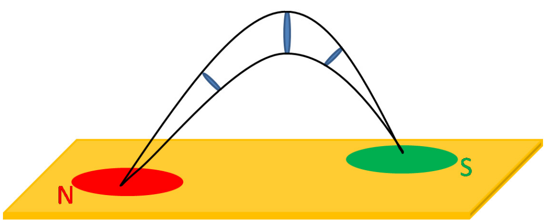

(a) On the yellow photosphere, an active region is located. A plasma tube connecting the regions of different magnetic polarity is illustrated.

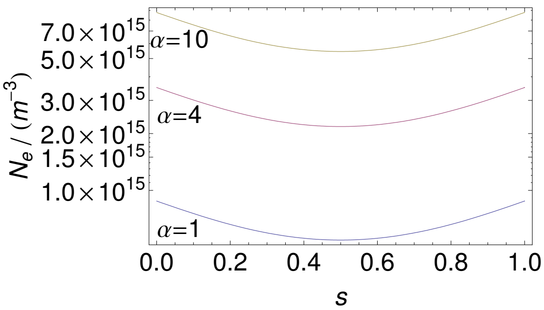

(b) The Newkirk (1961) density in a coronal loop is presented for several Newkirk scaling parameters.

Figure 7.2: A sketch for the cross-section of the coronal loop and a diagram of the electron density therein.

$A[s=0.5] = \left({}^{23.9\,\mathrm{Mm}}/_{2}\right)^2 \pi = 4.50 \times 10^{14}\,\mathrm{m}^2$ are found. If these values are used and a second order polynomial fit is applied on them, a cross section dependency of the loop can be acquired, i.e.,

$$A[s] \quad = \quad -1.49 \times 10^{15}\,\mathrm{m}^2\,s^2 + 1.49 \times 10^{15}\,\mathrm{m}^2\,s + 7.85 \times 10^{13}\,\mathrm{m}^2. \tag{7.1}$$

The values mentioned so far are used for illustrating the numerically obtained results in order to compare them with the observations. As explained (in e.g., Sect. 5.2.1), the special event on October 28, 2003 is employed here, since it is a typical case of a large flare. Consequently, the presented results are not only valid for this special event, but of general interest for solar flare physics.

The Newkirk (1961) density model, as explained in Sect. 4.2 (pg. 26), is applied to the specified coronal loop. As presented in Fig. 7.2(b), the electron density in a loop that is shaped as in Fig. 7.1(a), can be easily calculated in dependence of the Newkirk scaling parameter α.

The electric field is primarily responsible for the acceleration process. Indeed the larger it is and the longer it acts on the electrons in the coronal loop, the higher the final kinetic energy of

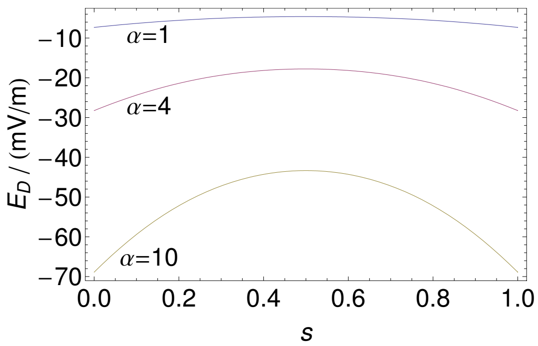

(a) The Dreicer field is presented as a function of the loop's arc length for several different Newkirk scaling parameters and a temperature of $T_0 = 1.39\,\mathrm{MK}$.

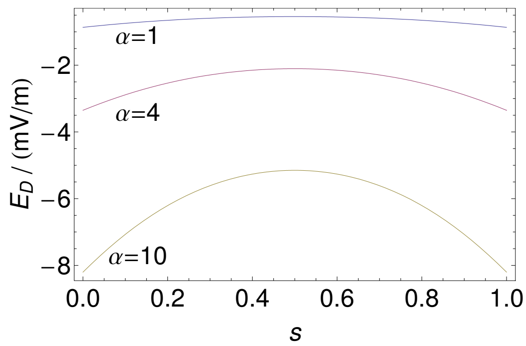

(b) As in Fig. 7.3(a), but for a ten times higher temperature, i.e., $10\,T_0 = 13.9\,\mathrm{MK}$.

Figure 7.3: The diagrams show the Dreicer field as a function of the loop's arc length for several different Newkirk scaling parameters. Each diagram is for a different temperature. The curves are found, if the barometric density model along the isothermal coronal loop is considered.

the accelerated particles becomes. Since the particle number density in the loop varies, the local Dreicer field (E_D) varies too. This means that in those regions where the local particle density is higher, the electric field needed for acceleration needs to be higher as well, in order to accelerate the same number of electrons, as in regions with lower density. The Dreicer field for the chosen loop configuration can be found in Fig. 7.3 for two different temperatures, but several different Newkirk scaling factors α. In the model presented in the thesis at hand, the electric field for the acceleration is given by the negative ratio of the electric voltage drop in the coronal loop, and the coronal loop length. The voltage drop corresponds to the drop in one of the coronal resistors (Fig. 5.4, pg. 35) or to the potential of the coronal capacitor (Fig. 5.7(b), pg. 40), respectively, whenever a magnetic connection is present between the regions of different magnetic polarity through the corona.

If the calculations as presented in Chapter 6 are evaluated for a given set of parameters which are discussed above, a result as presented in Fig. 7.4 is obtained. Therein the differential electron flux j is plotted versus the kinetic energy W of the electrons. Each calculation (for a given set of parameters) leads to two curves, i.e., the accelerated flux (solid curve) calculated by Eq. (6.43) and the thermal flux (dotted curve) calculated by Eq. (6.44), see pg. 62. As explained in Chapter 6, the local temperature, the local loop density and the electric field applied for the electron acceleration determine the critical kinetic energy (which is related to the Dreicer velocity) above which electrons can be accelerated. Therefore the thermal and accelerated components of the flux are equal to each other below this critical energy, but separate from each other above it. The energy gain ΔW (see Eq. (6.12), pg. 58) of the electrons is directly related to the distance they can travel in the loop along the electric field. Therefore the energy the electrons can obtain primarily depends on their initial location (and initial velocity). Hence within Fig. 7.4 the spatial loop extension is represented by the flat solid curve in the interval between the critical energy (related to the Dreicer velocity) and the abrupt cutoff at roughly $-eEL_\mathrm{loop} = 240\,\mathrm{keV}$. The location of this cutoff energy is directly related to the electric field. The higher the field is, the higher the cutoff energy becomes.

Summarising these information the generated electron flux spectra can be understood as following: The longer the distance which the electrons travel along the coronal loop is, the more they can be accelerated by the electric field. Additionally the loop geometry and the electron distribution need to be considered, i.e., there are more electrons at the loop's footpoints, than at the loop's top. If all these effects are considered, the electron flux spectra as presented in Fig. 7.4 are obtained.

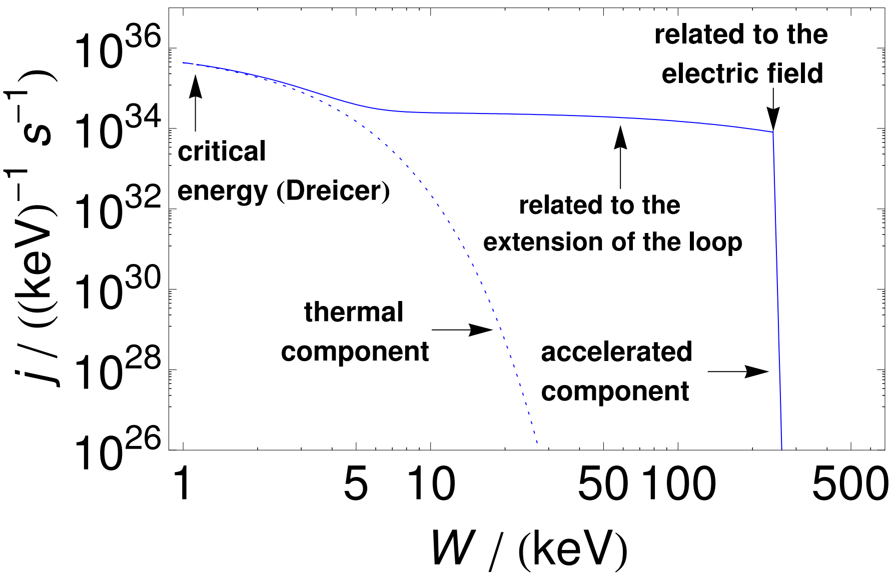

Figure 7.4: For a typical set of parameters, i.e., $T = 13.9\,\mathrm{MK}$, $\alpha = 4$, $E = -2.18\,\mathrm{mV/m}$, and $A[s] = A_\mathrm{s} = 7.85 \times 10^{13}\,\mathrm{m}^2$, a typical numerical result of the electron flux is presented.

7.2 Numerical electron flux calculations

In Sect. 7.1 the conditions in the coronal plasma influencing the form of the electron flux spectra are discussed. In the current section a quantitative discussion is presented by introducing the results of the numerical calculations. Though a large number of electron flux spectra for several different parameters have been calculated, only a few of them are presented in this thesis.

7.2.1 Parameters chosen in the calculation

During all following calculations the magnetic loop along which the electrons are accelerated, is considered to have a length of $L_\mathrm{loop} = 110\,\mathrm{Mm}$. Moreover it is assumed to be constituted by 200 segments of equidistant length, i.e., $n = 200$ in Eqs. (6.29) to (6.31) (pg. 60). The plasma conditions within each of these segments are considered to be constant, depending on the height of the centre of the segment. All subsequently presented calculations refer to the following set of parameters:

$$E_0 = -2.18\,\mathrm{mV/m} \tag{7.2}$$

$$T_0 = 1.39\,\mathrm{MK} \tag{7.3}$$

$$A_0 = A_\mathrm{s} = 7.85 \times 10^{13}\,\mathrm{m}^2 \tag{7.4}$$

These three parameters together with the Newkirk scaling parameter α, make four independent variables in total. Their values determine the look of the electron fluxes as explained in Sect. 7.1. As presented in Table 7.1, all of these parameters are systematically varied in the following. The results of these calculations are presented in the Figs. 7.5 to 7.8 and are discussed next.

Table 7.1: Description of the presented electron flux spectra

Figure	electric field E	temperature T	scaling factor α	cross section A	frictionless energy gain $\Delta W = -eEL_{\text{loop}}$
7.5	E_0	T_0	4	A_0	240 keV
	E_0	$10\,T_0$	4	A_0	240 keV
	E_0	$20\,T_0$	4	A_0	240 keV
	E_0	$28.7\,T_0$	4	A_0	240 keV
7.6	$0.5\,E_0$	$10\,T_0$	4	A_0	120 keV
	E_0	$10\,T_0$	4	A_0	240 keV
	$1.5\,E_0$	$10\,T_0$	4	A_0	360 keV
7.7	E_0	$10\,T_0$	1	A_0	240 keV
	E_0	$10\,T_0$	4	A_0	240 keV
	E_0	$10\,T_0$	10	A_0	240 keV
7.8	E_0	$10\,T_0$	4	A_0	240 keV
	E_0	$10\,T_0$	4	see Eq. (7.1)	240 keV

7.2.2 Discussions and Results

The Figs. 7.5 to 7.8 contain the results of the calculations. In all of these four diagrams several different electron flux spectra are presented. They are all superimposed with the thermal electron flux spectrum (which is always represented by a dotted curve). The basic set of parameters have been varied according to the Table 7.1.

Figure 7.5:

The diagram shows four different results for the electron flux calculations, each for a different temperature, i.e., $T = T_0 = 1.39\,\text{MK}$, $T = 10\,T_0 = 13.9\,\text{MK}$, $T = 20\,T_0 = 27.9\,\text{MK}$, and $T = 28.7\,T_0 = 40.0\,\text{MK}$ represented by the red, blue, green, and brown curves, respectively. As explained before, for each of these fluxes, the thermal electron flux (dotted curves) is presented too.

It can be seen that if the temperature is increased, then due to the following two reasons an higher electron flux for the accelerated electrons is obtained:

1. A higher temperature leads to a higher initial thermal flux, directly leading to higher fluxes for the accelerated electrons.

2. A rising temperature is correlated with a decreasing Dreicer field (see e.g., Fig. 6.2, pg. 55). Therefore the electric field applied for the electron acceleration can accelerate more electrons than in a colder plasma.

Table 7.2 lists the total electron flux and the total electron flux power for energetic ($\geq 20\,\text{keV}$) electrons. If the case with the temperature of $T = 13.9\,\text{MK}$ is compared with *RHESSI* observations, it is found to be fitting best the values described before (see e.g., Sect. 3.2.1 (pg. 20 and following) or the estimation for F_{e} on pg. 57). That case predicts a power of the electron flux in the order of $5.51 \times 10^{22}\,\text{W}$ and is associated with an energetic electron production rate of $3.07 \times 10^{36}\,{}^{1}/_{\text{s}}$.

Figure 7.6:

The diagram shows three different results for the electron flux calculations, each for a different electric field, i.e., $E = 0.5\,E_0 = -1.09\,{}^{\text{mV}}/_{\text{m}}$, $E = 1.0\,E_0 = -2.18\,{}^{\text{mV}}/_{\text{m}}$, and $E = 1.5\,E_0 = -3.27\,{}^{\text{mV}}/_{\text{m}}$ represented by the blue, red, and green curves, respectively. Again the dotted curves present the thermal fluxes for these cases.

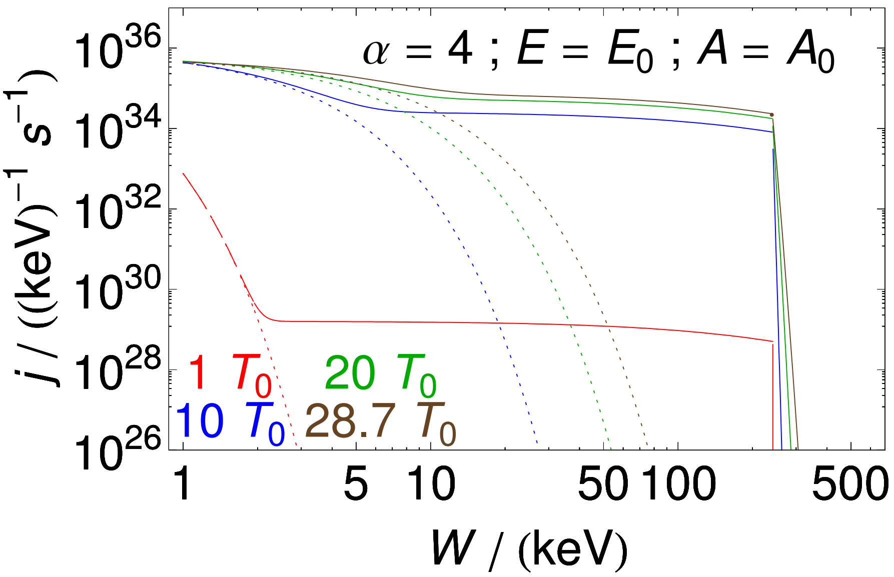

Figure 7.5: The electron flux spectra for several different temperatures $T \in \{T_0, 10\,T_0, 20\,T_0, 28.7\,T_0\}$, but constant electric field $E = E_0$, constant Newkirk parameter $\alpha = 4$, and constant loop cross section $A = A_0$ are presented in dependence upon the energy.

Table 7.2: Total flux and power of the energetic ($\geq 20\,\mathrm{keV}$) electron flux for Fig. 7.5.

temperature T	total energetic electron flux $\int_{20\,\mathrm{keV}}^{\infty} \mathrm{d}W\,[j]$	power of the energetic electron flux $\int_{20\,\mathrm{keV}}^{\infty} \mathrm{d}W\,[W j]$
T_0	1.91×10^{31} 1/s	3.41×10^{17} W
$10\,T_0$	3.07×10^{36} 1/s	5.51×10^{22} W
$20\,T_0$	6.67×10^{36} 1/s	1.19×10^{23} W
$28.7\,T_0$	8.78×10^{36} 1/s	1.58×10^{23} W

As it can be seen, the higher the electric field used for the electron acceleration is, the more electrons are accelerated from the thermal bulk, and the more energy is transferred into the kinetic energy of the electrons. This again is related with the Dreicer field. A higher electric field, is related with a lower Dreicer velocity. Therefore also smaller electron initial velocities are situated in the runaway regime.

In the case of Fig. 7.6 (see Table 7.3) all the total electron fluxes and powers related with them are roughly in the same order of magnitude of 10^{36} 1/s and 10^{22} W, respectively.

Figure 7.7:

The diagram shows three different results for the electron flux calculations, each for a different Newkirk scaling factor, i.e., $\alpha \in \{1, 4, 10\}$, represented by the blue, red, and green curves, respectively. The thermal electron fluxes are represented by the dotted curves.

As it can be seen, a higher Newkirk scaling factor is associated with higher coronal densities. This again (see e.g., Fig. 6.2, pg. 55) leads to an increasing Dreicer field in the coronal plasma.

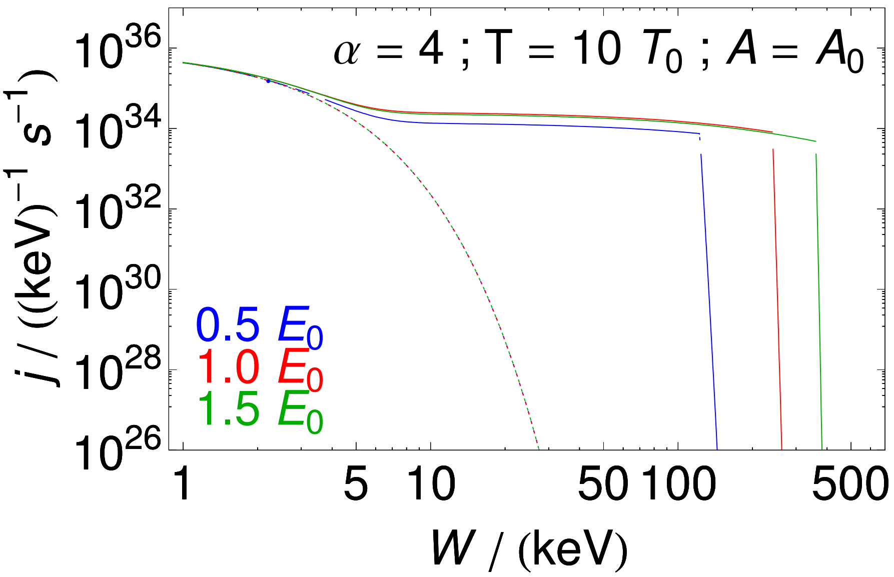

Figure 7.6: As in Fig. 7.5, but with constant temperature $T = 10\,T_0$ and for several different electric fields $E \in \{0.5\,E_0, E_0, 1.5\,E_0\}$.

Table 7.3: Total flux and power of the energetic ($\geq 20\,\text{keV}$) electron flux for Fig. 7.6.

electric field E	total energetic electron flux $\int_{20\,\text{keV}}^{\infty} \mathrm{d}W\,[j]$	power of the energetic electron flux $\int_{20\,\text{keV}}^{\infty} \mathrm{d}W\,[W j]$
$0.5\,E_0$	$1.01 \times 10^{36}\,{}^1\!/\!_\text{s}$	1.08×10^{22} W
$1.0\,E_0$	$3.07 \times 10^{36}\,{}^1\!/\!_\text{s}$	5.51×10^{22} W
$1.5\,E_0$	$3.52 \times 10^{36}\,{}^1\!/\!_\text{s}$	8.44×10^{22} W

Therefore the acceleration is impeded by the increased coronal density. This is why the acceleration sets in at higher energies for higher densities as seen in Fig. 7.7. For all three choices of α the energetic electron flux and power does not differ significantly (see Table 7.4).

Figure 7.8:

The diagram shows two different results for the electron flux calculations, one for a constant cross section $A = A_0$ of the loop, and one for a cross section varying according Eq. (7.1) $A = A[s]$, represented by the red, and blue curves, respectively. Once again the thermal electron flux for these cases is presented with the dotted curves.

As it can be seen in Fig. 7.8, the form of the loop has a huge influence on the flux of the accelerated electrons. In all cases with a constant loop cross section $A = A_0$, the flare spectra has a region with a nearly flat shape. If the cross section varies as discussed here, the flux spectrum of the accelerated electrons has a local minimum and a broad maximum followed by a relatively smooth decay. Furthermore the total flux increases in the case with the varying cross section by roughly an order of magnitude (see Table 7.5).

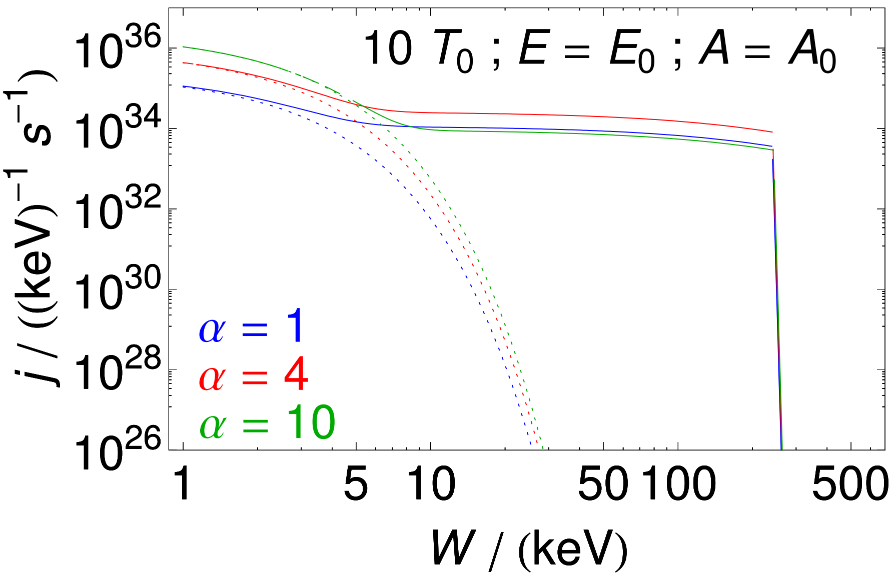

Figure 7.7: As in Fig. 7.5, but with constant temperature $T = 10\,T_0$ and for three different Newkirk parameters $\alpha \in \{1, 4, 10\}$.

Table 7.4: Total flux and power of the energetic ($\geq 20\,\text{keV}$) electron flux for Fig. 7.7.

Newkirk parameter α	total energetic electron flux $\int_{20\,\text{keV}}^{\infty} \mathrm{d}W\,[j]$	power of the energetic electron flux $\int_{20\,\text{keV}}^{\infty} \mathrm{d}W\,[W j]$
1	3.07×10^{36} 1/s	5.51×10^{22} W
4	3.07×10^{36} 1/s	5.51×10^{22} W
10	3.07×10^{36} 1/s	5.51×10^{22} W

7.3 Comparison with observation

So far in this chapter only directly calculated electron fluxes were presented. In the following these fluxes are compared with observations.

As already mentioned a few times throughout this theses, the total electron fluxes (10^{36} 1/s) and powers (10^{22} W) deduced from *RHESSI* observations (see e.g., Warmuth *et al.*, 2007) agree very well with the calculated ones (see tables 7.2 to 7.5). But what about the shape of the calculated fluxes and the observed fluxes? The shape cannot be directly compared, since *RHESSI* can observe only photon flux spectra, whereas the spectra calculated in the thesis are electron flux spectra. Hence an exemplary photon flux *RHESSI* observed during the flare event on October 28, 2003 is converted into an electron spectrum first. Figure 7.10 presents such a non-thermal contribution of the electron flux obtained from *RHESSI* observations.

On the first sight the resemblance with the fluxes calculated in this thesis can be easily recognised: For instance the calculations reproduce the low energy cutoff (critical energy) and the calculated fluxes are of the same order of magnitude as the observed ones.

However when directly compared, the calculated fluxes are too steep, and their high energy

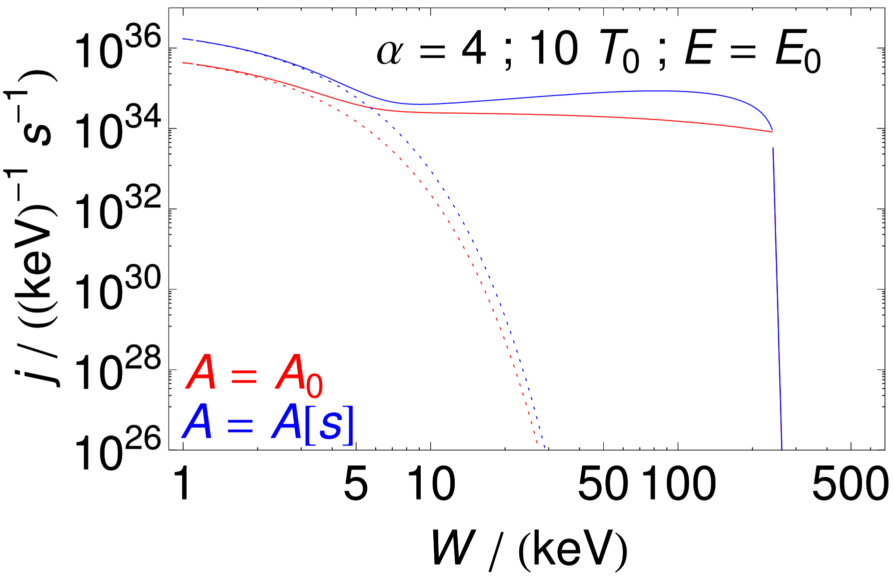

Figure 7.8: As in Fig. 7.5, but with constant temperature $T = 10\,T_0$ and for both a constant cross section $A = A_0$ and a cross section varying according Eq. (7.1).

Table 7.5: Total flux and power of the energetic ($\geq 20\,\mathrm{keV}$) electron flux for Fig. 7.8.

cross section A	total energetic electron flux $\int_{20\,\mathrm{keV}}^{\infty} \mathrm{d}W\,[j]$	power of the energetic electron flux $\int_{20\,\mathrm{keV}}^{\infty} \mathrm{d}W\,[W j]$
A_0	$3.07 \times 10^{36}\,{}^{1}/_{\mathrm{s}}$	$5.51 \times 10^{22}\,\mathrm{W}$
see Eq. (7.1)	$1.35 \times 10^{37}\,{}^{1}/_{\mathrm{s}}$	$2.41 \times 10^{23}\,\mathrm{W}$

cutoffs are too abrupt as well. But beside these few problems, the obtained results fit very well with the observations.

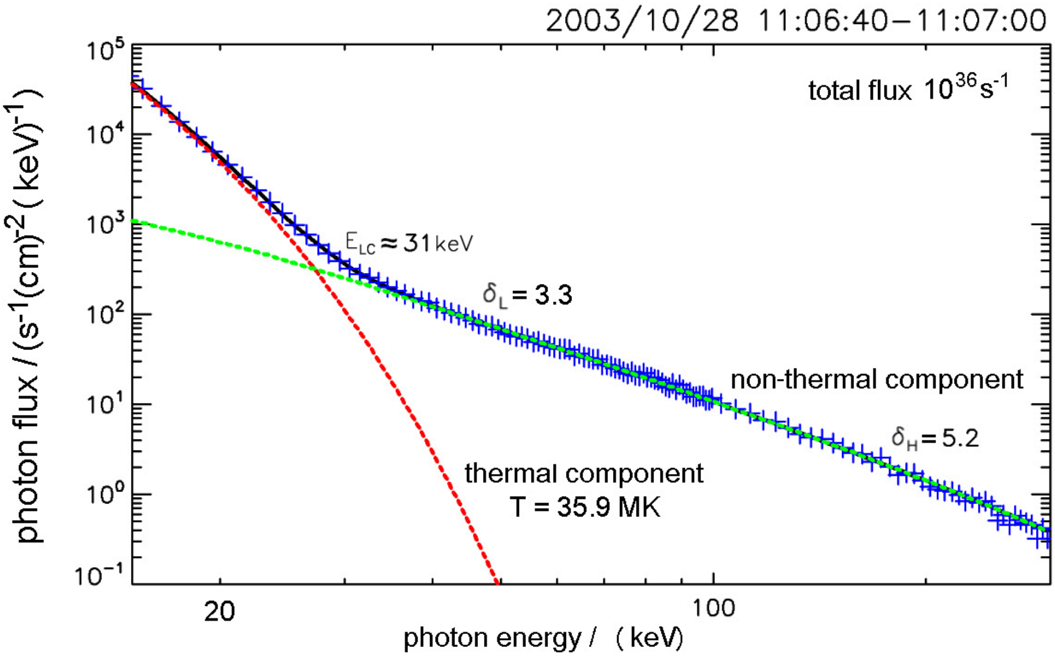

Figure 7.9: The photon spectrum from the October 28, 2003 event is recorded by *RHESSI*. The red curve shows the thermal and the green curve the non-thermal component. The observed photon flux is represented by the solid black line. In Fig. 3.5(b) (pg. 19) such a photon spectrum has already been introduced. (Courtesy of A. Warmuth.)

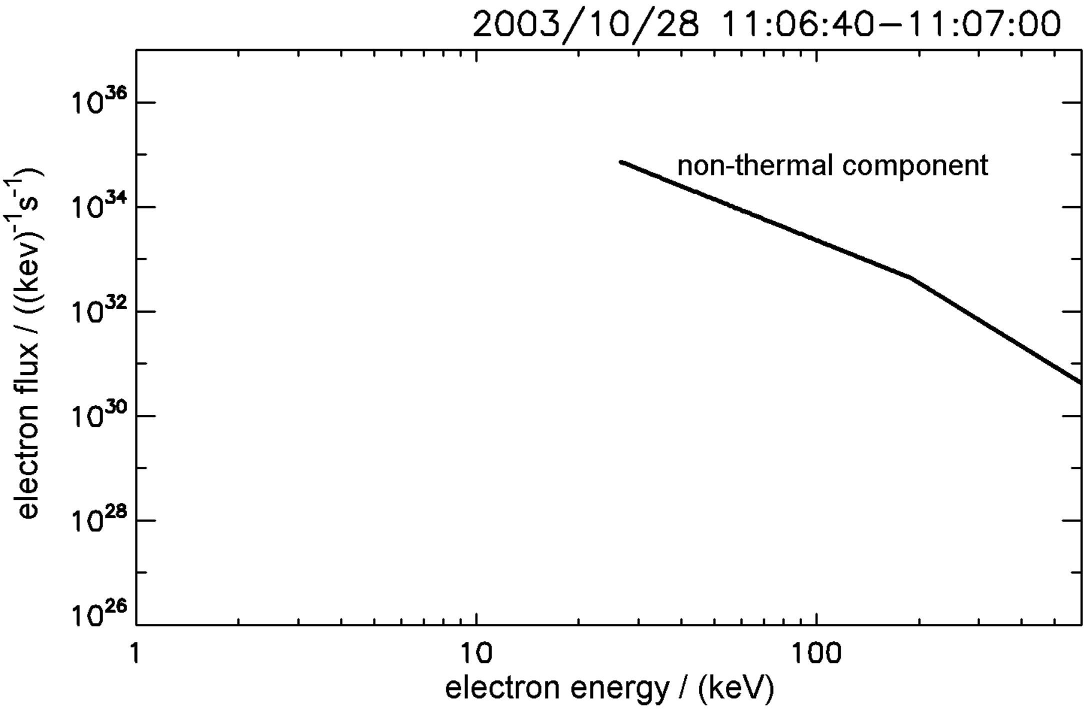

Figure 7.10: The electron spectrum from the October 28, 2003 event is obtained from the *RHESSI* photon spectrum presented in Fig. 7.9. (Courtesy of A. Warmuth.)

CHAPTER 8

Summary and conclusions

Solar flares are sources of energetic electrons as introduced in Chapter 1 to 3. On one hand, basic estimations emphasise the importance of electrons, by employing hard X-ray measurements (e.g., by *RHESSI*), since they carry a substantial part of the energy released during a flare. Typically during a large flare 10^{36} electrons with energies $\geq 20\,\mathrm{keV}$ are generated per second. They are associated with a power of about $10^{22}\,\mathrm{W}$. How so many electrons are accelerated to high energies (i.e., $\geq 20\,\mathrm{keV}$) within fractions of a second is still an open question in solar physics. The answer to this question is not only of interest for solar physics, but of astrophysics in general, since similar processes also happen in other stellar coronae and active galactic nuclei. On the other hand, energetic electrons are also responsible for the non-thermal radio and X-ray radiation of the Sun during flares. Hence they can be observed by remote sensing techniques, e.g., by ground based radioastronomical measurements or space based hard X-ray observations.

As already mentioned in Chapter 3, the flare is widely accepted in the framework of magnetic reconnection: The electrons are accelerated by a different mechanism appearing in the vicinity of reconnection site. However the reconnection model is not able to explain all the details needed for a complete understanding of the electron acceleration during flares. Two of these problems are addressed in this thesis: First, it is still an open question in which way the large number of electrons are delivered from the low density corona to the reconnection site. Second, the electron flux of $10^{36}\,{}^{1}\!/\mathrm{s}$ (as deduced from *RHESSI* measurements) is related to an electric current of about $1.6 \times 10^{17}\,\mathrm{A}$. Such a large current would induce a magnetic flux density strength of the order of $10^{3}\,\mathrm{T} = 10^{7}\,\mathrm{G}$. However such high magnetic fluxes have not been observed so far.

In contrary to the acceleration mechanism acting near the reconnection site, the thesis at hand presents a model, in which the electric field in the corona is generated as a result of the photospheric plasma motion. This means that electric currents can be established in the corona in order to balance out the electric potential differences generated in active regions in the photosphere due to the plasma motion. It is shown that these currents are associated with high electric fields along the coronal magnetic loops and these electric fields are more than sufficient to accelerate the electrons up to relativistic energies in fractions of a second (Sect. 6.1.1).

In order to estimate these electric fields, the coronal flare problem is discussed in terms of electric circuits (Chapter 5). The electric components of the electric circuit are made up by macroscopic electric resistors, inductors, and a capacitor which are carefully chosen according to observations. As presented these circuits allow to determine the electric field strength needed for the electron acceleration. Moreover they predict reasonable time-scales for the flare process and indicate electric current oscillations. The time period of these oscillations agrees with the time periods of hard X-ray pulses (Aschwanden *et al.*, 1995a) and super-short solar radio bursts

(SSS bursts) (Magdalenić, 2007; Magdalenić *et al.*, 2006).

In the next step (Chapter 6) these electric fields are used, to discuss the acceleration of electrons within a plasma tube. The plasma conditions in the tube are chosen in such a way that they correspond to those conditions present in the solar corona. The differential electron flux spectra are numerically calculated in a fully relativistic manner for several different sets of parameters (Chapter 7). The model intrinsically provides two identical counter-streaming currents causing the double nature of the chromospheric hard X-ray sources. Consequently, the magnetic flux density strength, related with these currents, vanishes globally, i.e., the magnetic field strength is much less than 10^3 T in the solar atmosphere. Both of these two issues are in agreement with the observations.

The calculated spectra (Chapter 7) agree roughly with the electron spectrum (Fig. 7.10) deduced from the observed photon spectrum (see Fig. 7.9), i.e., they show a thermal and pronounced non-thermal component. However in the high energy regime, i.e., beyond a few hundreds of keV, the numerically calculated spectra are too steep in comparison with the observations. On the other hand, the resulting flux and power of the energetic electrons is in good agreement with the observations, especially if a high flare temperature (i.e., a few tens of MK) is assumed.

In summary, the presented model agrees with the observations in a quantitative manner and should be regarded as a step toward a better understanding of electron acceleration in solar flares.

In future work, one issue to be addressed might be the time dependency of the stationary electron flux spectra presented in this thesis. Nevertheless this is a big task, since all the coronal plasma conditions are expected to change extremely during a flare.

Part IV

Appendices

If we knew what it was we were doing, it would not be called research, would it?

– Albert Einstein

APPENDIX A

Plasma parameters

The tables A.1 to A.6 present some important plasma parameters. The values listed therein are calculated using the α-fold coronal density model for a plasma composed by electrons, protons and α-particles. They are calculated according to the following equations.

The plasma beta β_{pl} describes the ratio between the thermal gas pressure $p_{\mathrm{co}} = {}^{(N_{\mathrm{e}} k_{\mathrm{B}} T)}/_{\mathcal{K}_2}$ ($\mathcal{K}_2$ represents the ratio of the electron number density N_{e} and the total particle number density N_{total}) and the magnetic pressure $p_{\mathrm{B}} = {}^{B^2}/_{(2\mu_0)}$, i.e.,

$$\beta_{\mathrm{pl}} = \frac{p_{\mathrm{co}}}{p_{\mathrm{B}}}. \tag{A.1}$$

In the case of $\beta_{\mathrm{pl}} > 1$ the magnetic field is considered to be frozen in the plasma, whereas in the opposite case $\beta_{\mathrm{pl}} < 1$ the plasma behaviour is particularly dependent on the magnetic field, which the plasma flow can hardly deform, i.e., the plasma flow mainly follows parallelly the stare field lines.

The electron plasma frequency is given by

$$f_{\mathrm{pl}} = \frac{1}{2\pi}\sqrt{\frac{N_{\mathrm{e}}\, e^2}{\varepsilon_0\, m_{\mathrm{e}}}}, \tag{A.2}$$

when the electron mass m_{e}, elementary charge e, electron number density N_{e}, and the permittivity of free space ε_0 are used.

The electron cyclotron frequency

$$f_{\mathrm{cyc}} = \frac{eB}{{}^{(2\pi m_{\mathrm{e}})}/_{\sqrt{1-(v_{\mathrm{th}}/c)^2}}} \tag{A.3}$$

for an electron of the thermal plasma can be obtained from the equality of the centrifugal force ($F_{\mathrm{centrifugal}} = {}^{m_{\mathrm{e}}\omega_{\mathrm{cyc}} v_{\mathrm{th}}}/_{\sqrt{1-(v_{\mathrm{th}}/c)^2}}$) and the Lorentz force ($F_{\mathrm{Lorentz}} = e v_{\mathrm{th}} B$), when the angular cyclotron frequency $\omega_{\mathrm{cyc}} = 2\pi f_{\mathrm{cyc}}$ is used.

The electron Larmor radius

$$r_{\mathrm{Lamor}} = \frac{v_{\mathrm{th}}}{2\pi f_{\mathrm{cyc}}} \tag{A.4}$$

follows from Eq. (A.3), if $r_{\mathrm{Lamor}} = \omega_{\mathrm{cyc}} v_{\mathrm{th}}$ is taken into account.

The Alfvén velocity $v_{\text{Alfvén}}$ can be written as

$$v_{\text{Alfvén}} = \frac{B}{\sqrt{\mu_0\,\rho_{\text{co}}}}, \tag{A.5}$$

if the coronal mass density $\rho_{\text{co}} = \sum_{\varsigma} N_\varsigma m_\varsigma$ is used.

The Debye length is given by

$$\lambda_{\text{Debye}} = \sqrt{\frac{\varepsilon_0 k_{\text{B}} T}{N_{\text{e}} e^2}},$$

if T is the plasma temperature and N_{e} is the electron number density (Debye & Hückel, 1923a,b,c).

Whenever needed in the following tables the models for the magnetic flux density (presented in Sect. 4.1) and for the coronal density (presented in Sect. 4.2), where the plasma temperature is $T = 1.39 \times 10^6$ K, are used. Under these conditions the thermal electron velocity is $v_{\text{th}} = 4\,596\,{}^{\text{km}}/\text{s}$.

Table A.1: Plasma parameters, obtained using a $\alpha = 1$-fold coronal density model, in the range of $3\,\mathrm{MHz} \lesssim f_{\mathrm{pl}} \lesssim 241\,\mathrm{MHz}$.

f_{pl} in MHz	r in $R_{\odot}$	N_{total} in m^{-3}	N_{e} in m^{-3}	B in T	β_{pl}	$v_{\mathrm{Alfvén}}$ in $\mathrm{m\,s}^{-1}$	f_{cyc} in MHz	r_{Larmor} in m	λ_{Debye} in m
4.	6.4052	3.82×10^{11}	1.98×10^{11}	3.98×10^{-6}	1.1657	1.81×10^{5}	5.99×10^{-8}	1.22×10^{7}	0.1829
11.9	2.6594	3.4×10^{12}	1.77×10^{12}	2.34×10^{-5}	0.3006	3.57×10^{5}	3.52×10^{-7}	2.08×10^{6}	0.0613
19.9	2.0897	9.43×10^{12}	4.9×10^{12}	4.4×10^{-5}	0.236	4.03×10^{5}	6.62×10^{-7}	1.11×10^{6}	0.0368
27.8	1.8312	1.85×10^{13}	9.6×10^{12}	6.6×10^{-5}	0.2051	4.32×10^{5}	9.94×10^{-7}	7.36×10^{5}	0.0263
35.8	1.6762	3.05×10^{13}	1.59×10^{13}	8.99×10^{-5}	0.1825	4.58×10^{5}	1.35×10^{-6}	5.4×10^{5}	0.0205
43.7	1.5701	4.56×10^{13}	2.37×10^{13}	1.16×10^{-4}	0.1633	4.85×10^{5}	1.75×10^{-6}	4.18×10^{5}	0.0167
51.6	1.4915	6.36×10^{13}	3.31×10^{13}	1.45×10^{-4}	0.1461	5.12×10^{5}	2.19×10^{-6}	3.35×10^{5}	0.0142
59.6	1.4302	8.47×10^{13}	4.4×10^{13}	1.77×10^{-4}	0.1304	5.42×10^{5}	2.67×10^{-6}	2.74×10^{5}	0.0123
67.5	1.3805	1.09×10^{14}	5.66×10^{13}	2.13×10^{-4}	0.1159	5.75×10^{5}	3.21×10^{-6}	2.28×10^{5}	0.0108
75.5	1.3392	1.36×10^{14}	7.07×10^{13}	2.53×10^{-4}	0.1025	6.12×10^{5}	3.81×10^{-6}	1.92×10^{5}	0.0097
83.4	1.304	1.66×10^{14}	8.63×10^{13}	2.98×10^{-4}	0.0902	6.52×10^{5}	4.49×10^{-6}	1.63×10^{5}	0.0088
91.4	1.2737	1.99×10^{14}	1.04×10^{14}	3.49×10^{-4}	0.0789	6.97×10^{5}	5.26×10^{-6}	1.39×10^{5}	0.008
99.3	1.2471	2.35×10^{14}	1.22×10^{14}	4.07×10^{-4}	0.0686	7.48×10^{5}	6.13×10^{-6}	1.19×10^{5}	0.0074
107.2	1.2235	2.74×10^{14}	1.43×10^{14}	4.73×10^{-4}	0.0592	8.05×10^{5}	7.13×10^{-6}	1.03×10^{5}	0.0068
115.2	1.2023	3.16×10^{14}	1.65×10^{14}	5.49×10^{-4}	0.0507	8.7×10^{5}	8.27×10^{-6}	8.84×10^{4}	0.0064
123.1	1.1833	3.61×10^{14}	1.88×10^{14}	6.37×10^{-4}	0.043	9.44×10^{5}	9.6×10^{-6}	7.62×10^{4}	0.0059
131.1	1.1659	4.1×10^{14}	2.13×10^{14}	7.4×10^{-4}	0.0362	1.03×10^{6}	1.11×10^{-5}	6.57×10^{4}	0.0056
139.	1.1501	4.61×10^{14}	2.4×10^{14}	8.6×10^{-4}	0.0301	1.13×10^{6}	1.3×10^{-5}	5.65×10^{4}	0.0053
146.9	1.1355	5.15×10^{14}	2.68×10^{14}	$1. \times 10^{-3}$	0.0248	1.24×10^{6}	1.51×10^{-5}	4.84×10^{4}	0.005
154.9	1.122	5.72×10^{14}	2.98×10^{14}	1.17×10^{-3}	0.0201	1.38×10^{6}	1.77×10^{-5}	4.14×10^{4}	0.0047
162.8	1.1095	6.32×10^{14}	3.29×10^{14}	1.38×10^{-3}	0.016	1.55×10^{6}	2.08×10^{-5}	3.52×10^{4}	0.0045
170.8	1.0978	6.95×10^{14}	3.62×10^{14}	1.63×10^{-3}	0.0126	1.75×10^{6}	2.46×10^{-5}	2.97×10^{4}	0.0043
178.7	1.0869	7.62×10^{14}	3.96×10^{14}	1.95×10^{-3}	0.0097	1.99×10^{6}	2.94×10^{-5}	2.49×10^{4}	0.0041
186.6	1.0767	8.31×10^{14}	4.32×10^{14}	2.36×10^{-3}	0.0072	2.3×10^{6}	3.55×10^{-5}	2.06×10^{4}	0.0039
194.6	1.067	9.03×10^{14}	4.7×10^{14}	2.88×10^{-3}	0.0053	2.7×10^{6}	4.34×10^{-5}	1.69×10^{4}	0.0038
202.5	1.058	9.78×10^{14}	5.09×10^{14}	3.58×10^{-3}	0.0037	3.23×10^{6}	5.4×10^{-5}	1.36×10^{4}	0.0036
210.5	1.0494	1.06×10^{15}	5.49×10^{14}	4.56×10^{-3}	0.0025	3.95×10^{6}	6.86×10^{-5}	1.07×10^{4}	0.0035
218.4	1.0412	1.14×10^{15}	5.92×10^{14}	5.97×10^{-3}	0.0015	4.98×10^{6}	8.99×10^{-5}	8.14×10^{3}	0.0033
226.4	1.0335	1.22×10^{15}	6.36×10^{14}	8.15×10^{-3}	0.0009	6.56×10^{6}	1.23×10^{-4}	5.96×10^{3}	0.0032
234.3	1.0262	1.31×10^{15}	6.81×10^{14}	1.18×10^{-2}	0.0005	9.19×10^{6}	1.78×10^{-4}	4.11×10^{3}	0.0031

Table A.2: Plasma parameters, obtained using a $\alpha = 2$-fold coronal density model, in the range of $4\,\mathrm{MHz} \lesssim f_{\mathrm{pl}} \lesssim 341\,\mathrm{MHz}$.

f_{pl} in MHz	r in $R_\odot$	N_{total} in m^{-3}	N_{e} in m^{-3}	B in T	β_{pl}	$v_{\mathrm{Alfvén}}$ in $\mathrm{m\,s}^{-1}$	f_{cyc} in MHz	r_{Larmor} in m	λ_{Debye} in m
5.	7.6159	5.96×10^{11}	3.1×10^{11}	2.94×10^{-6}	3.3399	1.07×10^{5}	4.43×10^{-8}	1.65×10^{7}	0.1463
16.2	2.7171	6.28×10^{12}	3.27×10^{12}	2.22×10^{-5}	0.6152	2.5×10^{5}	3.35×10^{-7}	2.19×10^{6}	0.0451
27.5	2.1107	1.8×10^{13}	9.35×10^{12}	4.27×10^{-5}	0.4767	2.84×10^{5}	6.43×10^{-7}	1.14×10^{6}	0.0266
38.7	1.8426	3.57×10^{13}	1.86×10^{13}	6.46×10^{-5}	0.4132	3.05×10^{5}	9.74×10^{-7}	7.51×10^{5}	0.0189
49.9	1.6836	5.94×10^{13}	3.09×10^{13}	8.85×10^{-5}	0.3674	3.23×10^{5}	1.33×10^{-6}	5.49×10^{5}	0.0147
61.2	1.5754	8.92×10^{13}	4.64×10^{13}	1.15×10^{-4}	0.3287	3.42×10^{5}	1.73×10^{-6}	4.24×10^{5}	0.012
72.4	1.4956	1.25×10^{14}	6.5×10^{13}	1.43×10^{-4}	0.2942	3.61×10^{5}	2.16×10^{-6}	3.39×10^{5}	0.0101
83.6	1.4334	1.67×10^{14}	8.67×10^{13}	1.75×10^{-4}	0.2625	3.82×10^{5}	2.64×10^{-6}	2.77×10^{5}	0.0087
94.8	1.3831	2.15×10^{14}	1.12×10^{14}	2.11×10^{-4}	0.2334	4.05×10^{5}	3.18×10^{-6}	2.3×10^{5}	0.0077
106.1	1.3414	2.68×10^{14}	1.4×10^{14}	2.51×10^{-4}	0.2066	4.31×10^{5}	3.77×10^{-6}	1.94×10^{5}	0.0069
117.3	1.306	3.28×10^{14}	1.71×10^{14}	2.95×10^{-4}	0.1818	4.59×10^{5}	4.45×10^{-6}	1.64×10^{5}	0.0062
128.5	1.2753	3.94×10^{14}	2.05×10^{14}	3.46×10^{-4}	0.1591	4.91×10^{5}	5.21×10^{-6}	1.4×10^{5}	0.0057
139.8	1.2485	4.66×10^{14}	2.42×10^{14}	4.04×10^{-4}	0.1383	5.27×10^{5}	6.08×10^{-6}	1.2×10^{5}	0.0052
151.	1.2248	5.44×10^{14}	2.83×10^{14}	4.69×10^{-4}	0.1194	5.67×10^{5}	7.07×10^{-6}	1.04×10^{5}	0.0048
162.2	1.2035	6.28×10^{14}	3.26×10^{14}	5.45×10^{-4}	0.1023	6.12×10^{5}	8.2×10^{-6}	8.92×10^{4}	0.0045
173.5	1.1843	7.17×10^{14}	3.73×10^{14}	6.32×10^{-4}	0.0869	6.64×10^{5}	9.52×10^{-6}	7.69×10^{4}	0.0042
184.7	1.1669	8.13×10^{14}	4.23×10^{14}	7.33×10^{-4}	0.0731	7.24×10^{5}	1.1×10^{-5}	6.62×10^{4}	0.004
195.9	1.1509	9.15×10^{14}	4.76×10^{14}	8.53×10^{-4}	0.0609	7.94×10^{5}	1.28×10^{-5}	5.7×10^{4}	0.0037
207.1	1.1363	1.02×10^{15}	5.32×10^{14}	9.94×10^{-4}	0.0501	8.75×10^{5}	1.5×10^{-5}	4.89×10^{4}	0.0035
218.4	1.1227	1.14×10^{15}	5.92×10^{14}	1.16×10^{-3}	0.0407	9.71×10^{5}	1.75×10^{-5}	4.18×10^{4}	0.0033
229.6	1.1102	1.26×10^{15}	6.54×10^{14}	1.37×10^{-3}	0.0325	1.09×10^{6}	2.06×10^{-5}	3.55×10^{4}	0.0032
240.8	1.0985	1.38×10^{15}	7.19×10^{14}	1.62×10^{-3}	0.0255	1.23×10^{6}	2.44×10^{-5}	$3. \times 10^{4}$	0.003
252.1	1.0875	1.52×10^{15}	7.88×10^{14}	1.93×10^{-3}	0.0197	1.4×10^{6}	2.91×10^{-5}	2.52×10^{4}	0.0029
263.3	1.0773	1.65×10^{15}	8.6×10^{14}	2.33×10^{-3}	0.0147	1.61×10^{6}	3.51×10^{-5}	2.09×10^{4}	0.0028
274.5	1.0676	1.8×10^{15}	9.35×10^{14}	2.85×10^{-3}	0.0107	1.89×10^{6}	4.28×10^{-5}	1.71×10^{4}	0.0027
285.8	1.0585	1.95×10^{15}	1.01×10^{15}	3.54×10^{-3}	0.0075	2.26×10^{6}	5.32×10^{-5}	1.37×10^{4}	0.0026
297.	1.0499	2.1×10^{15}	1.09×10^{15}	4.49×10^{-3}	0.005	2.76×10^{6}	6.76×10^{-5}	1.08×10^{4}	0.0025
308.2	1.0417	2.27×10^{15}	1.18×10^{15}	5.87×10^{-3}	0.0032	3.47×10^{6}	8.84×10^{-5}	8.28×10^{3}	0.0024
319.5	1.034	2.43×10^{15}	1.27×10^{15}	7.99×10^{-3}	0.0018	4.56×10^{6}	1.2×10^{-4}	6.08×10^{3}	0.0023
330.7	1.0266	2.61×10^{15}	1.36×10^{15}	1.15×10^{-2}	0.0009	6.36×10^{6}	1.74×10^{-4}	4.21×10^{3}	0.0022

Table A.3: Plasma parameters, obtained using a $\alpha = 4$-fold coronal density model, in the range of 6 MHz $\lesssim f_{\mathrm{pl}} \lesssim$ 483 MHz.

f_{pl} in MHz	r in $R_\odot$	N_{total} in m^{-3}	N_{e} in m^{-3}	B in T	β_{pl}	$v_{\mathrm{Alfvén}}$ in $\mathrm{m\,s}^{-1}$	f_{cyc} in MHz	r_{Larmor} in m	λ_{Debye} in m
7.	7.7355	1.17×10^{12}	6.08×10^{11}	2.86×10^{-6}	6.9079	7.45×10^{4}	4.31×10^{-8}	1.7×10^{7}	0.1045
22.9	2.7217	1.25×10^{13}	6.49×10^{12}	2.21×10^{-5}	1.2328	1.76×10^{5}	3.33×10^{-7}	2.19×10^{6}	0.032
38.8	2.1123	3.58×10^{13}	1.86×10^{13}	4.26×10^{-5}	0.9541	$2. \times 10^{5}$	6.42×10^{-7}	1.14×10^{6}	0.0189
54.6	1.8435	7.12×10^{13}	3.7×10^{13}	6.45×10^{-5}	0.8268	2.15×10^{5}	9.72×10^{-7}	7.53×10^{5}	0.0134
70.5	1.6842	1.19×10^{14}	6.17×10^{13}	8.83×10^{-5}	0.7351	2.28×10^{5}	1.33×10^{-6}	5.5×10^{5}	0.0104
86.4	1.5758	1.78×10^{14}	9.26×10^{13}	1.14×10^{-4}	0.6578	2.41×10^{5}	1.72×10^{-6}	4.24×10^{5}	0.0085
102.3	1.4959	2.5×10^{14}	1.3×10^{14}	1.43×10^{-4}	0.5886	2.55×10^{5}	2.16×10^{-6}	3.39×10^{5}	0.0072
118.2	1.4336	3.33×10^{14}	1.73×10^{14}	1.75×10^{-4}	0.5254	2.7×10^{5}	2.64×10^{-6}	2.77×10^{5}	0.0062
134.1	1.3834	4.29×10^{14}	2.23×10^{14}	2.11×10^{-4}	0.4671	2.87×10^{5}	3.17×10^{-6}	2.31×10^{5}	0.0055
149.9	1.3416	5.36×10^{14}	2.79×10^{14}	2.5×10^{-4}	0.4134	3.05×10^{5}	3.77×10^{-6}	1.94×10^{5}	0.0049
165.8	1.3061	6.56×10^{14}	3.41×10^{14}	2.95×10^{-4}	0.3638	3.25×10^{5}	4.45×10^{-6}	1.65×10^{5}	0.0044
181.7	1.2755	7.87×10^{14}	4.1×10^{14}	3.46×10^{-4}	0.3184	3.47×10^{5}	5.21×10^{-6}	1.4×10^{5}	0.004
197.6	1.2486	9.31×10^{14}	4.84×10^{14}	4.03×10^{-4}	0.2768	3.72×10^{5}	6.07×10^{-6}	1.2×10^{5}	0.0037
213.5	1.2249	1.09×10^{15}	5.65×10^{14}	4.69×10^{-4}	0.239	4.01×10^{5}	7.06×10^{-6}	1.04×10^{5}	0.0034
229.4	1.2036	1.25×10^{15}	6.52×10^{14}	5.44×10^{-4}	0.2048	4.33×10^{5}	8.2×10^{-6}	8.92×10^{4}	0.0032
245.2	1.1844	1.43×10^{15}	7.46×10^{14}	6.31×10^{-4}	0.174	4.7×10^{5}	9.51×10^{-6}	7.69×10^{4}	0.003
261.1	1.167	1.63×10^{15}	8.46×10^{14}	7.33×10^{-4}	0.1464	5.12×10^{5}	1.1×10^{-5}	6.63×10^{4}	0.0028
277.	1.151	1.83×10^{15}	9.52×10^{14}	8.52×10^{-4}	0.1219	5.61×10^{5}	1.28×10^{-5}	5.7×10^{4}	0.0026
292.9	1.1363	2.05×10^{15}	1.06×10^{15}	9.93×10^{-4}	0.1003	6.18×10^{5}	1.5×10^{-5}	4.89×10^{4}	0.0025
308.8	1.1228	2.27×10^{15}	1.18×10^{15}	1.16×10^{-3}	0.0815	6.86×10^{5}	1.75×10^{-5}	4.18×10^{4}	0.0024
324.6	1.1102	2.51×10^{15}	1.31×10^{15}	1.37×10^{-3}	0.0651	7.67×10^{5}	2.06×10^{-5}	3.56×10^{4}	0.0023
340.5	1.0985	2.77×10^{15}	1.44×10^{15}	1.62×10^{-3}	0.0512	8.66×10^{5}	2.44×10^{-5}	$3. \times 10^{4}$	0.0021
356.4	1.0876	3.03×10^{15}	1.58×10^{15}	1.93×10^{-3}	0.0394	9.87×10^{5}	2.91×10^{-5}	2.52×10^{4}	0.0021
372.3	1.0773	3.31×10^{15}	1.72×10^{15}	2.33×10^{-3}	0.0295	1.14×10^{6}	3.5×10^{-5}	2.09×10^{4}	0.002
388.2	1.0676	3.59×10^{15}	1.87×10^{15}	2.84×10^{-3}	0.0215	1.34×10^{6}	4.28×10^{-5}	1.71×10^{4}	0.0019
404.1	1.0585	3.89×10^{15}	2.03×10^{15}	3.53×10^{-3}	0.0151	1.59×10^{6}	5.32×10^{-5}	1.38×10^{4}	0.0018
419.9	1.0499	4.21×10^{15}	2.19×10^{15}	4.48×10^{-3}	0.0101	1.95×10^{6}	6.75×10^{-5}	1.08×10^{4}	0.0017
435.8	1.0417	4.53×10^{15}	2.36×10^{15}	5.86×10^{-3}	0.0064	2.45×10^{6}	8.83×10^{-5}	8.29×10^{3}	0.0017
451.7	1.034	4.87×10^{15}	2.53×10^{15}	7.98×10^{-3}	0.0037	3.22×10^{6}	1.2×10^{-4}	6.09×10^{3}	0.0016
467.6	1.0266	5.21×10^{15}	2.71×10^{15}	1.15×10^{-2}	0.0019	4.49×10^{6}	1.73×10^{-4}	4.22×10^{3}	0.0016

Table A.4: Plasma parameters, obtained using a $\alpha = 8$-fold coronal density model, in the range of $9\,\mathrm{MHz} \lesssim f_{\mathrm{pl}} \lesssim 682\,\mathrm{MHz}$.

f_{pl} in MHz	r in $R_\odot$	N_{total} in m^{-3}	N_{e} in m^{-3}	B in T	β_{pl}	$v_{\mathrm{Alfvén}}$ in $\mathrm{m\,s}^{-1}$	f_{cyc} in MHz	r_{Larmor} in m	λ_{Debye} in m
9.	9.0809	1.93×10^{12}	$1. \times 10^{12}$	2.18×10^{-6}	19.7199	4.41×10^{4}	3.28×10^{-8}	2.23×10^{7}	0.0813
31.5	2.7643	2.36×10^{13}	1.23×10^{13}	2.13×10^{-5}	2.5078	1.24×10^{5}	3.21×10^{-7}	2.28×10^{6}	0.0233
53.9	2.1273	6.93×10^{13}	3.61×10^{13}	4.18×10^{-5}	1.9216	1.41×10^{5}	6.29×10^{-7}	1.16×10^{6}	0.0136
76.4	1.8515	1.39×10^{14}	7.24×10^{13}	6.36×10^{-5}	1.6619	1.52×10^{5}	9.58×10^{-7}	7.63×10^{5}	0.0096
98.8	1.6894	2.33×10^{14}	1.21×10^{14}	8.74×10^{-5}	1.4768	1.61×10^{5}	1.32×10^{-6}	5.56×10^{5}	0.0074
121.3	1.5795	3.51×10^{14}	1.83×10^{14}	1.13×10^{-4}	1.3214	1.7×10^{5}	1.71×10^{-6}	4.29×10^{5}	0.006
143.8	1.4987	4.93×10^{14}	2.56×10^{14}	1.42×10^{-4}	1.1825	1.8×10^{5}	2.14×10^{-6}	3.42×10^{5}	0.0051
166.2	1.4359	6.59×10^{14}	3.43×10^{14}	1.74×10^{-4}	1.0556	1.91×10^{5}	2.62×10^{-6}	2.8×10^{5}	0.0044
188.7	1.3852	8.49×10^{14}	4.42×10^{14}	2.09×10^{-4}	0.9387	2.02×10^{5}	3.15×10^{-6}	2.32×10^{5}	0.0039
211.1	1.3431	1.06×10^{15}	5.53×10^{14}	2.49×10^{-4}	0.8308	2.15×10^{5}	3.75×10^{-6}	1.95×10^{5}	0.0035
233.6	1.3074	1.3×10^{15}	6.77×10^{14}	2.93×10^{-4}	0.7315	2.29×10^{5}	4.42×10^{-6}	1.66×10^{5}	0.0031
256.1	1.2766	1.56×10^{15}	8.13×10^{14}	3.44×10^{-4}	0.6403	2.45×10^{5}	5.18×10^{-6}	1.41×10^{5}	0.0029
278.5	1.2496	1.85×10^{15}	9.62×10^{14}	4.01×10^{-4}	0.5569	2.62×10^{5}	6.04×10^{-6}	1.21×10^{5}	0.0026
301.	1.2258	2.16×10^{15}	1.12×10^{15}	4.66×10^{-4}	0.4809	2.82×10^{5}	7.02×10^{-6}	1.04×10^{5}	0.0024
323.5	1.2044	2.49×10^{15}	1.3×10^{15}	5.41×10^{-4}	0.4122	3.05×10^{5}	8.15×10^{-6}	8.98×10^{4}	0.0023
345.9	1.1851	2.85×10^{15}	1.48×10^{15}	6.28×10^{-4}	0.3503	3.31×10^{5}	9.45×10^{-6}	7.74×10^{4}	0.0021
368.4	1.1676	3.24×10^{15}	1.68×10^{15}	7.29×10^{-4}	0.2949	3.61×10^{5}	1.1×10^{-5}	6.67×10^{4}	0.002
390.8	1.1516	3.64×10^{15}	1.89×10^{15}	8.47×10^{-4}	0.2457	3.95×10^{5}	1.28×10^{-5}	5.74×10^{4}	0.0019
413.3	1.1369	4.07×10^{15}	2.12×10^{15}	9.87×10^{-4}	0.2023	4.35×10^{5}	1.49×10^{-5}	4.92×10^{4}	0.0018
435.8	1.1233	4.53×10^{15}	2.36×10^{15}	1.15×10^{-3}	0.1643	4.83×10^{5}	1.74×10^{-5}	4.21×10^{4}	0.0017
458.2	1.1107	5.01×10^{15}	2.6×10^{15}	1.36×10^{-3}	0.1315	5.4×10^{5}	2.04×10^{-5}	3.58×10^{4}	0.0016
480.7	1.099	5.51×10^{15}	2.87×10^{15}	1.61×10^{-3}	0.1033	6.09×10^{5}	2.42×10^{-5}	3.02×10^{4}	0.0015
503.1	1.088	6.04×10^{15}	3.14×10^{15}	1.92×10^{-3}	0.0796	6.94×10^{5}	2.88×10^{-5}	2.54×10^{4}	0.0015
525.6	1.0777	6.59×10^{15}	3.43×10^{15}	2.31×10^{-3}	0.0598	8.01×10^{5}	3.48×10^{-5}	2.1×10^{4}	0.0014
548.1	1.068	7.16×10^{15}	3.73×10^{15}	2.82×10^{-3}	0.0436	9.38×10^{5}	4.25×10^{-5}	1.72×10^{4}	0.0013
570.5	1.0589	7.76×10^{15}	4.04×10^{15}	3.5×10^{-3}	0.0307	1.12×10^{6}	5.27×10^{-5}	1.39×10^{4}	0.0013
593.	1.0502	8.39×10^{15}	4.36×10^{15}	4.44×10^{-3}	0.0206	1.37×10^{6}	6.69×10^{-5}	1.09×10^{4}	0.0012
615.4	1.0421	9.03×10^{15}	4.7×10^{15}	5.8×10^{-3}	0.013	1.72×10^{6}	8.73×10^{-5}	8.38×10^{3}	0.0012
637.9	1.0343	9.7×10^{15}	5.05×10^{15}	7.87×10^{-3}	0.0076	2.25×10^{6}	1.19×10^{-4}	6.17×10^{3}	0.0011
660.4	1.0269	1.04×10^{16}	5.41×10^{15}	1.13×10^{-2}	0.0039	3.13×10^{6}	1.71×10^{-4}	4.29×10^{3}	0.0011

Table A.5: Plasma parameters, obtained using a $\alpha = 10$-fold coronal density model, in the range of $10\,\mathrm{MHz} \lesssim f_{\mathrm{pl}} \lesssim 763\,\mathrm{MHz}$.

f_{pl} in MHz	r in $R_\odot$	N_{total} in m^{-3}	N_{e} in m^{-3}	B in T	β_{pl}	$v_{\mathrm{Alfvén}}$ in $\mathrm{m\,s}^{-1}$	f_{cyc} in MHz	r_{Larmor} in m	λ_{Debye} in m
10.	9.1851	2.38×10^{12}	1.24×10^{12}	2.14×10^{-6}	25.2993	3.89×10^{4}	3.22×10^{-8}	2.27×10^{7}	0.0732
35.1	2.767	2.94×10^{13}	1.53×10^{13}	2.13×10^{-5}	3.1382	1.11×10^{5}	3.21×10^{-7}	2.28×10^{6}	0.0208
60.2	2.1282	8.65×10^{13}	4.5×10^{13}	4.17×10^{-5}	2.403	1.26×10^{5}	6.28×10^{-7}	1.16×10^{6}	0.0121
85.3	1.852	1.74×10^{14}	9.03×10^{13}	6.36×10^{-5}	2.078	1.36×10^{5}	9.57×10^{-7}	7.64×10^{5}	0.0086
110.4	1.6897	2.91×10^{14}	1.51×10^{14}	8.73×10^{-5}	1.8466	1.44×10^{5}	1.31×10^{-6}	5.56×10^{5}	0.0066
135.6	1.5798	4.38×10^{14}	2.28×10^{14}	1.13×10^{-4}	1.6521	1.52×10^{5}	1.71×10^{-6}	4.29×10^{5}	0.0054
160.7	1.4989	6.16×10^{14}	3.2×10^{14}	1.42×10^{-4}	1.4785	1.61×10^{5}	2.14×10^{-6}	3.42×10^{5}	0.0046
185.8	1.436	8.23×10^{14}	4.28×10^{14}	1.74×10^{-4}	1.3199	1.7×10^{5}	2.62×10^{-6}	2.8×10^{5}	0.0039
210.9	1.3853	1.06×10^{15}	5.52×10^{14}	2.09×10^{-4}	1.1737	1.81×10^{5}	3.15×10^{-6}	2.32×10^{5}	0.0035
236.	1.3432	1.33×10^{15}	6.91×10^{14}	2.49×10^{-4}	1.0389	1.92×10^{5}	3.75×10^{-6}	1.95×10^{5}	0.0031
261.1	1.3075	1.63×10^{15}	8.46×10^{14}	2.93×10^{-4}	0.9147	2.05×10^{5}	4.42×10^{-6}	1.66×10^{5}	0.0028
286.2	1.2767	1.95×10^{15}	1.02×10^{15}	3.44×10^{-4}	0.8006	2.19×10^{5}	5.17×10^{-6}	1.41×10^{5}	0.0026
311.3	1.2497	2.31×10^{15}	1.2×10^{15}	4.01×10^{-4}	0.6963	2.35×10^{5}	6.03×10^{-6}	1.21×10^{5}	0.0023
336.5	1.2258	2.7×10^{15}	1.4×10^{15}	4.66×10^{-4}	0.6014	2.53×10^{5}	7.02×10^{-6}	1.04×10^{5}	0.0022
361.6	1.2044	3.12×10^{15}	1.62×10^{15}	5.41×10^{-4}	0.5154	2.73×10^{5}	8.15×10^{-6}	8.98×10^{4}	0.002
386.7	1.1852	3.57×10^{15}	1.85×10^{15}	6.27×10^{-4}	0.438	2.96×10^{5}	9.45×10^{-6}	7.74×10^{4}	0.0019
411.8	1.1677	4.04×10^{15}	2.1×10^{15}	7.28×10^{-4}	0.3688	3.22×10^{5}	1.1×10^{-5}	6.67×10^{4}	0.0018
436.9	1.1517	4.55×10^{15}	2.37×10^{15}	8.47×10^{-4}	0.3072	3.53×10^{5}	1.27×10^{-5}	5.74×10^{4}	0.0017
462.	1.1369	5.09×10^{15}	2.65×10^{15}	9.87×10^{-4}	0.2529	3.89×10^{5}	1.49×10^{-5}	4.92×10^{4}	0.0016
487.1	1.1234	5.66×10^{15}	2.94×10^{15}	1.15×10^{-3}	0.2055	4.32×10^{5}	1.74×10^{-5}	4.21×10^{4}	0.0015
512.2	1.1107	6.26×10^{15}	3.25×10^{15}	1.36×10^{-3}	0.1644	4.83×10^{5}	2.04×10^{-5}	3.58×10^{4}	0.0014
537.4	1.099	6.89×10^{15}	3.58×10^{15}	1.61×10^{-3}	0.1293	5.45×10^{5}	2.42×10^{-5}	3.03×10^{4}	0.0014
562.5	1.088	7.54×10^{15}	3.92×10^{15}	1.91×10^{-3}	0.0995	6.21×10^{5}	2.88×10^{-5}	2.54×10^{4}	0.0013
587.6	1.0777	8.23×10^{15}	4.28×10^{15}	2.31×10^{-3}	0.0748	7.16×10^{5}	3.48×10^{-5}	2.1×10^{4}	0.0012
612.7	1.068	8.95×10^{15}	4.66×10^{15}	2.82×10^{-3}	0.0545	8.39×10^{5}	4.24×10^{-5}	1.72×10^{4}	0.0012
637.8	1.0589	9.7×10^{15}	5.05×10^{15}	3.5×10^{-3}	0.0384	$1. \times 10^{6}$	5.27×10^{-5}	1.39×10^{4}	0.0011
662.9	1.0503	1.05×10^{16}	5.45×10^{15}	4.44×10^{-3}	0.0258	1.22×10^{6}	6.68×10^{-5}	1.09×10^{4}	0.0011
688.	1.0421	1.13×10^{16}	5.87×10^{15}	5.79×10^{-3}	0.0163	1.53×10^{6}	8.72×10^{-5}	8.39×10^{3}	0.0011
713.1	1.0343	1.21×10^{16}	6.31×10^{15}	7.87×10^{-3}	0.0095	2.01×10^{6}	1.18×10^{-4}	6.18×10^{3}	0.001
738.2	1.0269	1.3×10^{16}	6.76×10^{15}	1.13×10^{-2}	0.0049	2.8×10^{6}	1.7×10^{-4}	4.29×10^{3}	0.001

Table A.6: Plasma parameters, obtained using a $\alpha = 12$-fold coronal density model, in the range of $10\,\mathrm{MHz} \lesssim f_{\mathrm{pl}} \lesssim 836\,\mathrm{MHz}$.

f_{pl} in MHz	r in $R_\odot$	N_{total} in m^{-3}	N_{e} in m^{-3}	B in T	β_{pl}	$v_{\mathrm{Alfvén}}$ in $\mathrm{m\,s}^{-1}$	f_{cyc} in MHz	r_{Larmor} in m	λ_{Debye} in m
11.	9.1152	2.89×10^{12}	1.5×10^{12}	2.16×10^{-6}	29.8351	3.59×10^{4}	3.26×10^{-8}	2.25×10^{7}	0.0665
38.5	2.7652	3.54×10^{13}	1.84×10^{13}	2.13×10^{-5}	3.7631	1.01×10^{5}	3.21×10^{-7}	2.28×10^{6}	0.019
66.	2.1276	1.04×10^{14}	5.41×10^{13}	4.18×10^{-5}	2.8828	1.15×10^{5}	6.29×10^{-7}	1.16×10^{6}	0.0111
93.5	1.8517	2.09×10^{14}	1.09×10^{14}	6.36×10^{-5}	2.4931	1.24×10^{5}	9.58×10^{-7}	7.64×10^{5}	0.0078
121.	1.6895	3.49×10^{14}	1.82×10^{14}	8.73×10^{-5}	2.2155	1.32×10^{5}	1.32×10^{-6}	5.56×10^{5}	0.006
148.5	1.5796	5.26×10^{14}	2.74×10^{14}	1.13×10^{-4}	1.9822	1.39×10^{5}	1.71×10^{-6}	4.29×10^{5}	0.0049
176.1	1.4987	7.39×10^{14}	3.84×10^{14}	1.42×10^{-4}	1.7739	1.47×10^{5}	2.14×10^{-6}	3.42×10^{5}	0.0042
203.6	1.4359	9.88×10^{14}	5.14×10^{14}	1.74×10^{-4}	1.5835	1.56×10^{5}	2.62×10^{-6}	2.8×10^{5}	0.0036
231.1	1.3852	1.27×10^{15}	6.62×10^{14}	2.09×10^{-4}	1.4082	1.65×10^{5}	3.15×10^{-6}	2.32×10^{5}	0.0032
258.6	1.3431	1.59×10^{15}	8.29×10^{14}	2.49×10^{-4}	1.2464	1.75×10^{5}	3.75×10^{-6}	1.95×10^{5}	0.0028
286.1	1.3074	1.95×10^{15}	1.02×10^{15}	2.93×10^{-4}	1.0974	1.87×10^{5}	4.42×10^{-6}	1.66×10^{5}	0.0026
313.6	1.2766	2.35×10^{15}	1.22×10^{15}	3.44×10^{-4}	0.9605	$2. \times 10^{5}$	5.18×10^{-6}	1.41×10^{5}	0.0023
341.1	1.2497	2.77×10^{15}	1.44×10^{15}	4.01×10^{-4}	0.8354	2.14×10^{5}	6.04×10^{-6}	1.21×10^{5}	0.0021
368.6	1.2258	3.24×10^{15}	1.69×10^{15}	4.66×10^{-4}	0.7215	2.31×10^{5}	7.02×10^{-6}	1.04×10^{5}	0.002
396.1	1.2044	3.74×10^{15}	1.95×10^{15}	5.41×10^{-4}	0.6183	2.49×10^{5}	8.15×10^{-6}	8.98×10^{4}	0.0018
423.6	1.1851	4.28×10^{15}	2.23×10^{15}	6.28×10^{-4}	0.5255	2.7×10^{5}	9.45×10^{-6}	7.74×10^{4}	0.0017
451.1	1.1676	4.85×10^{15}	2.52×10^{15}	7.28×10^{-4}	0.4424	2.94×10^{5}	1.1×10^{-5}	6.67×10^{4}	0.0016
478.6	1.1516	5.46×10^{15}	2.84×10^{15}	8.47×10^{-4}	0.3685	3.23×10^{5}	1.28×10^{-5}	5.74×10^{4}	0.0015
506.2	1.1369	6.11×10^{15}	3.18×10^{15}	9.87×10^{-4}	0.3034	3.56×10^{5}	1.49×10^{-5}	4.92×10^{4}	0.0014
533.7	1.1233	6.79×10^{15}	3.53×10^{15}	1.15×10^{-3}	0.2465	3.94×10^{5}	1.74×10^{-5}	4.21×10^{4}	0.0014
561.2	1.1107	7.51×10^{15}	3.91×10^{15}	1.36×10^{-3}	0.1972	4.41×10^{5}	2.04×10^{-5}	3.58×10^{4}	0.0013
588.7	1.099	8.26×10^{15}	4.3×10^{15}	1.61×10^{-3}	0.155	4.97×10^{5}	2.42×10^{-5}	3.03×10^{4}	0.0012
616.2	1.088	9.05×10^{15}	4.71×10^{15}	1.92×10^{-3}	0.1194	5.67×10^{5}	2.88×10^{-5}	2.54×10^{4}	0.0012
643.7	1.0777	9.88×10^{15}	5.14×10^{15}	2.31×10^{-3}	0.0897	6.54×10^{5}	3.48×10^{-5}	2.1×10^{4}	0.0011
671.2	1.068	1.07×10^{16}	5.59×10^{15}	2.82×10^{-3}	0.0654	7.66×10^{5}	4.24×10^{-5}	1.72×10^{4}	0.0011
698.7	1.0589	1.16×10^{16}	6.06×10^{15}	3.5×10^{-3}	0.046	9.13×10^{5}	5.27×10^{-5}	1.39×10^{4}	0.001
726.2	1.0503	1.26×10^{16}	6.54×10^{15}	4.44×10^{-3}	0.0309	1.11×10^{6}	6.68×10^{-5}	1.09×10^{4}	0.001
753.7	1.0421	1.35×10^{16}	7.05×10^{15}	5.79×10^{-3}	0.0195	1.4×10^{6}	8.73×10^{-5}	8.38×10^{3}	0.001
781.2	1.0343	1.46×10^{16}	7.57×10^{15}	7.87×10^{-3}	0.0114	1.84×10^{6}	1.19×10^{-4}	6.17×10^{3}	0.0009
808.8	1.0269	1.56×10^{16}	8.11×10^{15}	1.13×10^{-2}	0.0059	2.55×10^{6}	1.71×10^{-4}	4.29×10^{3}	0.0009

APPENDIX B

Plasma resistivity

As known (see e.g., Goldston & Rutherford, 1995, pg. 174), an electric field which is applied to a fully ionised electron-proton plasma accelerates the negatively charged electrons in the opposite direction to the electric field, whereas the protons (or positively charged ions) are accelerated in the direction of the electric field. Thus the relative motion between the electrons and the protons increases and an electrical current in direction of $\vec{E}$ is generated. The Coulomb collisions occurring between electrons and protons delay this relative motion and after some electron-proton collisions a steady state is reached. In equilibrium the isotropic plasma fulfils

$$\vec{E} = \eta \vec{j}, \tag{B.1}$$

where the constant of proportionality η represents the resistivity.[1] The classical Spitzer (1965) resistivity itself follows from the equation of motion for an electron within an uniform plasma either with no magnetic field or along the magnetic field. Thus the magnetic field does not appear in the equation of motion of the electron fluid

$$N_\mathrm{e} m_\mathrm{e} \frac{\mathrm{d}^2 \vec{u}_\mathrm{e}}{\mathrm{d}t^2} = -eN_\mathrm{e}\vec{E} - \overline{\nu} N_\mathrm{e} \frac{(\vec{u}_\mathrm{e} - \vec{u}_\mathrm{p})}{\left({}^1\!/_{m_\mathrm{e}} + {}^1\!/_{m_\mathrm{p}}\right)}. \tag{B.2}$$

The quantities N_e, m_e, m_p, $\vec{u}_\mathrm{e}$, $\vec{u}_\mathrm{p}$, and $\overline{\nu}$ represent the electron number density, the electron mass, the ion mass, the electron fluid velocity, the ion fluid velocity, and the averaged Coulomb collision frequency, respectively. The index "e" stands for an "electron" and "p" represents a positively charged "ion", i.e., a proton. The last sum on the right hand side of Eq. (B.2) describes the electron's momentum gain or loss, caused by combined action of the electric field and the Coulomb collisions with ions. Introducing the current density $\vec{j}$ with

$$\vec{j} = -eN_\mathrm{e}\left(\vec{u}_\mathrm{e} - \vec{u}_\mathrm{p}\right), \tag{B.3}$$

neglecting the electron inertia due to its very small mass, and using Eq. (B.1), i.e.,

$$0 = -eN_\mathrm{e}\eta\vec{j} + \frac{\overline{\nu}}{e\left({}^1\!/_{m_\mathrm{e}} + {}^1\!/_{m_\mathrm{p}}\right)}\vec{j} \quad \Leftrightarrow \quad \eta = \frac{\left({}^1\!/_{m_\mathrm{e}} + {}^1\!/_{m_\mathrm{p}}\right)^{-1}\overline{\nu}}{e^2 N_\mathrm{e}} \tag{B.4}$$

is obtained for the resistivity (see e.g., Kegel, 1998, pg. 175). In the current paper the averaged Coulomb collision frequency $\overline{\nu}$ is given by

$$\overline{\nu} = \frac{D_\mathrm{e}\big|_{\beta=\beta_\mathrm{th}}}{\beta_\mathrm{th}} + \frac{D_\mathrm{p}\big|_{\beta=\beta_\mathrm{th}}}{2\beta_\mathrm{th}} \tag{B.5}$$

[1] Since, this paper deals with a one-dimensional magnetic loop geometry, η is considered to be a scalar. In the most general case, it has to be treated as a 3×3-matrix.

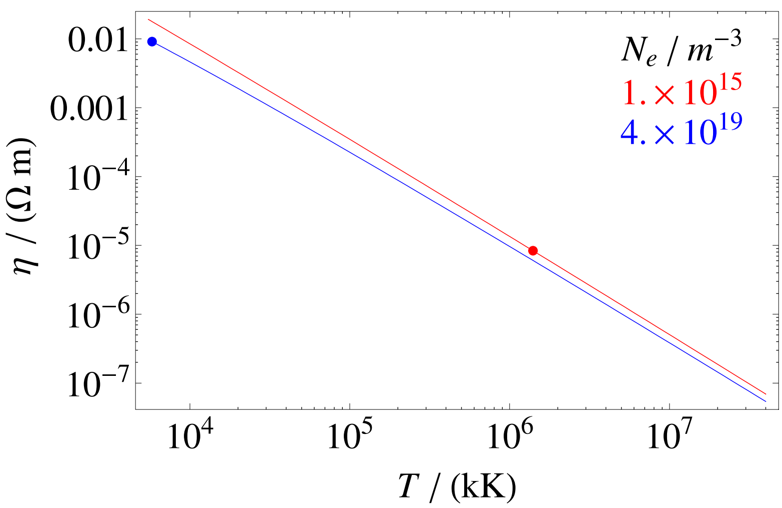

Figure B.1: The electric resistivity η is plotted in dependence on the temperature for two different electron densities. The dots in the diagram mark the conditions for the photosphere ($N_\mathrm{e} = 4 \times 10^{19}\,\mathrm{m}^{-3}$) and the corona ($N_\mathrm{e} = N_\mathrm{co} = 10^{15}\,\mathrm{m}^{-3}$).

by using of Eq. (6.5).

The resistivity obtained from Eq. (B.4) for coronal conditions ($T = 1.4\,\mathrm{MK}$, $N_\mathrm{e} = 10^{15}\,\mathrm{m}^{-3}$) is $8.38 \times 10^{-6}\,\Omega\mathrm{m}$. On the other hand the resistivity for the photospheric conditions ($T = 5.8\,\mathrm{kK}$, $N_\mathrm{e} = 4 \times 10^{19}\,\mathrm{m}^{-3}$) is $9\,140.39 \times 10^{-6}\,\Omega\mathrm{m}$. As mentioned in the introduction, it can be seen from these values that the electric conductivity, i.e., the reciprocal resistivity, in the corona is about 1 090 times higher, than in the photosphere. The dependence of the resistivity on the temperature is presented in Fig. B.1. The dots in the diagram correspond to the values given in this paragraph.

APPENDIX C

Relative velocities

Subsequently the averaged relative velocity between an electron moving through an electron-proton plasma and the plasma's electrons and protons is calculated.

The expression

$$\beta_\varsigma c = \sqrt{\int \mathrm{d}^3\hat{v}\left[\left((V_0-\hat{v}_x)^2+\hat{v}_y^2+\hat{v}_z^2\right) f_\varsigma[\vec{\hat{v}}]\right]} \tag{C.1}$$

represents the definition of the averaged relative velocity of an electron with the particles of the species ς of the plasma in which it penetrates with the velocity V_0 along the x-axis. The speed of light is represented by c. $f_\varsigma[\vec{v}]$ is the velocity distribution function of the particles ς in the (background) plasma. Assuming it to be a classical to unity normalised Maxwellian velocity distribution

$$f_\varsigma[\vec{v}] = \frac{1}{\left(2\pi\, v_{\mathrm{th},\varsigma}^2\right)^{3/2}} \exp\left[-\frac{\vec{v}^2}{2\, v_{\mathrm{th},\varsigma}^2}\right] \tag{C.2}$$

the integral of Eq. (C.1) can be calculated after introducing spherical coordinates, leading to

$$\begin{aligned}\beta_\varsigma^2 c^2 &= \frac{4\pi}{\left(2\,\pi v_{\mathrm{th},\varsigma}^2\right)^{3/2}} \int_0^\infty \mathrm{d}v\left[v^2\left(V_0^2+v^2\right)\exp\left[-\frac{v^2}{2v_{\mathrm{th},\varsigma}^2}\right]\right] &\text{(C.3)}\\ &= V_0^2+3v_{\mathrm{th},\varsigma}^2. &\text{(C.4)}\end{aligned}$$

Here $v_{\mathrm{th},\varsigma} = \left({k_\mathrm{B}T}/{m_\varsigma}\right)^{1/2}$ stands for the thermal speed of the particles of the species ς. Finally after normalising the velocities to the speed of light the averaged relative velocity between the electron and the plasma's electrons can be written as

$$\beta_\mathrm{e} = \sqrt{\beta_0^2+3\beta_{\mathrm{th,e}}^2} = \sqrt{\beta_0^2+3\beta_{\mathrm{th}}^2}. \tag{C.5}$$

Due to the high inertia of the protons, the averaged relative velocity between an electron and the plasma's protons is found to be

$$\beta_\mathrm{p} = \sqrt{\beta_0^2+3\beta_{\mathrm{th,p}}^2} \approx \beta_0. \tag{C.6}$$

These obtained Eqs. (C.5) and (C.6) have been used in Eq. (6.5) (see Sect. 6.1).

Part V

Epilogue

All truths are easy to understand once they are discovered; the point is to discover them.

– Galileo Galilei

Acknowledgements

First and foremost I want to express my deepest gratitude to everyone who contributed to the outcome of this thesis.

I am indebted to my thesis advisor, Prof. Dr. Gottfried J. Mann, for his continuous support, guidance and encouragement during my studentship. He and the Astrophysical Institute Potsdam (AIP) have provided a stimulating environment for my research activities. Highly appreciated is the 42 months lasting financial support of my work by the *Deutsches Zentrum für Luft- und Raumfahrt* grant 50 QL 0001.

I very much appreciate the support given to me by all the members of the Solar Radio Physics Group: the many interesting lectures and the many more fruitful scientific and non-scientific discussions were of great use. The theorist Dr. Christian Vocks and the observers Dr. Henry Auraß, Dr. Alexander Warmuth, as well as, the former PhD students, Dr. Germar Rausche and Dr. Rossitsa Miteva, the former colleagues Dr. H. Theo Claßen, Dr. Marina Skender and of course the secretary Mrs. Doris Lehmann supported me, whenever I had needs for them. Thanks a lot!

I am very grateful for the people of the AIP's computer department in general, and Dr. Karl-Heinz Böning in particular, who has earned my special thanks for his outstanding self sacrificing help, whenever a problem related with computers or a need of technical equipment or software was imminent.

I very much want to acknowledge Dr. Tae-Sun Kim's efforts for independently cross checking the resulting total fluxes calculated in Sect. 7.2. I am also thankful for M. Sc. Stevan White, who helped me out with my English at various passages in this thesis.

My supervisor Prof. Dr. Gottfried J. Mann, and Cand. Phys. Martin Reinke were this thesis' test readers. Their valuable feedback had a huge impact on the final version of it.

Furthermore I want to thank Prof. Dr. Erwin Sedlmeyr, who substantially supported me during my undergraduate student time at the Berlin University of Technology (TUB). His intriguing lectures strengthened my interest for astrophysics, and relativity in special. With no words I can express my gratitude for my outstanding physics teacher Dipl. Phys. Christian Fließbach from school, whose method of teaching was most stimulating.

I also do not want to forget Dr. Hans Blersch and the whole staff of the computer room at the department of physics at the TUB, where I found the technical equipment, and a sufficient number of available *Wolfram Research Mathematica* licenses to quickly perform the elaborate calculations presented in this thesis. Without Prof. Dr. Donald E. Knuth's TeX, Dr. Leslie Lamport's LaTeX and Ingo H. de Boer's very nice editor *WinShell*[1] writing this thesis would not have been as easy as it was.

[1] *WinShell* can be found at `http://www.winshell.org`.

During my PhD time I had the opportunity to do some travelling in order to visit a few national and international conferences, namely

- ◇ the "6th International Workshop on Planetary and Solar Radio Emissions" in Graz,
- ◇ the "6th *RHESSI* Workshop" in Meudon,
- ◇ the "International Heliophysical Year" in Bad Honnef,
- ◇ the anual meeting of the "Deutsche Physikalische Gesellschaft" in Freiburg,
- ◇ the "8th *RHESSI* Workshop" in Potsdam.

The lectures I listened to, the people I met there, and the discussions I had with them, as well as the impressions I obtained during these few days, were most stimulating.

In particular I want to thank to Dr. Jasmina Magdalenić and to Mag. rer. nat. Sigrid Stoiser for the ongoing and very precious friendships which established during the meetings mentioned above.

Of course my PhD time did not consist of work only: Though the occasions were rare, I am (in alphabetical order) very thankful for M.A. Angl./Am. Shehan Bonatz, Dr. Katja Janßen, Cand. Phys. Johanna Juszkiewicz, Dr. Tae-Sun Kim, Dipl.-Phys. Ulrike Lemke, Dr. Iliya Nickelt-Czycykowski, Dr. Christer Sandin (by the way: thanks for the acknowledgements in Sandin (2008)) Dr. Marina Skender, and M. Sc. Stevan White, who joined me for movies, museum visits, table tennis games and other activities outside the working hours on a regular basis.

I also want to express my thanks to my close friends Dipl. Phys. Mandy Baudach, Krzysztof Milinski, Kerstin Karottke, Dipl. Phys. Lena Ivanova and to all the other people, who understood that I could not meet them as frequently, as I would have liked to, while I was busy with this thesis.

I will never ever forget Christian H. Weise, a close friend of mine, who was killed a few weeks before his 18th birthday by a traffic accident in 1997. I still remember the very interesting discussions we had, when we both were observing the comets Hyakutake (C/1996 B2) and Hale-Bopp (C/1995 O1) in 1996 and 1997, respectively.

I also want to acknowledge Cand. Phys. Stephan J. Simon, who died in 2005. His idealism and impressive personality helped us to succeed many different science labs during my undergraduate student time.

Thank you for all the time we were destined to share!

Last but not least, I want to express my most sincere thanks to those people, who made my education possible: My beloved parents. Therefore the thesis at hand is dedicated to my Mum Nilgül, and Dad Eşref Önel. Without their continuous support and love throughout all the years I would not have been able to achieve anything.

Sizi çok seviyorum ve size çok teşekkür ediyorum.

Thank you very much !

H. Önel

This document was created with LaTeX 2$_{\varepsilon}$.

Potsdam, August 11, 2008.

Bibliography

Abramowitz, M., & Stegun, I. A. 1972. *Handbook of Mathematical Functions.* Handbook of Mathematical Functions, New York: Dover, 1972.

Akasofu, S.-I. 1979. Magnetospheric substorms and solar flares. *Solar Physics*, **64**(Dec.), 333–348.

Alfvén, H., & Carlqvist, P. 1967. Currents in the Solar Atmosphere and a Theory of Solar Flares. *Solar Physics*, **1**, 220–228.

Aschwanden, M. J. (ed). 2002a. *A Synthesis of Recent Observations and Theoretical Concepts.* Space Science Reviews, vol. 101. Kluwer Academic Publishers. ISBN 1-402-00725-6, available at `http://www.lmsal.com/~aschwand/eprints/2002_acc/`.

Aschwanden, M. J. 2002b. Particle acceleration and kinematics in solar flares A Synthesis of Recent Observations and Theoretical Concepts (Invited Review). *Space science reviews*, **101**(Jan.), 1–227.

Aschwanden, M. J. 2006. *Physics of the Solar Corona.* Springer-Verlag Berlin Heidelberg New York, Praxis Publishing Ltd, Chicester. ISBN 3-540-22321-5, available at `http://www.lmsal.com/~aschwand/eprints/2006_paperback/`.

Aschwanden, M. J., Schwartz, R. A., & Alt, D. M. 1995a. Electron Time-of-Flight Differences in Solar Flares. *The Astrophysical Journal*, **447**(July), 923–935.

Aschwanden, M. J., Benz, A. O., Dennis, B. R., & Schwartz, R. A. 1995b. Solar Electron Beams Detected in Hard X-Rays and Radio Waves. *The Astrophysical Journal*, **455**(Dec.), 347–365.

Aschwanden, M. J., Newmark, J. S., Delaboudinière, J.-P., Neupert, W. M., Klimchuk, J. A., Gary, G. A., Portier-Fozzani, F., & Zucker, A. 1999. Three-dimensional Stereoscopic Analysis of Solar Active Region Loops. I. SOHO/EIT Observations at Temperatures of (1.0-1.5) X 10ˆ6 K. *The Astrophysical Journal*, **515**(Apr.), 842–867.

Aurass, H., & Mann, G. 2004. Radio Observation of Electron Acceleration at Solar Flare Reconnection Outflow Termination Shocks. *The Astrophysical Journal*, **615**(Nov.), 526–530.

Aurass, H., Vršnak, B., & Mann, G. 2002. Shock-excited radio burst from reconnection outflow jet? *Astronomy & Astrophysics*, **384**(Mar.), 273–281.

Aurass, H., Rausche, G., Mann, G., & Hofmann, A. 2005. Fiber bursts as 3D coronal magnetic field probe in postflare loops. *Astronomy & Astrophysics*, **435**(June), 1137–1148.

Aurass, H., Rausche, G., & Mann, G. 2007. Radio burst from converging separatrices. *Astronomy & Astrophysics*, **471**(Aug.), L37–L40.

Baumjohann, W., & Treumann, R. A. 1996. *Basic space plasma physics*. London: Imperial College Press.

Beck, J. G., & Duvall, Jr., T. L. 2001 (Jan.). Time-distance study of supergranulation. *Pages 577–581 of:* Wilson, A., & Pallé, P. L. (eds), *Soho 10/gong 2000 workshop: Helio- and asteroseismology at the dawn of the millennium*. ESA Special Publication, vol. 464.

Benz, A. O. 1987. Acceleration and energization by currents and electric fields. *Solar Physics*, **111**, 1–18.

Benz, A. O., Brajša, R., & Magdalenić, J. 2007. Are There Radio-quiet Solar Flares? *Solar Physics*, **240**(Feb.), 263–270.

Benz, Arnold O. 2008. Flare observations. *Living reviews in solar physics*, **5**(1). Available at `http://www.livingreviews.org/lrsp-2008-1`.

Birch, A. C., & Gizon, L. 2005. Local helioseismology. *Living reviews in solar physics*, **2**(6). Available at `http://www.livingreviews.org/lrsp-2005-6`.

Bourouaine, S., Vocks, C., & Marsch, E. 2008. Coronal Loop Model Including Ion Kinetics. *The Astrophysical Journal*, **676**(Apr.), 1346–1355.

Bronstein, I. N., Semendjajew, K. A., Musiol, G., & Mühlig, H. 1999. *Taschenbuch der mathematik*. Frankfurt am Main: Verlag Harri Deutsch. 4. überarbeitete und erweiterte Auflage, ISBN 3-8171-2014-1.

Brown, J. C. 1971. The Deduction of Energy Spectra of Non-Thermal Electrons in Flares from the Observed Dynamic Spectra of Hard X-Ray Bursts. *Solar Physics*, **18**, 489–502.

Brown, J. C. 1972. The Directivity and Polarisation of Thick Target X-Ray Bremsstrahlung from Solar Flares. *Solar Physics*, **26**, 441–459.

Caroubalos, C., Maroulis, D., Patavalis, N., Bougeret, J.-L., Dumas, G., Perche, C., Alissandrakis, C., Hillaris, A., Moussas, X., Preka-Papadema, P., Kontogeorgos, A., Tsitsipis, P., & Kanelakis, G. 2001. The New Multichannel Radiospectrograph ARTEMIS-IV/HECATE, of the University of Athens. *Experimental astronomy*, **11**(Feb.), 23–32.

Chitre, S. M. 1968. The Evershed Motion in Sunspots. *Solar Physics*, **4**, 168–175.

Debye, P., & Hückel, E. 1923a. Berichtigung zu der Arbeit: „Zur Theorie der Elektrolyte – II. Das Grenzgesetz für die elektrische Leitfähigkeit“. *Physikalische zeitschrift*, **24**, 428–428.

Debye, P., & Hückel, E. 1923b. Zur Theorie der Elektrolyte – I. Gefrierpunkterniedrigung und verwandte Erscheinungen. *Physikalische zeitschrift*, **24**, 185–206.

Debye, P., & Hückel, E. 1923c. Zur Theorie der Elektrolyte – II. Das Grenzgesetz für die elektrische Leitfähigkeit. *Physikalische zeitschrift*, **24**, 305–325.

Dialetis, D., Macris, C., Prokakis, T., & Sarris, E. 1986. The lifetime and evolution of solar granules. *Astronomy & Astrophysics*, **168**(Nov.), 330–334.

Dreicer, H. 1959. Electron and Ion Runaway in a Fully Ionized Gas. I. *Physical review*, **115**(July), 238–249.

Dreicer, H. 1960. Electron and Ion Runaway in a Fully Ionized Gas. II. *Physical review*, **117**(Jan.), 329–342.

Dulk, G. A., & McLean, D. J. 1978. Coronal magnetic fields. *Solar Physics*, **57**(Apr.), 279–295.

Eddy, J. A., & Ise, R. 1979. New Sun: The Solar Results From Skylab. NASA SP-402. *Nasa special publication*, **402**.

Emslie, A. G., Kucharek, H., Dennis, B. R., Gopalswamy, N., Holman, G. D., Share, G. H., Vourlidas, A., Forbes, T. G., Gallagher, P. T., Mason, G. M., Metcalf, T. R., Mewaldt, R. A., Murphy, R. J., Schwartz, R. A., & Zurbuchen, T. H. 2004. Energy partition in two solar flare/CME events. *Journal of geophysical research (space physics)*, **109**(A18), 10104.

Encyclopedia of Astronomy and Astrophysics. 2006. *Encyclopedia of astronomy and astrophysics*. Available at `http://eaa.crcpress.com/`.

European Space Agency. 2006 (Dec.). *Hinode's first images of our violent sun*. Available at `http://www.esa.int/esaSC/SEMII1R08ZE_index_1.html`.

Evershed, J. 1909. Radial movement in sun-spots. *Monthly Notices of the Royal Astronomical Society*, **69**(Mar.), 454–458.

Fan, Y. 2004. Magnetic fields in the solar convection zone. *Living reviews in solar physics*, **1**(1). Available at `http://www.livingreviews.org/lrsp-2004-1`.

Forbes, T. G. 1986. Fast-shock formation in line-tied magnetic reconnection models of solar flares. *The Astrophysical Journal*, **305**(June), 553–563.

Gallagher, P. T., Lawrence, G. R., & Dennis, B. R. 2003. Rapid Acceleration of a Coronal Mass Ejection in the Low Corona and Implications for Propagation. *The Astrophysical Journal Letters*, **588**(May), L53–L56.

Gilbert, H. R., Holzer, T. E., & Burkepile, J. T. 2001. Observational Interpretation of an Active Prominence on 1999 May 1. *The Astrophysical Journal*, **549**(Mar.), 1221–1230.

Gizon, L., Duvall, Jr., T. L., & Schou, J. 2003a. Erratum: wave-like properties of solar supergranulation. *Nature*, **421**(Feb.), 764.

Gizon, L., Duvall, T. L., & Schou, J. 2003b. Wave-like properties of solar supergranulation. *Nature*, **421**(Jan.), 43–44.

Goldston, R. J., & Rutherford, P. H. 1995. *Introduction to plasma physics*. Institute of Physics Publishing, London.

Heber, B., Dröge, W., Klecker, B., & Mann, G. 2007. Die Sonne als Teilchenbeschleuniger. *Physik journal*, **6**(3), 43–49. Available at `http://www.pro-physik.de/Phy/pjtoc/25004/3`.

Heyvaerts, J. 1974. Coronal electric currents produced by photospheric motions. *Solar Physics*, **38**(Oct.), 419–437.

Hofmann, A., Ruždjak, V., & Vršnak, B. 1992. A Study on Electric Currents in a Solar Active Region - a Dynamo Process at a Place of Repeated Flaring. *Hvar observatory bulletin*, **16**, 29–40.

Holman, G. D. 1985. Acceleration of runaway electrons and Joule heating in solar flares. *The Astrophysical Journal*, **293**(June), 584–594.

Holman, G. D. 1995. DC Electric Field Acceleration of Ions in Solar Flares. *The Astrophysical Journal*, **452**(Oct.), 451–456.

Holman, G. D. 2006. Explosionen auf der Sonne. *Spektrum der wissenschaft*, June, 40–47.

HOLMAN, G. D., & PESSES, M. E. 1983. Solar type II radio emission and the shock drift acceleration of electrons. *The Astrophysical Journal*, **267**(Apr.), 837–843.

HUDSON, H. 2007 (Sept.). *Hugh hudson's solarmuri home page*. Available at `http://solarmuri.ssl.berkeley.edu/~hhudson/cartoons/`.

IVORY, K. 1998. *Suprathermische Elektronen im Sonnenwind als Indikatoren außergewöhnlicher Magnetfeldstrukturen der inneren Heliosphäre*. Ph.D. thesis, Georg-August-Universität zu Göttingen. Available at `http://webdoc.sub.gwdg.de/diss/1999/ivory/inhalt.htm`.

JANSEN, F., HILGERS, A., GLOVER, A., SCHWENN, R., BREKKE, P., KLECKER, B., DROLSHAGEN, G., JAKOWSKI, N., BENIGUEL, Y., SCHLEGEL, K., PULKKINEN, A., PIRJOLA, R., VILJANEN, A., FAVRE, R., BÜRGE, M., STELMACH, J., & LEHMUSKALLIO, J. 2003. *CD-ROM: Space Weather*. Available at `http://www.1a-firstapplications.com/MuSTAnGe.html`.

KAN, J. R., AKASOFU, S.-I., & LEE, L. C. 1983. A dynamo theory of solar flares. *Solar Physics*, **84**(Apr.), 153–167.

KARLICKÝ, M., & BÁRTA, M. 2007. Magnetic reconnection in solar flares and corresponding radio bursts. *Advances in space research*, **39**, 1415–1420.

KEGEL, W. H. 1998. *Plasmaphysik*. Eine Einführung, X, 320 S. 61 Abb., 5 in Farbe. Springer-Verlag Berlin Heidelberg New York. ISBN 3-540-63701-X.

KIENER, J., GROS, M., TATISCHEFF, V., & WEIDENSPOINTNER, G. 2006. Properties of the energetic particle distributions during the October 28, 2003 solar flare from INTEGRAL/SPI observations. *Astronomy & Astrophysics*, **445**(Jan.), 725–733.

KITAHARA, T., & KUROKAWA, H. 1990. High-resolution observation and detailed photometry of a great H-alpha two-ribbon flare. *Solar Physics*, **125**(Feb.), 321–332.

KLIMCHUK, J. A. 2000. Cross-Sectional Properties of Coronal Loops. *Solar Physics*, **193**(Apr.), 53–75.

KNEER, F., SOLANKI, S. K., STRASSMEIER, J. G., VON DER LÜHE, O., WIMMER-SCHWEINGRUBER, R. F., BRÜGGEN, M., FICHTNER, H., KUNOW, H., MANN, G., MARSCH, E., SCHERER, K, SCHLICHENMAIER, R., SCHÜSSLER, M., SCHWENN, R., STAUDE, J., & WOCH, J. 2003. *Perspektiven der Erforschung von Sonne und Heliosphäre in Deutschland*. Copernicus GmbH, Katlenburg-Lindau. ISBN 3-936586-19-5, available at `http://www.mps.mpg.de/dokumente/publikationen/perspektiven/Perspektiven.pdf`.

KONTAR, E. P., EMSLIE, A. G., MASSONE, A. M., PIANA, M., BROWN, J. C., & PRATO, M. 2007. Electron-Electron Bremsstrahlung Emission and the Inference of Electron Flux Spectra in Solar Flares. *The Astrophysical Journal*, **670**(Nov.), 857–861.

KOUTCHMY, S. 1994. Coronal physics from eclipse observations. *Advances in space research*, **14**(Apr.), 29–39.

LIFSHITZ, E. M., & PITAEVSKII, L. P. 1990. *Landau Lifshitz: Lehrbuch der Theoretischen Physik*. 2nd edn. Vol. 10. Akademie Verlag GmbH. ISBN 3-05-500074-9.

LIN, R. P. 1974. Non-relativistic Solar Electrons. *Space science reviews*, **16**, 189–256.

LIN, R. P., & HUDSON, H. S. 1971. 10-100 keV Electron Acceleration and Emission from Solar Flares. *Solar Physics*, **17**, 412–435.

LIN, R. P., & HUDSON, H. S. 1976. Non-thermal processes in large solar flares. *Solar Physics*, **50**(Oct.), 153–178.

Lin, R. P., Dennis, B. R., Hurford, G. J., Smith, D. M., Zehnder, A., Harvey, P. R., Curtis, D. W., Pankow, D., Turin, P., Bester, M., Csillaghy, A., Lewis, M., Madden, N., van Beek, H. F., Appleby, M., Raudorf, T., McTiernan, J., Ramaty, R., Schmahl, E., Schwartz, R., Krucker, S., Abiad, R., Quinn, T., Berg, P., Hashii, M., Sterling, R., Jackson, R., Pratt, R., Campbell, R. D., Malone, D., Landis, D., Barrington-Leigh, C. P., Slassi-Sennou, S., Cork, C., Clark, D., Amato, D., Orwig, L., Boyle, R., Banks, I. S., Shirey, K., Tolbert, A. K., Zarro, D., Snow, F., Thomsen, K., Henneck, R., Mchedlishvili, A., Ming, P., Fivian, M., Jordan, J., Wanner, R., Crubb, J., Preble, J., Matranga, M., Benz, A., Hudson, H., Canfield, R. C., Holman, G. D., Crannell, C., Kosugi, T., Emslie, A. G., Vilmer, N., Brown, J. C., Johns-Krull, C., Aschwanden, M., Metcalf, T., & Conway, A. 2002. The Reuven Ramaty High-Energy Solar Spectroscopic Imager (*RHESSI*). *Solar Physics*, **210**(Nov.), 3–32.

Litvinenko, Y. E. 2000. Electron Acceleration by Strong DC Electric Fields in Impulsive Solar Flares. *Pages 167–170 of:* Ramaty, R., & Mandzhavidze, N. (eds), *Asp conf. ser. 206: High energy solar physics workshop - anticipating hess!*

Longcope, D. W. 2005. Topological methods for the analysis of solar magnetic fields. *Living reviews in solar physics*, **2**(7). Available at `http://www.livingreviews.org/lrsp-2005-7`.

Magdalenić, J. 2007. *Solar radio emission and diagnostics of Solar coronal plasma*. Ph.D. thesis, University of Zagreb, Faculty of Science.

Magdalenić, J., Vršnak, B., Zlobec, P., Hillaris, A., & Messerotti, M. 2006. Classification and Properties of Supershort Solar Radio Bursts. *The Astrophysical Journal Letters*, **642**(May), L77–L80.

Mann, G. 2007. Die Sonnenkorona. *Sterne und weltraum special*, **1**(Dec.), 24–25.

Mann, G., & Classen, H.-T. 1995. Electron acceleration to high energies at quasi-parallel shock waves in the solar corona. *Astronomy & Astrophysics*, **304**(Dec.), 576–584.

Mann, G., Aurass, H., Voigt, W., & Paschke, J. 1992 (Nov.). Preliminary observations of solar type 2 bursts with the new radiospectrograph in Tremsdorf (Germany). *Pages 129–132 of:* Mattok, C. (ed), *Esa sp-348: Coronal streamers, coronal loops, and coronal and solar wind composition.*

Mann, G., Jansen, F., MacDowall, R. J., Kaiser, M. L., & Stone, R. G. 1999. A heliospheric density model and type III radio bursts. *Astronomy & Astrophysics*, **348**(Aug.), 614–620.

Mann, G., Classen, H.-T., & Motschmann, U. 2001. Generation of highly energetic electrons by shock waves in the solar corona. *Journal of Geophysical Research*, **106**(Nov.), 25323–25332.

Mann, G., Aurass, H., & Warmuth, A. 2006. Electron acceleration by the reconnection outflow shock during solar flares. *Astronomy & Astrophysics*, **454**(Aug.), 969–974.

Marsch, E. 2006. Kinetic physics of the solar corona and solar wind. *Living reviews in solar physics*, **3**(1). Available at `http://www.livingreviews.org/lrsp-2006-1`.

Martres, M.-J., Soru-Escaut, I., & Rayrole, J. 1973. Relationship between Some Photospheric Motions and the Evolution of Active Centers. *Solar Physics*, **32**, 365–378.

Matthaeus, W. H., Elliott, H. A., & McComas, D. J. 2006. Correlation of speed and temperature in the solar wind. *Journal of geophysical research*, **111**(Oct.), 1–6. A10103, DOI: 10.1029/2006JA011636.

MELROSE, D. B. 1994. Turbulent acceleration in solar flares. *Astrophysical Journal Supplement Series*, **90**(Feb.), 623–630.

MENDE, D., & SIMON, G. 1971. *Physik · Gleichungen und Tabellen*. 3rd edn. VEB Fachbuchverlag Leibzig 1971.

MIESCH, M. S. 2005. Large-scale dynamics of the convection zone and tachocline. *Living reviews in solar physics*, **2**(1). Available at http://www.livingreviews.org/lrsp-2005-1.

MILLER, J. A., CARGILL, P. J., EMSLIE, A. G., HOLMAN, G. D., DENNIS, B. R., LAROSA, T. N., WINGLEE, R. M., BENKA, S. G., & TSUNETA, S. 1997. Critical issues for understanding particle acceleration in impulsive solar flares. *Journal of Geophysical Research*, **102**(July), 14631–14660.

MITALAS, R., & SILLS, K. R. 1992. On the photon diffusion time scale for the sun. *The Astrophysical Journal*, **401**(Dec.), 759–760.

MITEVA, R. 2007 (July). *Electron acceleration at localized wave structures in the solar corona*. Ph.D. thesis, University of Potsdam. Available at http://opus.kobv.de/ubp/volltexte/2007/1477/.

MITEVA, R., & MANN, G. 2005 (Dec.). Electron Acceleration due to Jets in the Solar Corona. *In: The dynamic sun: Challenges for theory and observations*. ESA Special Publication, vol. 600.

MITEVA, R., & MANN, G. 2007. Electron Acceleration at Whistler Wave Packets Attached to Coronal Shock Waves. *Central european astrophysical bulletin*, **31**, 155–164.

MITEVA, R., MANN, G., VOCKS, C., & AURASS, H. 2007. Excitation of electrostatic fluctuations by jets in a flaring plasma. *Astronomy & Astrophysics*, **461**(Jan.), 1127–1132.

MOHR, P. M., TAYLOR, B. T., & NEWELL, D.B. 2007 (Mar.). *The 2006 CODATA Recommended Values of the Fundamental Physical Constants, Web Version 5.0*. Available at http://physics.nist.gov/constants [2007, September 13]. National Institute of Standards and Technology, Graithersburg, MD 20899.

NAGASHIMA, K., & YOKOYAMA, T. 2006. Statistical Study of the Reconnection Rate in Solar Flares Observed with Yohkoh SXT. *The Astrophysical Journal*, **647**(Aug.), 654–661.

NEWKIRK, G. J. 1961. The Solar Corona in Active Regions and the Thermal Origin of the Slowly Varying Component of Solar Radio Radiation. *The Astrophysical Journal*, **133**(May), 983–1013.

OBAYASHI, T. 1975. Energy build-up and release mechanisms in solar and auroral flares . *Solar Physics*, **40**(Jan.), 217–226.

O'NEILL, I. J. 1998. *Quiescent coronal loops heated by turbulence*. Ph.D. thesis, University of Wales Aberystwyth. Available at http://www.astroengine.net/projects/thesis06.pdf.

ÖNEL, H. 2004 (Dec.). *Einfluss von Coulomb-Stößen auf die Ausbreitung von Elektronen im Flare-Plasma der Sonnenkorona*. Diploma thesis, University of Technology Berlin in collaboration with the Astrophysical Institute Potsdam, Germany.

ÖNEL, H., MANN, G., & SEDLMAYR, E. 2007. Propagation of energetic electrons through the solar corona and the interplanetary medium. *Astronomy & Astrophysics*, **463**(Mar.), 1143–1152.

PARKER, E. N. 1958. Dynamics of the Interplanetary Gas and Magnetic Fields. *The Astrophysical Journal*, **128**(Nov.), 664–676.

PARKER, E.N. 1963. *Interplanetary dynamical processes*. Interscience Monographs and Texts in Physics and Astronomy, vol. 8. New York, U.S.A.: Interscience Publishers.

Priest, E. R. 2000. *Solar Magnetohydrodynamics*. D.Reidel Publishing Company, Dordrecht, Holland.

Rausche, G. 2008 (Feb.). *Ein Verfahren zur Bestimmung des Magnetfeldes in aktiven Strukturen der Sonnenkorona*. Ph.D. thesis, University of Potsdam.

Robinson, P. A. 1996. Stochastic Wave Growth, Power Balance, and Beam Evolution in Type III Solar Radio Sources. *Solar physics*, **168**(Oct.), 357–374.

Sakai, J.-I., & de Jager, C. 1996. Solar Flares and Collisions Between Current-Carrying Loops Types and Mechanisms of Solar Flares and Coronal Loop Heating. *Space science reviews*, **77**(July), 1–192.

Sandin, C. 2008. Three-component modelling of C-rich AGB star winds - IV. Revised interpretation with improved numerical descriptions. *Monthly Notices of the Royal Astronomical Society*, Feb., 225.1–225.16.

Santos, J. C., & Büchner, J. 2007. MHD simulation of electric currents in the solar atmosphere caused by photospheric plasma motion. *Astrophysics and space sciences transactions*, **3**(Dec.), 29–33.

Schleicher, H., Balthasar, H., & Wöhl, H. 2003. Velocity Field of a Complex Sunspot with Light Bridges. *Solar Physics*, **215**(Aug.), 261–280.

Schrijver, C. J., & DeRosa, M. L. 2003. Photospheric and heliospheric magnetic fields. *Solar Physics*, **212**(Jan.), 165–200.

Schwenn, R. 2006. Space weather: The solar perspective. *Living reviews in solar physics*, **3**(2). Available at `http://www.livingreviews.org/lrsp-2006-2`.

Sen, H. K., & White, M. L. 1972. A Physical Mechanism for the Production of Solar Flares. *Solar Physics*, **23**, 146–154.

Shibata, K., Masuda, S., Shimojo, M., Hara, H., Yokoyama, T., Tsuneta, S., Kosugi, T., & Ogawara, Y. 1995. Hot-Plasma Ejections Associated with Compact-Loop Solar Flares. *The Astrophysical Journal Letters*, **451**(Oct.), L83–L85.

Smith, H. J., & Smith, E. V. P. 1963. *Solar flares*. New York, Macmillan.

SOHO webpage. 2008 (June). *Hotshot*. Available at `http://sohowww.nascom.nasa.gov/hotshots/2003_10_28/`.

Somov, B. V. (ed). 2000. *Cosmic Plasma Physics*. Astrophysics and Space Science Library, vol. 251. Boston, Mass.: Kluwer Academic Publishers.

Somov, B. V., & Kosugi, T. 1997. Collisionless Reconnection and High-Energy Particle Acceleration in Solar Flares. *The Astrophysical Journal*, **485**(Aug.), 859–868.

Somov, B. V., & Titov, V. S. 1985. Magnetic reconnection in a high-temperature plasma of solar flares. I - Effect of gradient instabilities. *Solar Physics*, **95**(Jan.), 141–153.

Spitzer, L. 1965. *Physics of fully ionized gases*. 2nd rev. ed. edn. Interscience Tracts on Physics and Astronomy, New York: Interscience Publication.

Stix, M. 2002. *The sun: An introduction*. 2nd edn. Astronomy and Astrophysics Library. Berlin, Germany, New York, U.S.A.: Springer.

Treumann, R. A., & Baumjohann, W. 1997. *Advanced space plasma physics*. London: Imperial College Press.

TSUNETA, S., & NAITO, T. 1998. Fermi Acceleration at the Fast Shock in a Solar Flare and the Impulsive Loop-Top Hard X-Ray Source. *The Astrophysical Journal Letters*, **495**(Mar.), L67–L70.

UGAI, M. 2007. Modeling of two-ribbon flares by the fast reconnection mechanism. *Physics of plasmas*, **14**(Oct.), 102904–1–102904–6.

U.S. DEPARTMENT OF ENERGY, ENERGY INFORMATION ADMINISTRATION. 2006 (July). *World consumption of primary energy by energy type and selected country groups: 1980-2004*. Available at `http://www.eia.doe.gov/pub/international/iealf/table18.xls`.

VAN HOVEN, G. 1976. Solar flares and plasma instabilities - Observations, mechanisms and experiments. *Solar Physics*, **49**(July), 95–116.

VERNAZZA, J. E., AVRETT, E. H., & LOESER, R. 1981. Structure of the solar chromosphere. III - Models of the EUV brightness components of the quiet-sun. *Astrophysical Journal Supplement Series*, **45**(Apr.), 635–725.

VOCKS, C. 2001 (Nov.). *Ein kinetisches Modell der Ionen in koronalen Löchern mit Welle-Teilchen–Wechselwirkung und Coulomb–Stößen*. Ph.D. thesis, University of Technology Braunschweig. Available at `http://www.biblio.tu-bs.de/ediss/data/20010405a/20010405a.html`.

VOCKS, C. 2007. Der Sonnenwind. *Sterne und weltraum special*, **1**(Dec.), 36–37.

VRŠNAK, B., & SKENDER, M. 2005. 2 1/2-Dimensional Reconnection Model and Energy Release in Solar Flares. *Solar Physics*, **226**(Jan.), 97–119.

WANG, H., QIU, J., JING, J., & ZHANG, H. 2003. Study of Ribbon Separation of a Flare Associated with a Quiescent Filament Eruption. *The Astrophysical Journal*, **593**(Aug.), 564–570.

WANG, H., QIU, J., JING, J., SPIROCK, T. J., YURCHYSHYN, V., ABRAMENKO, V., JI, H., & GOODE, P. R. 2004. Evidence of Rapid Flux Emergence Associated with the M8.7 Flare on 2002 July 26. *The Astrophysical Journal*, **605**(Apr.), 931–937.

WARMUTH, A. 2007. Sonneneruptionen. *Sterne und weltraum special*, **1**(Dec.), 26–31.

WARMUTH, A., MANN, G., & AURASS, H. 2007. Constraining Electron Acceleration at a Standing Shock with HXR and Radio Observations. *Central european astrophysical bulletin*, **31**, 135–153.

WILLIAMS, D. R. 2007 (Aug.). *Nasa: Sun fact sheet*. Available at `http://nssdc.gsfc.nasa.gov/planetary/factsheet/sunfact.html`.

XU, Y., CAO, W., LIU, C., YANG, G., QIU, J., JING, J., DENKER, C., & WANG, H. 2004. Near-Infrared Observations at 1.56 Microns of the 2003 October 29 X10 White-Light Flare. *The Astrophysical Journal Letters*, **607**(June), L131–L134.

YANG, G., XU, Y., CAO, W., WANG, H., DENKER, C., & RIMMELE, T. R. 2004. Photospheric Shear Flows along the Magnetic Neutral Line of Active Region 10486 prior to an X10 Flare. *The Astrophysical Journal Letters*, **617**(Dec.), L151–L154.

YASHIRO, S., GOPALSWAMY, N., MICHALEK, G., ST. CYR, O. C., PLUNKETT, S. P., RICH, N. B., & HOWARD, R. A. 2004. A catalog of white light coronal mass ejections observed by the SOHO spacecraft. *Journal of geophysical research (space physics)*, **109**(A18), A12S05.1–A12S05.11.

Yashiro, S., Gopalswamy, N., Akiyama, S., Michalek, G., & Howard, R. A. 2005. Visibility of coronal mass ejections as a function of flare location and intensity. *Journal of geophysical research (space physics)*, **110**(A9), A12S05.1–A12S05.11.

Yokoyama, T., Nakajima, H., Shibasaki, K., Melnikov, V. F., & Stepanov, A. V. 2002. Microwave Observations of the Rapid Propagation of Nonthermal Sources in a Solar Flare by the Nobeyama Radioheliograph. *The Astrophysical Journal Letters*, **576**(Sept.), L87–L90.

Zaitsev, V. V., & Stepanov, A. V. 1992. Towards the circuit theory of solar flares. *Solar Physics*, **139**(June), 343–356.

Zaitsev, V. V., Stepanov, A. V., Urpo, S., & Pohjolainen, S. 1998. LRC-circuit analog of current-carrying magnetic loop: diagnostics of electric parameters. *Astronomy & Astrophysics*, **337**(Sept.), 887–896.

Index

Reader's notes